Technische Universität München

TUM School of Natural Sciences

Non-linear magneto-hydrodynamic simulations of hot and mitigated vertical displacement events and validation against experiments in the ASDEX Upgrade tokamak

Nina Schwarz

Vollständiger Abdruck der von der TUM School of Natural Sciences der Technischen Universität München zur Erlangung des akademischen Grades einer

Doktorin der Naturwissenschaften (Dr.rer.nat.)

genehmigten Dissertation.

Vorsitz:	Prof. Dr. Katharina Krischer
Prüfende der Dissertation:	
	1. Hon.-Prof. Dr. Sibylle Günter
	2. Prof. Dr. Carl Sovinec

Die Dissertation wurde am 26. Januar 2024 bei der Technischen Universität München eingereicht und durch die TUM School of Natural Sciences am 10. April 2024 angenommen.

DEPARTMENT OF PHYSICS

TECHNISCHE UNIVERSITÄT MÜNCHEN

Non-linear magneto-hydrodynamic simulations of hot and mitigated vertical displacement events and validation against experiments in the ASDEX Upgrade tokamak

Author:	Nina Schwarz
Supervisor:	Hon.-Prof. Dr. Sibylle Günter
Advisors:	Dr. Matthias Hoelzl
Submission Date:	26. Januar 2024

MAX-PLANCK-INSTITUT
FÜR PLASMAPHYSIK

ASDEX
Upgrade

EUROfusion

Abstract

Fusion has received a lot of attention in the last years, as it promises carbon-free electricity production by nuclear fusion reactions. To make this possible, high temperatures, sufficient densities and confinement of the fuel on longer time scales is required. Under these conditions, the particles are in the plasma state, where they are completely ionized and thus can be influenced by magnetic fields. This thesis focuses on phenomena observed in the so-called tokamak, which is a device in the form of a torus, where ions and electrons are confined by helical magnetic fields. Due to the large toroidal current necessary for confinement, tokamaks are susceptible to certain large scale instabilities leading to the loss of the thermal and magnetic energy stored in the plasma. This phenomenon is called disruption.

The Vertical Displacement Event (VDE) is of particular interest for this thesis, which is determined by the vertical movement of the plasma. We distinguish between the unmitigated and mitigated VDEs. The first are associated with large heat fluxes, electromagnetic forces as well as the occurrence of significant currents outside the core plasma, the so called halo currents. These can result in machine down-time and material aging, so that mitigation techniques are essential for future power plant operation. Active mitigation techniques like the injection of large quantities of material aim to reduce the loads on the machine by diluting the plasma and transferring part of the energy in radiation. The prediction of disruption consequences for future devices by numerical HPC codes is essential for machine safety. One of the codes capable of simulating future machines and the numerically challenging disruptions is the non-linear, extended MHD code JOREK, which is coupled to the electromagnetic wall code STARWALL to take into account the stabilizing effects of surrounding structures.

This thesis aims to validate JOREK for simulating mitigated and unmitigated VDEs by comparing simulation results with dedicated experiments in the tokamak ASDEX Upgrade. It will be shown that important features of the experiment, like the onset of the thermal energy loss, the magnitude of halo currents and comparable electromagnetic forces can be reproduced for the hot VDEs. However, the dynamics depend strongly on the boundary heat flux, which is not self-consistent with the boundary conditions chosen for this thesis. Therefore, scans have been performed to investigate its influence.

The theory of the vertical force reduction in radiation dominated disruptions is introduced in this thesis. Its main point is the induction of large toroidal halo currents outside the core, preventing the movement of the geometric center of the current distribution, which is responsible for the force. Also the shielding by a conductive wall around the plasma can contribute. This was confirmed by 2D simulations in JOREK that reproduce the important features of mitigated VDEs, like the behavior of the current centroid during the plasma current decay, the vertical

forces and the radiation magnitudes.

Finally, JOREK was extended by a coupling to the volumetric wall code CARIDDI to include the eddy current evolution with more realistic structures. The coupling was extensively benchmarked against JOREK-STARWALL and CarMa0NL to prove its reliability. This will allow the inclusion of realistic magnetic diagnostics, shielding effects and the interaction between non-axisymmetric plasmas and wall structures in the future.

Zusammenfassung

Die Kernfusion hat in den letzten Jahren viel Aufmerksamkeit erhalten, da sie die Produktion von kohlenstofffreier Elektrizität durch Kernfusionsreaktionen verspricht. Um dies zu ermöglichen, sind hohe Temperaturen, ausreichende Dichten und der Einschluss des Brennstoffs über längere Zeiträume erforderlich. Unter diesen Bedingungen befinden sich die Teilchen im Plasma-Zustand, wo sie vollständig ionisiert sind und daher von magnetischen Feldern beeinflusst werden können. Diese Arbeit konzentriert sich auf Phänomene, die in dem sogenannten Tokamak beobachtet werden, einem Gerät in Form eines Torus, in dem Ionen und Elektronen durch helikale Magnetfeldlinien eingeschlossen sind. Aufgrund des für den Einschlusses notwendigen großen toroidalen Stroms sind Tokamaks anfällig für bestimmte großskalige Instabilitäten, die zum Verlust der im Plasma gespeicherten thermischen und magnetischen Energie führen. Dieses Phänomen wird als Disruption bezeichnet.

Das Vertical Displacement Event (VDE), das durch die vertikale Bewegung des Plasmas bestimmt wird, ist von besonderem Interesse für diese Arbeit. Wir unterscheiden zwischen unmitigierten und mitigierten VDEs. Die ersteren zeichnen sich durch hohe Wärmeflüssen, elektromagnetischen Kräften sowie dem Auftreten signifikanter Ströme außerhalb des Plasmakerns, den sogenannten Haloströmen, aus. Diese können zu Maschinenausfallzeiten und vorzeitiger Materialalterung führen, sodass Mitigierungstechniken für den zukünftigen Betrieb von Kraftwerken unerlässlich sind. Aktive Mitigierungstechniken wie die Zuführung von einer großen Menge von Material zielen darauf ab die negativen Effekte auf die Maschine zu reduzieren, indem sie den Brennstoff verdünnen und einen Teil der Energie in Strahlung übertragen. Darüber hinaus ist die Vorhersage der Auswirkungen von Disruptionen auf zukünftige Geräte für die Maschinensicherheit unerlässlich, was durch HPC-Codes möglich ist. Einer der Codes, der in der Lage ist, zukünftige Maschinen und numerisch anspruchsvolle Disruptionen zu simulieren, ist der nichtlineare, erweiterte MHD-Code JOREK, der mit dem elektromagnetischen code STARWALL gekoppelt ist, um die stabilisierenden Effekte umgebender Strukturen zu berücksichtigen.

Diese Arbeit zielt darauf ab, JOREK für die Simulation von mitigierten und unmitigierten VDEs zu validieren, indem Simulationsergebnisse mit dedizierten Experimenten im Tokamak ASDEX Upgrade verglichen werden. Es wird gezeigt, dass wichtige Merkmale des Experiments, wie der Beginn des Verlusts thermischer Energie, die Größenordnung der Haloströme und vergleichbare elektromagnetische Kräfte, für die unmitigierten VDEs reproduziert werden können. Die Dynamik hängt jedoch stark vom Randwärmefluss ab, der, mit den für diese Arbeit gewählten Randbedingungen, nicht selbstkonsistent ist. Daher wurden Scans durchgeführt, um seinen Einfluss zu untersuchen.

In dieser Arbeit wird die Theorie der vertikalen Kraftreduktion in strahlungs-

dominierten Disruptionen vorgestellt. Die Voraussetzung hierfür ist das Auftreten signifikanter toroidaler Halo-Ströme außerhalb des Kerns, die die Bewegung des geometrischen Zentrums der Stromverteilung verhindern, das für die Kraft verantwortlich ist. Auch die Abschirmung durch eine leitfähige Wand um das Plasma kann zur Kraftreduktion beitragen. Dies wurde durch 2D-Simulationen in JOREK bestätigt, die wichtige Merkmale mitigierter VDEs reproduzieren, wie das Verhalten des Stromzentrums während des Abfalls des Plasmastroms, die vertikalen Kräfte und die Strahlung.

Schließlich wurde JOREK durch eine Kopplung an den volumetrischen Wandcode CARIDDI zur Erfassung der Wirbelstromentwicklung erweitert. Umfassende Benchmarks gegen JOREK-STARWALL und CarMa0NL wurden durchgeführt, um ihre Zuverlässigkeit aufzuzeigen. Dies wird die Einbeziehung realistischer magnetischer Diagnostik, Abschirmeffekte und die Interaktion zwischen nicht-achsensymmetrischen Plasmen und Wandstrukturen in der Zukunft ermöglichen.

List of publications and conference contributions

First/Second Author Journal Articles

N. Schwarz, et al. *Experiments and non-linear MHD simulations of hot vertical displacement events in ASDEX-Upgrade.* PPCF 65.5 (2023): 054003.

N. Schwarz, et al. *The mechanism of the global vertical force reduction in disruptions mitigated by massive material injection* NF 63 (2023): 126016

N. Isernia, **N. Schwarz**, et al. *Self-consistent coupling of JOREK and CARIDDI: On the electromagnetic interaction of 3D tokamak plasmas with 3D volumetric conductors* PoP 30 (2023): 113901,

Contributions to Journal Articles

V. Mitterauer, et al.; *Non-linear free boundary simulations of the plasma response to resonant magnetic perturbations in ASDEX Upgrade plasmas.* JoP: Conference Series. Vol. 2397. No. 1. IOP Publishing, 2022.

F.J. Artola, et al.; *Non-axisymmetric MHD simulations of the current quench phase of ITER mitigated disruptions* NF 62.5 (2022): 056023

E. Nardon, et al.; *Thermal quench and current profile relaxation dynamics in massive-material-injection-triggered tokamak disruptions.* PPCF 63.11 (2021): 115006.

M. Hoelzl, et al.; *The JOREK non-linear extended MHD code and applications to large-scale instabilities and their control in magnetically confined fusion plasmas.* NF 61.6 (2021): 065001.

First Author Conference and Seminar Contributions

N. Schwarz, et al. (oral); *Simulations and Experiments of hot VDEs*; Hepp autumn colloquium; Garching, Germany; 2023

N. Schwarz, et al. (oral); *Mechanism of the global force reduction in disruptions -experimental validation of mitigated and unmitigated VDEs with the MHD code JOREK*; 29th IAEA FEC; London, UK; October 2023

N. Schwarz, et al. (invited); *The mechanism of vertical force reduction in mitigated disruptions*; TSDW; Princeton, USA; 2023

N. Schwarz, et al. (oral); *Simulations of Vertical Displacement Events in JOREK*; 10th REM Meeting; Garching, Germany; 2023

N. Schwarz, et al. (oral); *The mechanism of vertical force reduction in mitigated disruptions*; ITPA MHD; ITER Organization (virtual); 2023

N. Schwarz, et al. (oral); *SPI mitigated VDEs*; JOREK general meeting; ITER Organization, France; 2023

N. Schwarz, et al. (poster); *Experiments and simulations of hot VDEs in ASDEX Upgrade and JOREK*; IPP theory meeting; Ringberg, Germany; 2022

N. Schwarz, et al. (oral); *Vertical Stability in Tokamaks*; AUG Ringberg meeting; Ringberg, Germany; 2022

N. Schwarz, et al. (invited); *Experiments and non-linear MHD simulations of hot vertical displacement events in ASDEX-Upgrade*; 48th EPS Conference on Plasma Physics (EPS); Maastricht (virtual); 2022;

N. Schwarz, et al. (oral); *Simulations of hot VDEs in ASDEX Upgrade*; JOREK general meeting; Garching, Germany; 2022

N. Schwarz, et al. (poster); *Predictive simulations of Runaway Electron deconfinement by a helical coil*; DPG Spring Meeting; virtual; 2022

N. Schwarz, et al. (oral); *Hot VDE experiments in AUG*; JOREK general meeting; virtual; 2021

N. Schwarz, et al. (poster); *Disruption simulations in ASDEX Upgrade with JOREK-STARWALL*; DPG Spring Meeting; virtual; 2021

Contents

Abbreviations

Physical quantities		**Unit**
$\mathbf{B}$	Magnetic field	[T]
$\mathbf{E}$	Electric field	[$\mathrm{V\,m^{-1}}$]
η	Resistivity	[$\Omega\,\mathrm{m}$]
$\mathbf{J}$	Current density	[$\mathrm{A\,m^{-2}}$]
σ	Conductivity	[$\mathrm{S\,m^{-1}}$]
Φ	Magnetic flux	[$\mathrm{T\,m^{2}}$]
ψ	Poloidal magnetic flux ($\psi = \frac{\Phi}{2\pi}$)	[$\mathrm{T\,m^{2}}$]
n	Number density	[$\mathrm{m^{-3}}$]
p	Pressure	[$\mathrm{N\,m^{-2}}$]
ρ	Mass density	[$\mathrm{kg\,m^{-3}}$]
T	Temperature	[K]
I	Current	[A]
$\mathcal{L}$	Inductance	[H]
$\mathcal{R}$	Resistance	[Ω]
Physical constants		
μ_0	Vacuum permeability	$4 \times 10^{-7}\pi\,\mathrm{H\,m^{-1}}$
ε_0	Vacuum permittivity	$8.858 \times 10^{-12}\,\mathrm{F\,m^{-1}}$
e	Electric unit charge	$1.9 \times 10^{-19}\,\mathrm{C}$
k_B	Boltzmann constant	$1.38 \times 10^{-23}\,\mathrm{J\,K^{-1}}$
Tokamak quantities		
a	Minor Radius	[m]
κ	Elongation of plasma cross-section	[–]
q	Safety factor	[–]
R	Major Radius	[m]
ϕ, θ,z	toroidal, poloidal angle, vertical coordinate	[rad],[rad],[m]
General abbreviations		
AUG	**A**SDEX **U**pgrade	
CQ	**C**urrent **Q**uench	
HPC	**H**igh **P**erformance **C**omputing	
LHS/RHS	Left/ Right Hand Side (of an equation)	
MGI	**M**assive **G**as **I**njection	
MHD	**M**agneto**H**ydro**D**ynamics	
PFC	**P**lasma **F**acing **C**omponents	
PF coil	**P**oloidal **F**ield coil	
PSL	**P**assive **S**tabilizing **L**oop	
SOL	**S**crape–**O**ff **L**ayer	
SPI	**S**hattered **P**ellet **I**njection	
TF coil	**T**oroidal **F**ield coil	
TQ	**T**hermal **Q**uench	
VDE	**V**ertical **D**isplacement **E**vent	

I Introduction

> *Whatever happens will be for the worse, and therefore it is in our interest that as little should happen as possible.*
> – Lord Salisbury

The tendency of physical systems to evolve towards lower energy states determines their stability and dynamical behavior. This fundamental principle sets significant challenges in the quest for fusion energy, as will be outlined at the end of this chapter. Prior to that, we discuss the basics of nuclear fusion in section I.1, one particular kind of device, the tokamak, in section I.2 and its properties in section I.3. This is followed by a physics model of plasmas and its stability in section I.4 and finally, the goal of this thesis in section I.5.

I.1 What is fusion?

Fusion is the process of combining two nuclei to form a larger one. When the binding energy per nucleon increases, as in the case of elements lighter than iron, this process releases energy. Consequently, the mass of the fusion product is smaller than the two original nuclei combined, where the difference is released in the form of kinetic energy according to the well-known formula $\Delta E = \Delta m c^2$. Fusion scientists work towards using this process to create an electricity source with a small carbon footprint[1]. The most promising reaction for a reactor is the fusion of the hydrogen isotopes deuterium ($^2_1\mathrm{H}$) and Tritium ($^3_1\mathrm{H}$):

$$^2_1\mathrm{H} + {}^3_1\mathrm{H} \rightarrow {}^4_2\mathrm{He} + {}^1_0\mathrm{n} \quad (17.6\,\mathrm{MeV}). \tag{I.1}$$

It is particularly favorable because the peak of its cross-section occurs at temperatures of several tens of keV [Wes11], achievable in realistic devices, and the maximum cross-section is larger than for other candidate reactions. The product consists of a helium nucleus and a neutron, with the latter carrying most of the energy (14 MeV) [Che16] intended to serve a double purpose. The first is to heat a suitable fluid for a steam turbine to generate electricity that is eventually supplied to the electrical grid. The second is to create Tritium in a nuclear reaction to provide further fuel for reaction (I.1). The latter process is necessary as Tritium is exceptionally scarce in nature due to its half-life of 13 yr [Wes11]. Therefore, a future power plant must obtain the tritium fuel self-sufficiently by **breeding**, where a reaction of a neutron with Lithium ($^6_3\mathrm{Li}$) is the most promising. The remaining energy is carried by the α-particle ($^4_2\mathrm{He}^{2+}$). While normal chemical reactions release energies in the order of eV, nuclear fusion and fission reactions exceed this value by a million times and thus require less fuel than coal or gas power plants to obtain the same amount of usable energy.

---

[1] The reaction itself does not produce any CO_2. However, constructing a suitable reactor, transporting materials, etc. will cause emissions.

To reach the minimum requirements for a self-sustaining reaction, called **ignition condition**, the product of temperature T, density n, and confinement time τ_e has to fulfill the following [Wes11]:

$$nT\tau_e \geq 5 \times 10^{21}\,\mathrm{keV\,s\,m^{-3}}, \tag{I.2}$$

which is the specific threshold for devices operating based on magnetic confinement that will be introduced in section I.2. Under such conditions, the electrons are stripped from the nucleus, and both are thus susceptible to the influence of electromagnetic fields and their collective motion. This state is called the **plasma state**. Plasmas have the following properties:

Charged particles move in a way to screen electric fields on length scales beyond the characteristic Debye length:

$$\lambda_D = \sqrt{\frac{\varepsilon_0 k_B T_e}{n_e e^2}}, \tag{I.3}$$

where ε_0 is the vacuum permittivity, k_B the Boltzmann constant, T_e and n_e the electron temperature and density and e the electron charge. This property called **quasi-neutrality** leads to an approximate equilibrium of charge densities with $n_e \approx Zn_i$, where Z is the effective ion charge and n_i is the ion density.

In the presence of a magnetic field of strength B, charges gyrate around the field line with an average radius of motion:

$$r_L = \frac{mv_\perp}{qB}, \tag{I.4}$$

named the **Larmor radius** determined by the velocity $v_\perp$ perpendicular to B, the electric charge q and mass m, at the **gyration frequency**:

$$\Omega = \frac{qB}{m}. \tag{I.5}$$

Due to the different masses of electrons and ions, the Larmor radius and gyration frequency differ by a factor of $\frac{m_i}{m_e}$.

For a collection of charged particles to behave like a plasma, the following conditions must be met [Che16]. The size of the system L must be large compared to the Larmor radius $L \gg r_L$, the number of particles inside a sphere of radius λ_D must be large ($\frac{4}{3}\pi\lambda_D^3 n \gg 1$) and the characteristic time of the plasma oscillation ω has to be larger than the mean time between two collisions τ_c: $\omega\tau_c > 1$.

Several pathways lead to achieving fusion-relevant conditions of sufficient density, temperature, and confinement time. One is via the large density route as done in stars and inertial confinement fusion (ICF), where the fuel is compressed by gravity or laser beams, respectively. The other method is confinement by magnetic fields (**magnetic confinement fusion (MCF)**), where lower densities and higher confinement times ($\tau \approx 1\,\mathrm{s}$, $n_e \approx 1 \times 10^{20}\,\mathrm{m^{-3}}$) compared to ICF ($\tau \approx 1 \times 10^{-10}\,\mathrm{s}$, $n_e \approx 1 \times 10^{31}\,\mathrm{m^{-3}}$) are aimed for. While the former method has progressed over the years [Zyl22], MCF is closer to the goal of sustained fusion as the technology allows longer confinement times, and the heating systems are more energy efficient compared to the high-energy lasers used in ICF. MCF is based on the principle that charged particles gyrate around magnetic field lines, so that the magnetic topology can be optimized for confining plasma in a *magnetic cage*. Although there is a diversity of concepts in magnetic confinement research, only the most advanced concept, the so-called tokamak, will be presented in the following since it is the main focus of this thesis.

I.2 Tokamaks

Among the possible geometries for plasma confinement by a magnetic field, the **tokamak** (an abbreviation of "*toroidal chamber with an axial magnetic field*" in Russian [Che16]) is one of the simplest ones as it is based on an approximately toroidally symmetric geometry. The concept was first developed in Russia in the 1950s [Sha01] by A.D. Sakharov and I. E. Tamm after an initial idea was brought forth by the soldier O. Lavrentiev [Bon01].

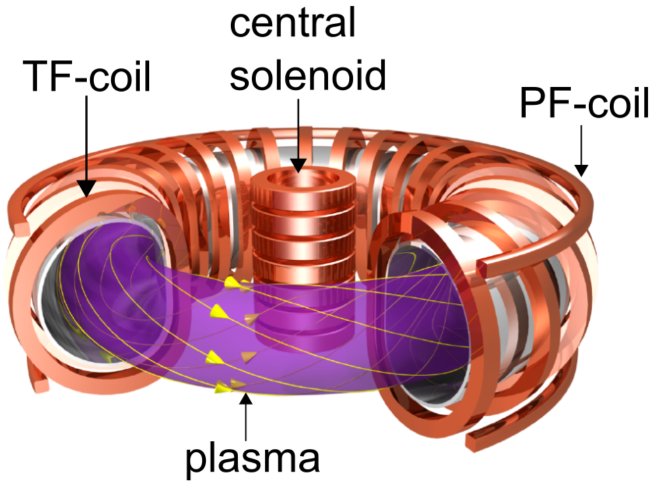

Figure I.1: The principle setup of a tokamak: A helical magnetic field is created by a combination of the large toroidal field produced by TF coils and a current induced by the central solenoid in the center of the device. The PF coils regulate the position and shape of the plasma. The plasma is enclosed by a conductive shell (silver) to counteract instabilities. (Figure from [Gar23])

The inner tokamak plasma has the shape of a torus, as shown in figure I.1, to prevent end losses at magnetic field lines intersecting with structures. Instead, the field lines circle perpetually inside the domain without connecting to the surrounding components. The main toroidal magnetic field B_ϕ is typically one to two orders of magnitude larger than the poloidal one and created by a set of D-shaped toroidal field (TF) coils indicated in figure I.1. The poloidal component of the field B_θ is required to cancel radial particle drifts that would lead to losses [Che16]. In tokamaks, B_θ is created by the central solenoid (CS) in the center of the torus acting as a transformer to drive a **toroidal plasma current** with the plasma as the secondary winding. However, this concept limits the discharge duration, so that advanced methods for the current drive are investigated for continuous operation [Gor07].

Additionally, poloidal field (PF) coils surround the device for shape and position control. The structures closest to the plasma are called plasma facing components (PFCs) and are designed to withstand large heat loads, minimize plasma pollution by impurities, and prevent tritium retention in a reactor environment. The latter usually consist of a carbon or metal-based material, where tungsten is particularly favorable due to its high melting point and low tritium retention rate. These structures are surrounded by a conductive wall and additional large conductive structures that interact with the plasma by induced eddy currents. Thanks to this, specific kinds of plasma instabilities can be suppressed or slowed down, allowing for their active control. In a nuclear reactor, blanket structures are needed as additional components located inside the coils, which a) shield the superconducting coils from neutron damage and heating, b) host the Lithium needed for the breeding reaction, and c) absorb the neutrons, so that the resulting heat can be transported to turbines by a coolant. An additional high-Z material outside the blanket reduces the remaining neutron flux [Wes11].

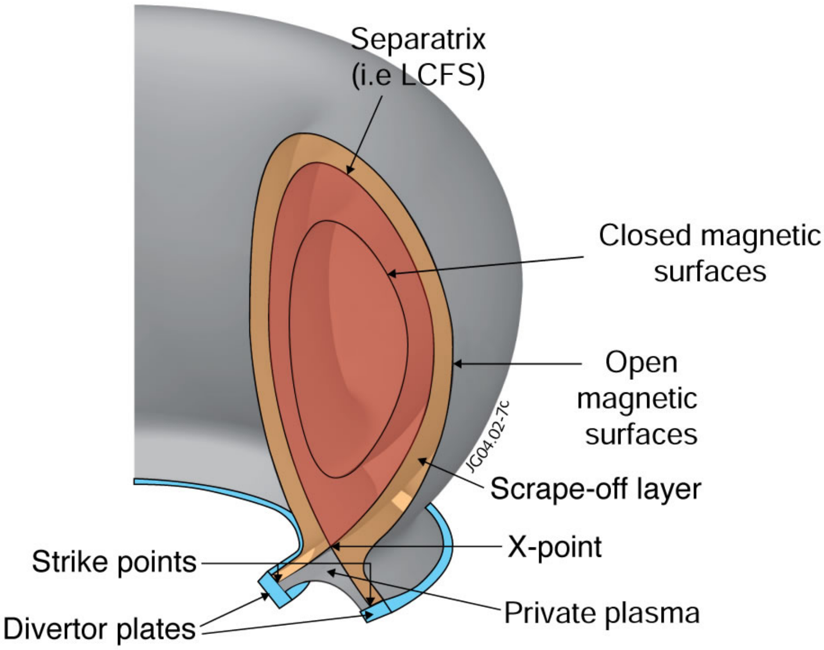

Figure I.2: The core plasma (confined region) is limited by the separatrix. Outside, the SOL is located, which separates the core from the PFCs. On the divertor plates, the field lines intersect with the surrounding structures. (Figure from [Fus07])

The plasma itself can be subdivided into different regions as shown in figure I.2: Inside the core, the magnetic field lines stay on closed surfaces and are not directly connected to the PFCs. Hence, it is referred to as the confined region, bounded by either a physical limiter or a separatrix. In the latter case, the PF coils control the shape, producing a diverted plasma with one or two X-points where $B_\theta = 0$. The case of a lower X-point is illustrated in figure I.2. In an axisymmetric equilibrium, the magnetic field lines in the confined region circle helically around the torus on so-called flux surfaces. In contrast to the closed field line region in the core, the volume outside is referred to as the open field line region. Outside the core, the temperature and density drop sharply in the scrape-off layer (SOL). The interaction with the PFCs defines the SOL characteristics as the magnetic field lines are directly connected to the surface at the legs. This region, named divertor, is designed to spread the heat fluxes, e.g., by minimizing the incidence angle of magnetic field lines, and to withstand thermal stresses.

Since the first tokamaks were developed in Russia, the confinement has been steadily improved, leading to higher achievable temperatures and longer confinement times. With increasing tokamak size, the performance has increased by orders of magnitude approaching reactor conditions as illustrated in figure I.3. The tokamak at IPP Garching, ASDEX Upgrade (AUG), is a medium-sized tokamak with a divertor and PFCs made of tungsten, which has been in operation since 1991 [Kal21]. Its major radius is 1.65 m, the main toroidal field can be up to 2.5 T in the core, and it can sustain a plasma current of up to 1.2 MA or higher in specific conditions. The experiments presented in section III were carried out in this machine.

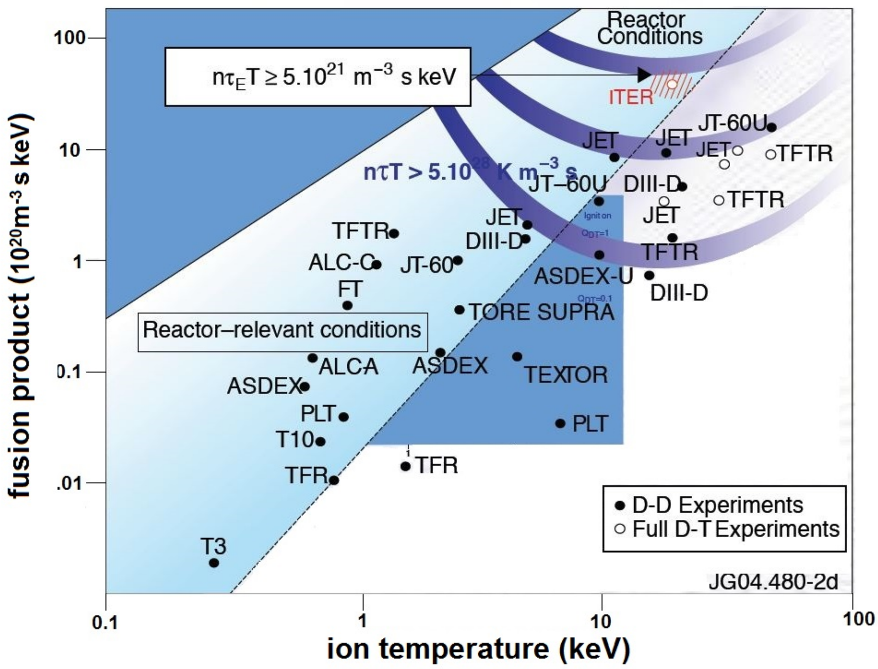

Figure I.3: The triple product of the temperature T, the density n and the energy confinement time τ_E indicates the distance to power plant relevant conditions. The evolution of the achieved fusion product over the years is shown in this figure. Since the earliest devices started operation, its value has increased by orders of magnitude. (adapted from from [Fus07])

While the initial startup in future power plants and conventional tokamaks relies on external heating systems like Ohmic heating, neutral beam injection (NBI), or resonant wave heating, the α-particles produced in a burning plasma remain confined and can thus be used for self-heating. A substantial breakthrough was the discovery of the high confinement regime (**H-mode**) [Wag84] accessible beyond a certain threshold of heating power, leading to the formation of an edge transport barrier and therefore better confinement [Wag07]. The H-mode allowed for a doubling of the confinement time with respect to the low confinement regime (L-mode) and higher energy content at equal heating power [Wag07]. Reaching the H-mode was a significant step towards fusion reactor-relevant conditions, with ignition being a goal in particular.

The minimum requirement to reach **ignition** is to fulfill equation (I.2). At this point, the self-heating by the confined α-particles balances the heat losses, rendering external heating unnecessary. Consequently, Q_{sci}, the ratio of the fusion power released by the nuclear reactions and the heating power that reaches the plasma

$$Q_{\mathrm{sci}} = \frac{\text{fusion power from reactions}}{\text{input heating power}}, \tag{I.6}$$

becomes infinite. Another meaningful milestone towards ignition is reaching a Q_{sci} of 1, the so-called break-even point, where the fusion power balances the external heating power. In order to obtain a net energy gain from a fusion power plant, we also have to consider the power used for the facility operation, losses of the heating systems, and losses from converting the energy carried by the neutrons into electric power. When these effects are taken into account, we speak of the engineering Q_{eng}:

$$Q_{\mathrm{eng}} = \frac{\text{electric output power}}{\text{operating power}}, \tag{I.7}$$

where the operating power contains the average power used by the power plant, and the electric output power is the power supplied to the electrical grid. Reaching a $Q_{\mathrm{eng}} > 1$ is one of the necessary conditions for a fusion power plant to become economically viable. Q_{sci} differs from Q_{eng} by a factor of 5 to 10 for a tokamak [Men11]. In order to demonstrate the capabilities of tokamaks, the largest device so far, named **ITER**, is currently under construction in Cadarache, France. Its goal is to obtain steady-state scenarios, a fusion output of 500 MW with a $Q_{\mathrm{sci}} \geq 10$, self-heating by α-particles and testing of tritium breeding as well as relevant technologies for fusion power plants (like heating systems, remote handling capabilities, etc.) [Org18].

I.3 Properties of tokamak plasmas

In the following, an appropriate coordinate system for tokamaks and important plasma quantities are defined. Due to the toroidal shape, cylindrical coordinates (R, Z, ϕ) are used, which defines a point by the major radius R indicating the distance to the center of the torus, the vertical coordinate Z and the toroidal angle ϕ as depicted in figure I.4.

An axisymmetric equilibrium is characterized by nested surfaces of constant poloidal magnetic flux ψ, the flux surfaces. Therefore, ψ is commonly used as a radial coordinate instead of the minor radius r. Where ψ is the magnetic flux

$$\psi = \int_{S_p} \mathbf{B} \cdot \mathrm{d}\mathbf{S}_p \tag{I.8}$$

through an area $\mathbf{S}_p$ defined by a toroidal ribbon originating from the plasma center as shown in [Fre14, ch. 4.6.1]. The center of the core is characterized by a vanishing gradient of ψ and is called the **magnetic axis**. Based on this, the normalized poloidal flux is defined as

$$\psi_N = \frac{\psi - \psi_{\mathrm{axis}}}{\psi_{\mathrm{boundary}} - \psi_{\mathrm{axis}}}, \tag{I.9}$$

where ψ_{axis} and ψ_{boundary} are the values of ψ on the magnetic axis and boundary of the confined

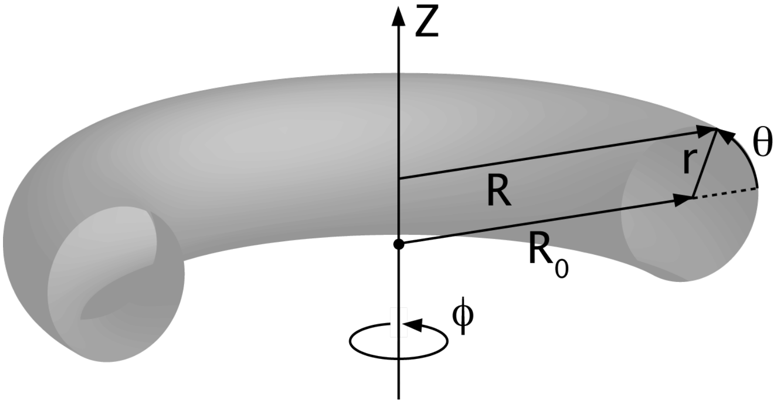

Figure I.4: A cylindrical coordinate system (R, Z, ϕ) is used to describe tokamak plasmas. The major radius R defines the distance to the center of the torus, while the minor radius r denotes the distance to the plasma center in a circular plasma. The toroidal angle ϕ and poloidal angle θ are used to describe the respective positions. The vertical coordinate is given by Z.

region, respectively. The separatrix or limiting surface is called the Last Closed Flux Surface (LCFS) as it separates the closed field line region in the core from the open field line region as illustrated in figure I.2.

The poloidal angle θ is defined from the outboard midplane at the Z-position of the magnetic axis. The toroidal magnetic field in vacuum falls off from the center of the torus with a R^{-1} dependence, where it increases or decreases inside the plasma region depending on the diamagnetic properties of the plasma. The ratio between the mean plasma pressure in the full plasma volume V and the mean magnetic pressure of B_θ on the LCFS

$$\beta_p = \frac{\langle p \rangle_V}{\langle B_\theta^2 \rangle_{LCFS} / 2\mu_0}, \tag{I.10}$$

defines if the plasma the diamagnetic properties. Diamagnetic plasmas have a $\beta_p > 1$; thus, B_ϕ decreases slightly in the plasma domain and paramagnetic plasmas have a $\beta_p < 1$.

Due to the decrease of B_ϕ with increasing R, the outboard side of the plasma is referred to as the low field side (LFS), while the inboard side located closer to the CS is called the high field side (HFS). The value of β describes the ratio of the average plasma pressure $\langle p \rangle_V$ to the magnetic pressure:

$$\beta = \frac{\langle p \rangle_V}{|B|^2 / 2\mu_0}, \tag{I.11}$$

where B is usually taken as a combination of the toroidal field in vacuum on the axis and the poloidal field is defined as for β_p.

The poloidal beta also indicates how much the magnetic axis is shifted towards the LFS with respect to the geometric center of plasma, called the **Shafranov shift** Δ_S. It is caused by the plasma pressure and the weaker magnetic pressure on the LFS and its magnitude depends on the specific equilibrium and the current distribution. The latter is characterized by the normalized **internal inductance** l_i of the plasma, which is a measure of the shape of the current profile.

It is defined as [Fre14]:

$$l_i = \frac{2L_i}{\mu_0 R_0}, \tag{I.12}$$

$$\text{with} \quad \frac{1}{2} L_i I_p^2 = \int_{\text{plasma}} \frac{B_\theta^2}{2\mu_0} \mathrm{d}V \tag{I.13}$$

where L_i is the internal inductance, and R_0 is the major radius of the plasma center. The smaller l_i, the flatter the current profile with a value of 0.5 corresponding to a uniform current inside the domain.

The existence of a larger magnetic field strength region on the HFS has an important consequence for the motion of particles along the magnetic field lines. Both the magnetic moment $\mu_B = \frac{mv_\perp^2}{2B}$ originating from the gyration around $\mathbf{B}$ and the kinetic energy of the particle $\frac{1}{2}m(v_\parallel + v_\perp)^2$ are conserved quantities, where $v_\parallel$ is the velocity along $\mathbf{B}$. For increasing B, the perpendicular velocity $v_\perp$ increases accordingly to keep μ_B constant, while, simultaneously, $v_\parallel$ decreases to conserve the kinetic energy. Therefore, only particles with sufficiently high $v_\parallel$ enter the high field region, the others are reflected back into the LFS. They are respectively named **passing** and **trapped** particles. The same phenomenon, named **magnetic mirror**, occurs on the magnetic poles on the earth, where similarly certain charged particles are reflected as B increases closer to the poles. When the trajectory of the trapped particles is projected on the poloidal plane, it has the form of a banana, thus, named *banana orbit*.

An important parameter for tokamak plasmas is the pitch angle of the helical magnetic field lines. Based on this, the **safety factor** q is defined as the number of toroidal turns per poloidal turn when following a magnetic field line along the torus:

$$q(\psi) = \frac{\mathrm{d}\phi}{\mathrm{d}\theta}, \tag{I.14}$$

which increases in standard tokamak scenarios from finite values at the magnetic axis to infinity at the separatrix plasmas with an X-point. Therefore, the value of q at a ψ_N of 95 % is taken as a proxy for the safety factor at the edge. On rational surfaces, where the magnetic field lines close upon themselves after m toroidal and n poloidal turns, q can be expressed as a rational number $\frac{m}{n}$. These surfaces are prone to various classes of instabilities, which will be described in the following section.

I.4 Mathematical description and instabilities

In order to understand the dynamics of a plasma, we need mathematical models to describe its properties and evolution. The most straightforward way of following the charged particles becomes computationally infeasible due to the large number in the order of 1×10^{20}. Instead, the system can also be described by a set of equations looking at the plasma as a fluid while taking into account electromagnetic effects. Therefore, the model is named **m**agneto-**h**ydro**d**ynamics (**MHD**). This approach focuses instead on the evolution of macroscopic quantities like density and temperature, rather than the position of single particles. The formulation and limits of this description will be discussed in more detail in section II.1. One important goal of MHD is to describe the stability of the plasma for a given configuration. Here, general arguments will be made for the stability, which will be detailed in section II.1.2 and can be found in MHD textbooks like [Bis93, Fre14, Goe04].

In order to understand the stability of the system, the response to an arbitrary perturbation from its equilibrium is considered. The evolution of the displacement ξ of the plasma from its equilibrium can be described by a force operator **F**:

$$\rho\ddot{\xi} = \mathbf{F}(\xi), \tag{I.15}$$

which we identify as Newton's second law. The energy change δW associated with the displacement can be expressed in the form of the **energy principle** [Bis93, eq. 4.21]:

$$\delta W \equiv -\frac{1}{2}\int \xi \cdot \mathbf{F} \mathrm{d}^3 x \tag{I.16}$$

If $\delta W \geq 0$ for all displacements ξ, the equilibrium is stable as any small perturbation would increase the energy. A plasma will explore all possible eigenstates to search for the lowest energy state. Therefore, if a perturbation exists with $\delta W < 0$, the associated instability will occur. Non-linear theory is then required to determine if this state will lead to turbulence, a saturated quasi-stationary state, a transient relaxation, or even the termination of the discharge.

MHD theory describes a variety of large scale instabilities, which can be classified by the following different characteristics.

- The *instability drive*: E.g. pressure gradients and current densities are typically responsible for causing instabilities, limiting the safe operation region.
- The *influence of resistivity*: If the plasma resistivity η influences the growth rate and the field line topology changes, the instability is called resistive. If the instability also occurs in ideally conducting plasmas, it is ideal.
- The *location of the instability*: Which can be in the core or at the edge. In particular, instabilities can be associated with certain rational flux surfaces $q = \frac{m}{n}$.
- Some instabilities that interact with conductive structures can be slowed down to the resistive time scales of the wall by electromagnetic interaction.

The books [Igo15, Zoh15] describe a variety of MHD instabilities and their experimental observation in tokamaks. Instabilities of the same class are referred to as *modes*. Of particular importance for disruption are so-called tearing modes, where field lines reconnect to form island structures. They are associated to rational surfaces m/n that determine their structure. Furthermore, kink modes are associated to a deformation of flux surfaces either inside the core (*internal kink mode*) or at the plasma edge (*external kink mode*).

Tokamaks are especially prone to particular classes of instabilities because of the drive provided by the large plasma current. Large scale instabilities can lead to a loss of the stored energy in the plasma in an event called **disruption**. Consequences of disruptions are large heat loads, electromagnetic forces on the encompassing structures as well as the conversion of a considerable part of the plasma current into relativistic electrons, which can lead to the melting of PFCs. The electrons accelerated by the latter phenomenon are called runaway electrons (REs), which are mainly a concern in high current devices. The damage becomes more destructive the larger the stored thermal and magnetic energies in plasmas, which are, however, essential for power plant operation. Therefore, the causes and consequences of disruptions have to be understood to avoid machine downtime due to damages in future operation or premature material aging.

This work focuses on one phenomenon associated with disruptions, the **vertical displacement event (VDE)**. High elongations, favorable for plasma confinement, are created by PF coils that produce a quadrupole field in the plasma center. When the plasma experiences a small displacement from its equilibrium position, it is accelerated by this field in direction of the perturbation. Therefore, elongated plasmas are unstable to vertical displacements. In the presence of a conducting wall, the motion is slowed down to the time scale of the resistive wall $\tau_{L/R}$ such that it can be actively controlled by fast control coils. VDEs can be categorized into two types. In the case of a *hot VDE*, caused, e.g., by a control system failure, the plasma drifts vertically into the PFCs on the time scale of $\tau_{L/R}$, eventually resulting in the fast loss of the stored energy. This type of event is associated with the largest forces and heat loads, as the plasma comes into contact with the wall at a high temperature and current. The second type of VDE occurs after a thermal quench caused by an instability or radiation collapse, where the plasma becomes vertically unstable and drifts into the wall at a lower temperature compared to the hot VDE and reduced plasma current. Therefore, it is sometimes referred to as a *cold* VDE. In these events, radiation plays an essential role to balance the Ohmic heating by the current density.

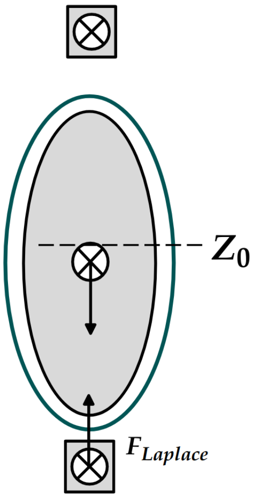

Figure I.5: PF coils produce an elongated plasma shape, which is favorable for confinement. However, this makes the plasma unstable to vertical displacements due to the $\mathbf{J}\times\mathbf{B}$ force by the PF coils. Placing the plasma into a closely fitting conductive shell slows the motion by the induction of eddy currents. (Own illustration)

Today's tokamaks can usually handle the disruption stresses within certain limits. Therefore, they can also study non-mitigated scenarios to understand their cause, dynamics, and consequences in order to make predictions for future machines.

I.5 Thesis goal and structure

There are several major scientific challenges on the way of building a fusion power plant. Among them are optimizing transport to obtain long confinement times while avoiding the accumulation of impurities and fusion products in the core, defining stable plasma scenarios not degraded by transient events, and finding materials that can withstand large neutron fluxes over a long period without polluting the machine.

One particular challenge is solving the problem of disruptions. The fast loss of the stored energy can reduce the lifetime of the components and cause additional downtime for the facility. Therefore, it is crucial to understand the causes and consequences of disruptions to identify a safe operational space and mitigation techniques. This can be done by using computational methods and physical models to explore the effects of disruptions on future machines. However, in order to build trust in these models and assess their reliability, it is necessary to validate them against experimental data.

Towards this goal, this thesis aims to validate the extended MHD code JOREK in its free boundary version against dedicated experiments in ASDEX Upgrade to test the validity limits of this model for VDEs. In particular, we are interested in reproducing experimental data and investigating the influence of boundary conditions, conductive structures, and various parameters on the results. Furthermore, the JOREK model is enhanced by coupling it to the volumetric EM code CARIDDI, which can represent realistic structures derived from CAD models of machines. This will allow us to study the effects of 3D structures on the plasma dynamics and allow a more realistic inclusion of magnetic measurements.

The manuscript is structured in the following way: At first, the necessary background is presented in section II, which includes an introduction to MHD theory in section II.1, an overview about the plasma wall interaction in section II.2, a summary of the theory and experimental observations of disruptions in II.3, diagnostics relevant for disruptions in section II.4 and concludes with a presentation of the MHD code JOREK and the EM code STARWALL used for modeling the experimental results in section II.5. In the following chapter III, the dedicated experiments as part of this thesis and their results are presented, where first the unmitigated disruptions are described in section III.1, followed by mitigated disruptions in section III.2. The simulation results based on these experiments are analyzed in chapter IV, which is subdivided into axisymmetric simulations of the unmitigated disruptions in section IV.2, extended by 3D simulations in section IV.3. The chapter then concludes with validating the mitigated disruptions in section IV.4. After the validation work, the code coupling between JOREK and CARIDDI is lined out in section V, where first the implementation is described in sectoin V.1 and benchmarks are carried out in section V.2 before continuing with a study of the influence of realistic wall structures on the dynamics of a disruption in section V.3. In the end, the results of the work are summarized in section VI with an outlook towards future work.

II Theoretical background and previous experiments

> *As we embark on this fusion-powered odyssey, let's not only aim to conquer the stars but also the unruly tantrums of plasma instabilities—after all, even the sun occasionally has a bad hair day.*
> – ChatGPT

Large scale dynamics in tokamak plasmas can be described by magnetohydrodynamic (MHD) models. This thesis makes use of these to perform simulation studies of VDEs with the extended MHD code JOREK based on dedicated experiments in ASDEX Upgrade. In preparation for the results of the work, this chapter aims to provide a comprehensive overview of the theoretical, computational and experimental background. First, the theoretical background of MHD theory is presented in section II.1, which is complemented by a short summary of plasma wall interaction in II.2. The experimental observations and theory of disruptions are laid out in section II.3 before the diagnostic systems used for this thesis are described in section II.4. Finally, the modeling codes are introduced in section II.5 comprised of the non-linear MHD code JOREK in section II.5.1, which is coupled to the electromagnetic wall code STARWALL II.5.2.

II.1 Magnetohydrodynamics (MHD)

MHD theory mainly serves to make predictions about stability characteristics of plasma states and their dynamics during transient events. Towards this goal, understanding the evolution of macroscopic quantities like temperature and density is the primary objective. The name of the model originates from its description of the plasma as a fluid, where the structure of the equation reminds of fluid dynamics with the addition of long range effects by electromagnetic fields. The fundamentals and limits of this theory are described in the subsequent sections, following literature about MHD provided in [Bis93, Fre14, Goe04].

II.1.1 Fluid description of the plasma equations

The macroscopic equations are derived from fine-scale dynamics in the following way. A collection of particles of species α can be described by its distribution function $f_\alpha(\mathbf{x}, \mathbf{v}, t)$, a probability density in phase space, which evolves according to the Boltzmann equation:

$$\frac{\partial f_\alpha}{\partial t} + \mathbf{v} \cdot \frac{\partial f_\alpha}{\partial x} + \frac{q_\alpha(\mathbf{E} + \mathbf{v} \times \mathbf{B})}{m_\alpha} \cdot \frac{\partial f_\alpha}{\partial \mathbf{v}} = \left.\frac{\partial f_\alpha}{\partial t}\right|_{\text{collisions}}, \tag{II.1}$$

where the right hand side (r.h.s.) denotes the change of the distribution function by collisions between particles of the same or different species. The force term $q_\alpha(\mathbf{E}+\mathbf{v}\times\mathbf{B})$ originates from the Lorentz force and contains both external fields and self-generated fields by the collection of particles. Gaining insight about this evolution is the main objective of **kinetic theory**.

By taking velocity moments of different orders, one arrives at the evolution of the number density n, the velocity $\mathbf{v}$ and the temperature T, and higher order quantities. The change of the r.h.s. is determined by transport theory, which takes into account classical transport due to a) Coulomb collisions, b) neo-classical transport due to particle motion in toroidal geometry with curved field lines and trapped particles (see section I.3) as well as c) turbulent (anomalous) transport resulting from small scale fluctuations due to micro-instabilities.

These external assumptions are necessary to close the system of equations and determine the change of momentum and energy due to interactions between particles. A further simplification can be obtained by combining the fluid descriptions of the ions and electrons into a single fluid, leading to the MHD equation, for which further generalizations and extensions exist beyond the model described in the following.

Structure of the MHD equations By taking the velocity moments of (II.1), we arrive at a collection of conservation laws closed by an equation for the magnetic field evolution. The plasma is described by the mass density ρ, temperature T, the fluid velocity $\mathbf{v}$, the current density $\mathbf{J}$ and the total magnetic field by external and internal currents $\mathbf{B}$. The resistive MHD equations are presented in the following to show the principle structure of the equations.

$$\begin{align}
\frac{\partial \rho}{\partial t} + \boldsymbol{\nabla} \cdot (\rho \mathbf{v}) &= \boldsymbol{\nabla} \cdot (\underline{\mathbf{D}} \boldsymbol{\nabla} \rho) + S_\rho && \text{(continuity equation)} \tag{II.2a} \\
\rho \frac{\partial \mathbf{v}}{\partial t} + \rho(\mathbf{v} \cdot \boldsymbol{\nabla})\mathbf{v} &= -\boldsymbol{\nabla} p + \mathbf{J} \times \mathbf{B} + \boldsymbol{\nabla} \cdot \underline{\mathbf{P}} && \text{(momentum equation)} \tag{II.2b} \\
\frac{\partial p}{\partial t} + \mathbf{v} \cdot \boldsymbol{\nabla} p &= (\gamma - 1)\eta \mathbf{J}^2 - \gamma p \boldsymbol{\nabla} \cdot \mathbf{v} \nonumber \\
&\quad + (\gamma - 1)\boldsymbol{\nabla} \cdot (\underline{\kappa} \boldsymbol{\nabla} T) + (\gamma - 1)\underline{\mathbf{P}} : \boldsymbol{\nabla} \mathbf{v} && \text{(energy equation)} \tag{II.2c} \\
\frac{\partial \mathbf{B}}{\partial t} &= \boldsymbol{\nabla} \times (\mathbf{v} \times \mathbf{B}) - \boldsymbol{\nabla} \times (\eta \boldsymbol{\nabla} \times \mathbf{B}) && \text{(induction equation)} \tag{II.2d}
\end{align}$$

The continuity equation (II.2a) is a result of the conservation of particles and can be extended by external sources S_ρ originating from fueling, recombination and ionization or changes due to nuclear reactions in burning fusion plasmas. These can change the total number of particles of one species. $\underline{\mathbf{D}}$ is the diffusion coefficient of the particle density, which can be an-isotropic.

In the momentum equation (II.2b), the pressure tensor is commonly reduced to its isotropic contribution p and the off-diagonal elements $\underline{\mathbf{P}}$ are represented by $\nu \boldsymbol{\nabla} \mathbf{v}$, where ν is the scalar, kinematic viscosity. The force terms originate from the pressure term and the $\mathbf{J} \times \mathbf{B}$ contribution.

The pressure equation (II.2c) includes the effect of resistivity η, which also appears in the induction equation for the magnetic field evolution (II.2d). Due to the movement of charges along magnetic field lines leading plasma an-isotropies in presence of strong magnetic fields, the heat transport in direction of $\mathbf{B}$ is much faster than the perpendicular one. Therefore, the heat diffusion coefficient along the magnetic field $\kappa_\parallel$ is orders of magnitude larger than the perpendicular one. The adiabatic index γ is usually taken as 5/3 for plasmas.

In the limit of vanishing dissipation and resistivity, the following applies:

$$\underline{\mathbf{P}} = 0, \quad \eta = 0, \quad \underline{\kappa} = 0, \quad \nu = 0 \quad \text{and} \quad \underline{\mathbf{D}} = 0, \tag{II.3}$$

and the equations (II.2) reduce to the ideal MHD equations. In this limit, the magnetic field lines are *frozen into the fluid*, meaning that they move with the fluid elements due to flux conservation (see e.g. [Fre14, ch. 3.5]). As a consequence, the magnetic topology cannot change, so that initially nested flux surfaces can deform but cannot break up during the evolution of the plasma. Only when η is finite or effects beyond the basic MHD model are included, the plasma can break up its structures by reconnection.

After presenting the equations and main properties of MHD, we approach the question of MHD stability and the validity of the equations in the following.

II.1.2 The energy principle

The topic of stability theory was already touched upon in section I.4 and will be detailed below. Its fundamental question is, whether a plasma remains close to its equilibrium when small, albeit unavoidable, perturbations occur. The overall stability of the system can be assessed by exploiting the energy principle (I.16). It states that the sign of the energy change δW due to a displacement $\boldsymbol{\xi}$ from its equilibrium indicates if the system is stable (with $\delta W > 0 \rightarrow$ stable), where δW can be categorized into different contributions [Bis93].

The contribution from the plasma volume:

$$\delta W_p = \frac{1}{2} \int_{V_p} \mathrm{d}^3 x \left(|\mathbf{B}_1|^2 + \gamma p |\boldsymbol{\nabla} \cdot \boldsymbol{\xi}|^2 - \boldsymbol{\xi}^* \cdot (\mathbf{J} \times \mathbf{B}_1) + \boldsymbol{\xi}_\perp \cdot \boldsymbol{\nabla} p \boldsymbol{\nabla} \cdot \boldsymbol{\xi}_\perp^* \right), \tag{II.4}$$

where the subscripts $\{1, \perp, ||\}$ denote perturbed quantities and the direction perpendicular or parallel to the equilibrium magnetic field respectively. The quantities without subscript represent equilibrium values. The quantity $\boldsymbol{\xi}^*$ is the complex conjugate of $\boldsymbol{\xi}$, while δW_p remains real due to the self-adjointness of $\mathbf{F}(\boldsymbol{\xi})$ [Bis93]. By looking at the equation above, it is clear that only the terms containing pressure gradients or the current density have negative contributions. Therefore, we identify them as the driving mechanisms of instabilities.

The contribution from the plasma vacuum interface S_p to δW has the following form:

$$\delta W_s = \frac{1}{2} \oint_{S_p} \mathrm{d}\mathbf{S} \cdot \left[\boldsymbol{\nabla} \left(p + \frac{B^2}{2} \right) \right]_S |\mathbf{n} \cdot \boldsymbol{\xi}|^2, \tag{II.5}$$

where $[]_S$ denotes the jump of a quantity at the plasma boundary S_p and $\mathbf{n}$ is the outward normal. This contribution vanishes in the absence of equilibrium surface currents as B as well as p are continuous across S_p.

The last term describes the vacuum contribution:

$$\delta W_V = \frac{1}{2} \int_{V_{\text{out}}} \mathrm{d}^3 x |B_{1V}|^2, \tag{II.6}$$

which quantifies the change in the vacuum energy by integrating the over volume outside the plasma V_{out}. If a perfectly conducting wall is placed at the plasma boundary, δW_V reduces to 0 as the magnetic field outside is frozen. These configurations are in general more stable as an ideal wall excludes a class of instabilities by enforcing $\boldsymbol{\xi}|_{S_p} = 0$. In free boundary cases ($\boldsymbol{\xi}|_{S_p} \neq 0$) and for non-ideal walls, the vacuum contribution is nevertheless stabilizing.

In simple geometries, this method can be directly employed to identify classes of instabilities and their respective stability limits as done in [Fre14, ch. 11], whereas numerical codes are required to assess the stability in more complex configurations. While energy principle is a valuable approach for excluding violently unstable scenarios, it cannot predict the time evolution of a system, in particular, far from its initial equilibrium.

More information can be obtained with the help of non-linear calculations that allow the evaluation of the non-linear stability of a system (e.g. the equilibrium evolves into a more stable state), its non-linear saturation or determine whether it is fully unstable (e.g. leading to a termination of the discharge). Putting it simple, non-linear theory takes into account self-consistent changes in the equilibrium plasma and can thus evaluate the region far from the initial equilibrium. Furthermore, they go beyond stability considerations by describing the dynamics of the system as well as determining quantities of interests like heat fluxes, forces, radiation, etc. that can be used to assess the machine safety.

Non-linear simulations facilitate experimental understanding or the design of future scenarios and machines. One of the tools for investigating the non-linear evolution of a plasma is the extendend MHD code JOREK, that will be presented in section II.5.1. To conclude the introduction into MHD theory, we will describe the limits of the model in the following.

II.1.3 Validity of the MHD model

The MHD equations are valid under several assumptions, the Larmor radius has to be smaller than the system size $r_L \ll L$ and the mean free path λ_{mfp} of Coulomb collisions is short compared to typical variations of quantities $\frac{\boldsymbol{\nabla} f}{f}\lambda_{mfp} \ll 1$, which requires high collisionality [Fre14]. The second condition ensures that the plasma equilibrates on a fast time scale by frequent collisions with particles of the same or different species. While the first assumption is usually satisfied, the latter one is often not true for fusion relevant plasmas.

The second condition can also be represented in terms of typical time scales. To ensure the validity of the fluid description of the plasma constituents, their relaxation times τ_α have to be smaller than the time scale of interest. For electrons, τ_e is $1.09 \times 10^{-4} \frac{T[\text{keV}]^{1.5}}{n[10^{20}\text{m}^{-3}]\ln\Lambda}\text{s}$ [Fre14], where $\ln\Lambda$ is the Coulomb logarithm ranging around 14 to 19 in fusion plasma conditions. For typical conditions ($T_e \approx 1\,\text{keV}$, $n_e \approx 1 \times 10^{20}\,\text{m}^{-3}$), the time scale is around $5\,\mu\text{s}$. For ions, the relaxation time is around a factor of $\sqrt{\frac{2m_i}{m_e}}$ longer. Therefore, some models consider a (gyro-) kinetic description of ions, while the electrons are still described by fluid equations [Bis93]. If these conditions are not fulfilled, the distribution function can deviate from a Maxwellian.

For the one-fluid equations (like MHD) to be valid, the temperature equilibration time τ_{eq} between electrons and ions has to be smaller than the dynamics under consideration. Otherwise, they have to be treated as separate fluids as the temperatures of the species are not the same. Alternatively, the MHD equations can be modified to describe a fluid with distinct temperatures for different species. The time constant τ_{eq} is $\frac{m_i}{2m_e}\tau_e$ and, thus, imposes stronger constraints than the relaxation times of the single species. These conditions predict the conditions for validity quite pessimistically with $\tau_i \approx 0.3\,\mathrm{ms}$ and τ_{eq} in the range of ms. Nevertheless, by taking into account neo-classical effects or turbulence, the effective relaxation times are reduced [Goe04], extending the region of validity of the MHD equations.

In spite of this, the MHD equations have proven to be useful for determining the stability and large scale dynamics of plasmas. This contradiction can be resolved by considering the geometry of the system. Because of the inherent an-isotropy between the direction parallel and perpendicular to the magnetic field resulting from the large toroidal component of $\mathbf{B}$, the effective gradient length in the direction perpendicular to $\mathbf{B}$ is on the scale of the Larmor radius [Fre14, Bis93]. Also, [Bis93] reasons that small scale turbulence acts like phase space mixing similar to collisions. Thus, when the system size is large compared to the Larmor radius, the perpendicular motion is still described reasonably well with the MHD equations. Also, when the plasma is incompressible ($\boldsymbol{\nabla} \cdot \mathbf{v} = 0$), the MHD equations are a good description of the evolution of the parallel momentum and energy [Fre14]. This is however not true for a large range of instabilities in toroidal systems, where compression plays a role.

The validity of ideal MHD $\eta \approx 0$ is formally given for fusion relevant high temperature plasmas. However, when small scale gradients appear, dissipative effects are not negligible any more. The importance of resistive effects is given by the so called magnetic Reynolds number R_m

$$R_m = \frac{vL}{\eta}, \tag{II.7}$$

with the flow velocity v and the length L. When looking at linear growth rates, this number is often replaced by the Lundquist number, where the fluid velocity is replaced by the Alfvén velocity $v_A = \frac{B}{\sqrt{\mu_0 \rho}}$:

$$L = R_m(v = v_A) = \frac{v_A L}{\eta}, \tag{II.8}$$

which is the typical speed of a plasma wave parallel to $\mathbf{B}$ in the system.

In summary, MHD theory can be useful despite the limitations introduced by the time scales of the equilibration times. For certain phenomena the kinetic description is necessary for at least some of the plasma constituents (e.g. only high energetic particles or ions). However, the MHD equations can also be extended to take effects into account in a simplified way that are not contained in the basic MHD model. This is done in the JOREK code presented in section II.5.1. In particular, the effect of energetic particles present due to fusion reactions or heating are not taken into account in the MHD model, while they can also trigger instabilities. Furthermore, outside the LCFS the interaction with the material plays an important role and suitable boundary conditions have to be found to take this into account, which will be laid out in the following.

II.2 Plasma wall interface

The contact with the plasma facing components (PFCs) defines the properties of the edge plasma. In particular, we will see in section IV that the boundary conditions significantly affect the dynamics of the simulated processes. Therefore, the basics of the plasma wall interaction are outlined in the following. A comprehensive review of the physics of the plasma wall interaction can be found in [Sta00]. Recently, Bunkers [Bun19] and Spinicci [Spi23] investigated appropriate boundary conditions for disruption simulations, which was extended here [Art21a] by the use of current density limitations. The relevant physics is described in the remainder of the section following the outline of [Sta00].

Some main properties of the plasma wall interface stems from the high mobility of the light electrons leading to a buildup of a negative charge density at the wall. The resulting electric field accelerates ions and repels electrons except for the high velocity tail of the distribution. At the wall, the ions neutralize by picking up wall electrons and are scattered back into the plasma where they ionize either inside the core plasma or in the SOL. The small volume in which quasi-neutrality breaks down due to the net-charge of the wall is called the **Debye Sheath**, which is in the order of λ_D (defined here (I.3)). In order to keep quasi-neutrality in the plasma, the flux $\Gamma = n_\alpha v_\alpha$ of ions and electrons to the sheath must be equal:

$$n_e v_e = n_i v_i \tag{II.9}$$

Taking this into consideration and several other assumptions (no radiation, re-ionization of ions in the core, high collisionality), the resulting ion velocity must be equal to the sound speed $c_s = \sqrt{(k_B T_e + \gamma k_B T_i)/m_i}$ at the sheath edge. This is known as the **Bohm criterion**.

The voltage of the sheath entrance with respect to the plasma is found to be around $V_{se} = -0.7\frac{k_B T_e}{e}$. In the simple SOL model, the density at the sheath entrance n_{se} is half the density in the upstream plasma.

When an external voltage V_e is applied, a net current depending on V_e, n_{se} and c_s can be present in the SOL. For large voltages, it is limited by the so called **ion saturation current** density:

$$j_\mathrm{sat} = e n_{se} c_s. \tag{II.10}$$

The equation above is valid only in the case of no electron emission from the surface. The external voltage can be applied from outside or be a result from plasma current changes like happening during disruptions.

Furthermore, the considerations above only apply for magnetic field lines perpendicular to the surface. In case of oblique angles of $\mathbf{B}$, the so called magnetic pre-sheath (MPS) with a length in the order of the ion Larmor radius builds up [Mat90, Sta00]. The ion velocity is then modified to $v_i|_{MPS} = c_s \sin(\alpha)$, with α being the angle between the surface and magnetic field. The heat flux q to the boundary is described by:

$$q = \gamma n_e^\mathrm{bnd} k_B T_e c_s \sin(\alpha), \tag{II.11}$$

where n_e^{bnd} is the density at the boundary and γ_{sh} is the sheath transmission factor with a typical value of 7 to 8.

The physics described above gives the most simple assumptions for the sheath properties, which can be used as boundary conditions for MHD simulations. In order to do these calculations self-consistently, the dynamics of neutrals as well as effects like sputtering need to be included as well as the ion-saturation current limit as done in [Art21a]. In section IV.2, we will see that the effects of the SOL will be of particular importance for the VDE dynamics. To understand why this is the case, an introduction into disruptions, their dynamics and consequences is given in the following section.

II.3 Disruptions

Disruptions are defined as fast events that lead to a loss of plasma control and ultimately to the end of a plasma discharge. Due to their detrimental effects on the machine, they are a serious concern for future power plant operation.

Disruptions can be classified into the following categories.

- **Major disruptions** Major disruptions are triggered by large scale MHD instabilities, radiative events, or a number of other reasons [Sch95, Vri11].
- Events with a small loss of thermal energy are referred to as **minor disruptions**.
- **Vertical Displacement Event** As described in I.4, a loss of vertical control can lead to the loss of plasma energy.
- **Radiation dominated disruptions** When the majority of the plasma energy is lost by radiation, the consequences in terms of heat loads and forces are typically less severe. To achieve this, **mitigated disruptions** are intentionally triggered by large amount of material or impurities. Moreover, non-actively mitigated discharges can fall in this category if the radiation is the dominant loss channel.

The general phenomenology of disruptions is described in section II.3.1 before focusing on one type of disruption, the vertical displacement event as the main focus of this thesis in section II.3.2. Currents in the SOL called halo currents are associated with these events, which will be presented in section II.3.3. These can contribute to the electromagnetic forces that are observed in tokamak disruption and which will be introduced in section II.3.4. Finally, the negative effects of disruption need to be alleviated by suitable techniques. In particular, the mitigation of disruptions by shattered pellet injection is discussed in section II.3.5.

II.3.1 Dynamics and causes of disruptions

A disruption can be antipicated by a precursor, e.g. a rise of radiation levels or enhanced MHD activity [Sch95, Wes89]. Detecting early signs of disruptions allows for preventive measures by leading the plasma back into a stable state or initiating a controlled shutdown.

If this is not possible, the disruption event chain will be initiated, as described in the following and summarized in the diagram in figure II.1. It typically starts with a fast reduction of thermal energy E_{th} known as the **thermal quench (TQ)**. Prior to this, up to 30 % [ITE99, Pau03] or even the majority of E_{th} [Loa04] can already be lost on a time scale of several ms to s due to performance degradation or reactions of the control system. In the following, the dynamics of the TQ are described in more detail.

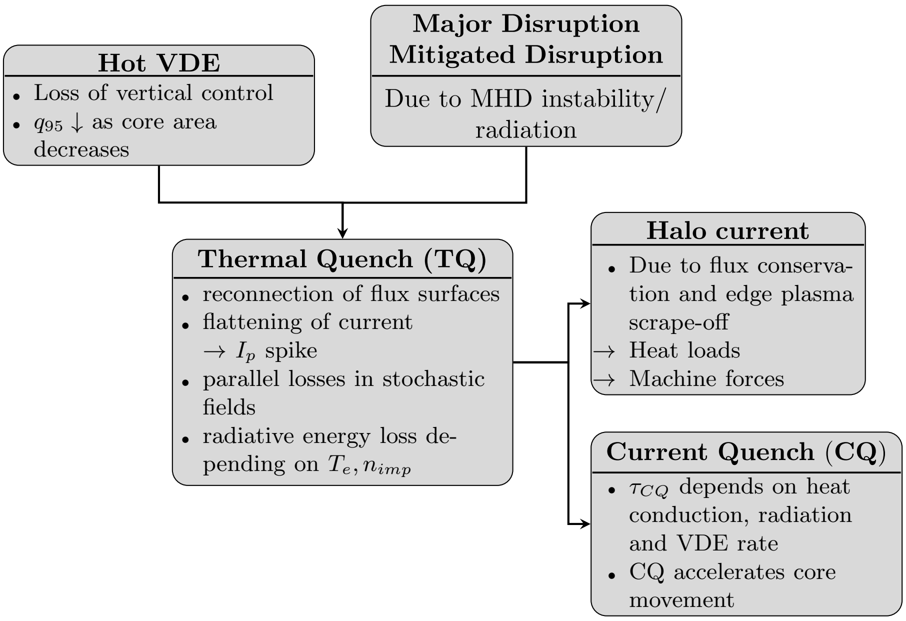

Figure II.1: MHD instabilities (s. section II.1) or impurity accumulations can lead to the termination of a discharge in a major disruption (s. section II.3.1). In some cases, a disruption is intentionally triggered or mitigated by the injection of material (s. section II.3.5) to reduce the loads on the machine. The subsequent thermal quench leads to a fast loss of the thermal energy, resulting in large heat loads on the PFCs. Afterwards, I_p decays during the current quench phase on a time scale depending on the post-TQ temperature. The TQ can also be a result of the vertical motion in a VDE (see section II.3.2). A as a result of the vertical motion and current diffusion, halo currents flow in the SOL and wall (see section II.3.3). A consequence of disruptions are EM forces on the structures (see section II.3.4).

TQ dynamics One of the most common triggers of the TQ is the growth of a tearing mode associated to a rational flux surface. But also other violations of the MHD stability limits or sudden cooling by impurities lead to the growth of large scale modes. The dynamics of the TQ can vary depending on the cause of the disruption, but we describe an often observed scenario in the following.

During the initial phase of the TQ, the core profiles first flatten due to core mixing often induced by a coupling between a 2/1 and an internal 1/1 or 3/2 mode [Bon86, Sch95]. This only leads to a small decrease of the thermal energy content. The non-linear destabilization of further modes leads to an overlap of various magnetic islands, resulting eventually in a reconnection event [Boo19a] throughout the plasma. As a large fraction of the flux surfaces become stochastic, fast parallel conduction leads to a loss of thermal energy to the surrounding PFCs [Hen07, Ned08].

The TQ is accompanied by a characteristic spike in the plasma current (I_p) in the order of 10 % of the initial I_p, as indicated in figure II.2, which is a result of the flattening of the current

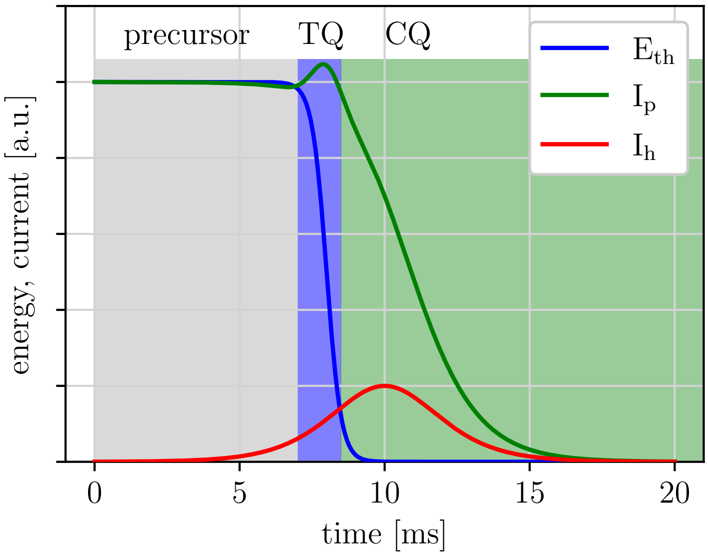

Figure II.2: The evolution of the thermal energy, plasma current and halo current during a typical disruption are shown. The thermal quench occurs on a short time scale of ≈1 ms, the associated reconnection event leads to a spike in the plasma current before it decays on a longer time scale from 1 to hundreds of ms. During the current quench, a fraction of the current flows through the SOL and wall structure, the so called halo current I_h.

profile during the reconnection event. Its origin is the conservation of helicity H during the current re-distribution phase [Bis93], where H is defined as

$$H = \int \mathbf{A} \cdot \mathbf{B} \, \mathrm{d}V, \tag{II.12}$$

with the vector potential **A**. The current flattening itself is too fast for simple current diffusion. Instead, it can be explained by mixing of the plasma by MHD activity [Nar23] similar to sawtooth instabilities and by plasma waves [Boo20, Nar23]. Current flattening beyond the LCFS has also been observed in [Art21a], as a sign of global redistribution of the current.

In the experiment, the TQ duration can be measured directly by the temperature, the heat deposition on the PFCs or X-ray emissions as done in various machines [Pau03, Xia23, Ric05]. The measured TQ duration varies from hundreds of µs to ms [Hen07] scaling with the plasma radius a [ITE99, Ned08], where the TQ time is usually taken as the time between the drop of 90 % to 20 % of E_{th} or the core temperature:

$$\tau_{TQ,90} = \frac{t_{20} - t_{90}}{0.7} \tag{II.13}$$

The TQ dynamics were studied [Zha23] with a kinetic code under the assumption of fully stochastic field lines and under the absence of perpendicular transport, indicating that τ_{TQ} is dominated by convective transport rather than parallel heat conduction. Under these considerations, the flux-limited heat conduction is constrained by ambipolarity, so that the ion sound speed determines the energy loss throughout the majority of the TQ [Li23]. This shows that

MHD might not be sufficient to capture the full dynamics of the TQ and kinetic simulations might give useful input to set the transport coefficients in MHD.

In conclusion, the two determining factors of the TQ duration is the opening of the flux surfaces dictated by MHD mode growth and reconnection [Wad79], and second, the rate of heat loss in stochastic field lines. In MHD simulations, the parallel transport becomes ineffective below 100 eV when the Spitzer-Haerm parallel conductivity [Spi53] is used, so that the final temperature stays in this range unless impurities are taken into account [ITE99]. Inside the core, the post-TQ temperature is determined by a balance of transport, Ohmic heating and radiation. The effective heat transport in the core depends on the reformation of closed field lines and secondary reconnection events. Whereas in the SOL, the parallel heat flux on the PFCs can also be an important loss channel for thermal energy [Kir16]. The impurities responsible for radiation either originate from the background present during normal operation or stem from interaction with the wall.

Due to various processes taking part on their respective time scales, the TQ can consist of several phases with different E_{th} loss rates [Hen07] and (II.13) is only one way to define its duration. E.g. during the core mixing, the loss rate is relatively slow, while it speeds up significantly after the complete plasma volume becomes stochastic.

Analysis of AUG data showed a temperature loss on a time scale of hundreds of µs, while the power deposition on the PFC components occurs on a longer time scale of ms [Pau03, Pau04]. The core loss is governed by the MHD activity and heat conduction time scales, whereas the energy deposition is strongly influenced by the sheath physics [Hen07], rendering this problem strongly non-linear. Hence, simple scaling laws might not apply for the prediction of time scales in future, larger machines and numerical models can help to resolve this issue by dedicated simulations. The TQ itself remains a complicated process with dynamics that are not fully understood, which can vary greatly depending on the equilibrium profiles and the cause of the disruption [Sch95].

For future machine design, it is essential to accurately predict the peak heat flux, the toroidal asymmetries and the expansion of the heat deposition width, where the latter is estimated to three times its steady state value [ITE99].

CQ dynamics The TQ is followed by a decay of I_p in the subsequent **current quench (CQ)** phase due to the enhanced plasma resistivity η in the cold post-TQ plasma, as $\eta \propto T^{-3/2}$. The CQ duration (τ_{CQ}) is commonly defined as the normalized time between a decrease from 80 to 20 % of the pre-disruption I_p:

$$\tau_{CQ} = \frac{t_{20} - t_{80}}{0.6}. \tag{II.14}$$

τ_{CQ} depends on η and the plasma inductance [Mye17], where the latter depends on the plasma shape and internal inductance l_i, and is typically in the range of several to tens of ms in present machines. The CQ can be accelerated by radiation leading to a low post-TQ temperature or by the vertical movement of the core, opening up flux surfaces [Leh13]. A minimum CQ time normalized by the plasma area of 1.67 ms/m^2 was found empirically and is used as a lower estimate for future tokamaks [Eid15].

The CQ is also responsible for some of the loads that the machine experiences during a disruption as the I_p decay transfers a fraction of the current to the wall, leading to local and global electromagnetic forces. Furthermore, the remaining magnetic energy is transformed into thermal energy by Ohmic heating, leading to heat loads on the PFCs.

Finally, tokamaks with large I_p are susceptible to so-called **runaway electrons (REs)**, which are relativistic electrons that can make up a large fraction ($> 50\,\%$) of the initial plasma current. Due to their high energy, they can lead to surface and deep melting of the PFCs. Especially high current devices face the risk of REs because the I_p decay leads to a high toroidal electric field, which can accelerate [Ros97] the small fraction of fast electrons stemming from various sources [Bre19]. This so-called avalanche effect depends exponentially on I_p with a multiplication factor of $\exp\left(\frac{I_p}{0.02\,\mathrm{MA} \ln\Lambda}\right) \approx \mathrm{e}^{50}$ for ITER-like devices [Ros97]. This signifies that a single electron with sufficient energy is enough to produce a significant runaway current.

In summary, disruptions are characterized by a reconnection phase during the TQ and the I_p decay in the CQ phase, which can be preceded by losses of thermal energy. The typical dynamics of a disruption can be seen in figure II.2 including the TQ, CQ as well as so-called halo currents introduced more in detail in section II.3.3. Disruptions can lead to large heat loads and electromagnetic forces, which pose a risk for future power plant operation because of machine downtime. One type of disruption is known for leading to particularly large heat loads and forces, which is the hot VDE discussed in the following section.

II.3.2 Vertical Displacement Events

Disruptions are closely linked to the vertical instability of the plasma, which has its origin in the plasma shape. Increasing the elongation κ of the plasma cross-section is a common tool to enhance the performance [Fre15] at the cost of vertical instability. The plasma shaping is achieved by a gradient in the external magnetic field, which transforms a stable equilibrium into a marginally stable one with respect to the vertical position.

This can be understood easily when considering three current loops that are stacked on top of each other as a representation of the plasma and PF coil system [Kik12, Sch20]. If the middle loop representing the plasma moves downwards, it is accelerated in the same direction due to the $\mathbf{J} \times \mathbf{B}$ force as the current in all three loops has the same sign. Per symmetry, an upward perturbation leads to an upward acceleration. In general, the vertical force on the plasma by the PF coils has the vertical component F_z, with:

$$F_z \propto I_p \frac{\partial B_{r,\mathrm{vac}}}{\partial z} \mathrm{d}z, \tag{II.15}$$

where $\mathrm{d}z$ is the displacement from the equilibrium and $B_{r,\mathrm{vac}}$ is the radial component of the external magnetic field.

The plasma motion induces eddy currents in the strategically placed conductive structures, e.g. passive coils and conductive walls, that slow down the plasma motion. The resulting stabilizing force has the following dependence:

$$F_{z,\mathrm{stab}} \propto I_p^2 \left(\frac{\mathrm{d}M_{pw}}{\mathrm{d}z}\right)^2 \mathrm{d}z, \tag{II.16}$$

where M_{pw} is the mutual inductance between the plasma and surrounding structures.

The eddy currents decay on the resistive time scale of the passive components $\tau_{L/R}$ ranging from several to hundreds of ms, which allows the use of an active control system to stabilize the position [Amb05]. However, this is only successful above a certain plasma current [Gru93, Boo19b] and up to a maximum elongation κ [Miy11] since the destabilizing force dominates otherwise.

In the case of a control system failure, the plasma will move vertically on the $\tau_{L/R}$ time scale. The vertical growth rate γ_{VDE}, with $\mathrm{d}z \propto \exp(\gamma_{VDE}t)$, depends on the coupling to the conductive structures, $\tau_{L/R}$, the plasma current as well as different shaping factors that influence the magnetic field index n_{fi} [Seh16]. The field index n_{fi} is an indicator for F_z and is related to the external magnetic field by:

$$n_{fi} = -\frac{R}{B_{z,vac}}\frac{\partial B_{z,vac}}{\partial R}. \tag{II.17}$$

The vertical external magnetic field required for equilibrium is described by [Wes11, ch 3.8]:

$$B_{z,vac} = -\frac{\mu_0 I_p}{4\pi R_0}\left(\ln\left(\frac{8R_0}{a}\right) + \Lambda - \frac{1}{2}\right), \tag{II.18}$$

where R_0 is the major radius of the magnetic axis and $\Lambda = \beta_p + \frac{l_i}{2} - 1$ (see section I.3 for their definition). Therefore, also the plasma pressure and the current profile influence the vertical stability of the system. As these quantities vary during the displacement, γ_{VDE} is not constant for sufficiently large displacements, making the vertical displacement non-linear.

During the vertical motion, the plasma comes into contact with the wall and the outer layers are scraped off. This leads to a reduction of the edge safety factor ($q_{95} \propto a^2/I_p$) due to the shrinking of the plasma area at approximately constant I_p [Art20]. Low-n current driven MHD modes are triggered as the safety factor decreases, eventually leading to the onset of the TQ. Also, the gradients of the current, density and temperature steepen at the edge, destabilizing further MHD modes [Bon86, Sch23a]. Observations in EAST showed that the edge temperature decreases first and the thermal energy is lost in stages, linked to the changing q_{95} until the temperature decreases further in a final crash [Xia23]. The fast loss at the end is probably due to a full reconnection, while before only the edge was stochastic. Because the plasma retains its temperature and current during the displacement and prior to the TQ, this event is referred to as a **hot VDE**. The associated electromagnetic forces and heat fluxes are in the most destructive category and should be avoided for safe operation.

Vertical instabilities can also occur as a consequence of rapid profile changes resulting from sawtooth crashes or large edge instabilities (ELMs) that degrade the field index (II.17). Also major disruptions are a prominent example among these events. Additionally to the current profile changes, the plasma shifts inward in R direction into a region of more destabilizing n_{fi} due to the loss of pressure in the TQ. This is due to the fact that the Shafranov shift (see section I.3) decreases as p is lower.

Simultaneously, l_i changes because of the magnetic reconnection event, inducing currents in the surrounding structures. As a consequence, the plasma experiences a dragging effect due to the attraction by the eddy currents in the top-down asymmetric conductive structures, unless it is positioned at the so-called neutral point [Nak96]. This effect leads to a shift towards the X-point for decreasing l_i, which is the case for the current flattening during the TQ.

Additionally, the stabilizing force $F_{z,\mathrm{stab}}$ decreases faster than F_z during the CQ due to its I_p^2 dependence, thus, accelerating the vertical motion [Gru93, Boo19b]. This mechanism leads to an unavoidable motion of the plasma core during disruptions. In particular, the plasma position becomes a function of I_p in the limit of fast current quenches $\tau_{CQ} \ll \tau_{L/R}$ [Kir17]. Therefore, the wall contact always occurs at the same I_p [Boo19b, AS18].

We can distinguish two different kinds of VDEs: In case the vertical motion is faster than the CQ duration ($\tau_{CQ} > \tau_{L/R}$), q_{95} decreases with the displacement, which can lead to plasma asymmetries and larger forces (see section II.3.4 for the forces). This is the case for hot VDEs for example. In contrast, q_{95} typically stays larger and less plasma asymmetries are observed if $\tau_{CQ} < \tau_{L/R}$. The latter scenario is sometimes referred to as **cold VDE** or radiation dominated VDE because it requires a cold plasma, which can only be achieved in the presence of impurities [Art23]. Otherwise, the plasma can reheat, leading to longer CQ times.

Furthermore, this picture changes when currents in the SOL are considered, as will be pointed out in section II.3.5. These so called **halo currents** (s. section II.3.3) close poloidally through the wall structure [Hum99] and typically reach their peak magnitude during the CQ as shown in figure II.2. Before describing the special role of halo currents in mitigated disruptions in section II.3.4, we will go more in detail in the halo current physics in the following section.

II.3.3 Halo currents

The **halo currents** observed during disruptions reside in the SOL (also called halo region in this context) and close through the wall structures as indicated in figure II.3. Due to the low pressure in the SOL, the currents follow the magnetic field lines to preserve the pressure balance $\mathbf{J} \times \mathbf{B} = \boldsymbol{\nabla} p \approx 0$, while the wall can resist a force. Therefore, the currents take the path of the lowest resistance, in most cases poloidally through the conductive structure. The halo current I_h is usually defined as the **poloidal component that enters the wall** as:

$$I_h = \frac{1}{2} \int \int |\mathbf{J} \cdot \mathbf{n}| r R \,\mathrm{d}\theta \,\mathrm{d}\phi, \tag{II.19}$$

where $\mathbf{n}$ is the normal unit vector to the wall and $r\mathrm{d}\theta$ is the poloidal length of the wall segment. Unless further specified, we use this definition in accordance to the experiments, where I_h can be measured more easily than the toroidal component in the SOL as it enters into the wall. The poloidal and toroidal halo current component in the SOL ($J_{h,\theta}, J_{h,\phi}$) are related by the local safety factor in the halo region q_h with $J_{h,\phi} = q_h J_{h,\theta}$ [Hum99]. The **halo fraction (HF)** is the ratio of the maximum I_h and the pre-TQ plasma current. The HF of hot VDEs are usually the largest, where ASDEX Upgrade observed HFs of up to 30 %, which is on the higher range of experimental measurements [Eid15].

The vertical force on the structures by halo currents can be estimated as $F_h = I_h B_\phi \Delta R$ [Pau11], where I_h is the poloidal halo current that enters into the structures and ΔR is the mean length of the current path through the wall. Due to Ohmic heating, halo currents are responsible for part of the heat fluxes during the CQ phase.

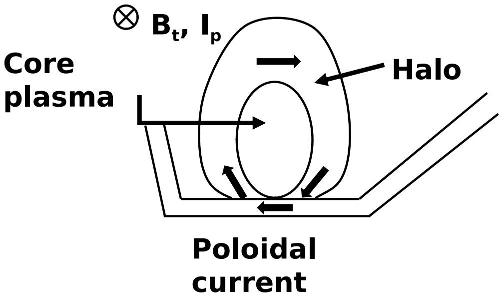

Figure II.3: The halo current follows magnetic field lines in the SOL due to force balance and closes poloidally through the surrounding structures. (Own figure based on [Hum99])

The halo currents occur due to the a) induction of current in the SOL for poloidal and toroidal flux conservation due to the decaying plasma core current, b) the current in the SOL through the opening of the closed flux surfaces during a VDE and c) the induction of halo currents by the motion of the plasma [Hum99]. Furthermore, reconnection events during the TQ and MHD crashes during the CQ phase lead to a flattening of the current profile beyond the LCFS, and thus, add to the halo current [Art22, Sch23a].

While the magnitude of I_h scales with I_p^2/B_t [Gra96], an explanation for the width of the halo region is not straightforward. The crucial factors are the SOL density and temperature, which are not easy to determine during a disruption. They in turn set the ion saturation current (II.10) that proved to limit the halo width in COMPASS discharges [Ada22]. Another factor is the current diffusion in the halo region. A low temperature decreases the current diffusion time to below the CQ time, which allows a broadening of the halo region [Eid11]. Whereas at larger temperatures, the halo resistivity η_h leads to diffusion times longer than the CQ time, and therefore, to a more narrow halo region. A characterization of the halo width has been performed in various machines [Cob21, Pau11, Eid11, Tin18]. In AUG, the mean lenght of the current path ΔR lies around 40 cm [Pau11].

During phases of MHD activity, the plasma, and thus, the halo current can be non-axisymmetric and potentially rotating, which causes horizontal forces on the machine. The asymmetry is quantified by the **toroidal peaking factor (TPF)** defined as [Eid15]:

$$TPF = \left.\frac{\max(I_h(\phi))}{I_h}\right|_{I_h=I_{h,max}}, \tag{II.20}$$

indicating the ratio of the maximum halo current at one toroidal position and the average I_h at the time of maximum I_h. The rotation is connected to the MHD dynamics [Str14, Boo12] and scaling laws have been deduced from present devices [Mye17] and refined in [Sap22, Sap23]. The expected rotation frequency in AUG would be in the order of a hundreds of Hz, which is in the previously observed range of 500 to 1000 Hz [Sap22]. It is a concern for ITER, in particular, if the rotation is in resonance with the machine components [Mye17]. In the following, the forces during disruptions are explained in more detail.

II.3.4 Disruption forces

The plasma motion, current profile changes and I_p decay lead to the induction of eddy currents in the surrounding conductive structures (here called wall for simplification). In the case of halo currents, the SOL currents close directly through the wall structure. Apart from the occurrence of local $\mathbf{J} \times \mathbf{B}$-forces, the interaction with the external magnetic field can lead to global EM-forces on the structures, so that sufficient support structures are required to withstand them. As the plasma column itself is globally force-free due to its low mass (large forces would lead to a high acceleration, generating large electric fields), the total force from the interaction with halo currents, eddy currents in the wall and the external magnetic field must be compensate each other.

The largest force that typically occurs is the global vertical force due to the vertical motion during a (hot) VDE. According to Newton's third law, this force must be opposite to the force by the PF coils on a displaced plasma (II.15) and therefore scales with $I_p I_{p,0} \Delta Z_{curr}$, resulting in a magnitude in the order of 100s of kN [Str91, Pau07] to MN [Ric04] in present devices. For future tokamaks that will operate at larger I_p, the forces will scale accordingly if not mitigated. The dependence on the pre-TQ current $I_{p,0}$ enters into the relation because the current in the PF coils, producing the quadrupole field, scales with I_p. Typically, the control system cannot react on the time scales of a fast disruption, so that the PF coil currents cannot be decreased.

Other contributions to the vertical force originate from the toroidal current in the vessel induced by the current decay or I_p spike, due to top/down asymmetries in the vessel and the magnetic field. The total force on the passive structures F_w can be expressed as shown in [Wes11, ch. 7.12] and [Miy11]:

$$F_w = F_{p,c} + F_{w,c}, \tag{II.21}$$

where $F_{p,c}$ is the force between the PF coils and $F_{w,c}$ is the force between the passive structures and the PF coils. $F_{p,c}$ can be expressed as (II.15) for forces due to the plasma motion in a hot VDE. The second term describes the shielding of the plasma by the induced eddy currents. In case of an ideal wall, the F_w is suppressed completely since the shielding would be perfect [Pus17].

The shielding term can be described by a damping term on the force $F_{p,c}$ and expressed as [Miy11]:

$$F_{w,c}(t) = \frac{1}{\tau_{L/R}} \int_{-\infty}^{t} F_{p,c}(t' - \tau_d) \exp\left(-\frac{t-t'}{\tau_{L/R}}\right) \mathrm{d}t', \tag{II.22}$$

where $\tau_{L/R}$ is the characteristic decay time of the wall currents and τ_d is a delay term to take into account the multiple decay times of different wall current eigenmodes. This shielding is effective when $\tau_{L/R}$ is smaller or comparable to the duration of the force ($\approx$ time of the disruption) as shown in the example of figure II.4. Then, the peak of the force is both reduced in its magnitude and delayed with respect to the source term.

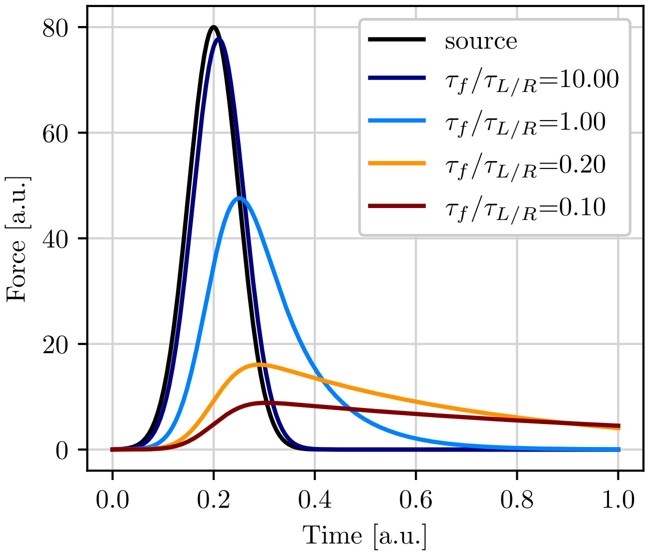

Figure II.4: The plot shows an example of the shielding of a Gaussian shaped force, applied on a time scale of $\tau_f = 0.05$ and the resistive wall time scale $\tau_{L/R}$ was varied in a range from $\tau_{L/R} < \tau_\mathrm{f}$ to $\tau_{L/R} > \tau_\mathrm{f}$. When the decay time of the wall terms is comparable or smaller to the time the force is applied, it can be shielded effectively.

Moreover, substantial horizontal forces can arise due to toroidal asymmetries in the conductive structures [Yan22] or plasma asymmetries. The JET tokamak observed horizontal forces in the order of MN [Ric00b] associated with a 1/1 kink mode, which corresponds to a tilting of the plasma around a horizontal axis. Simultaneously, the plasma current varies toroidally with a $n = 1$ pattern. Similar current asymmetries have been observed in COMPASS [Ger15], while in AUG no substantial horizontal force is observed [Pau11]. This points to an absence of a large 1/1 kink mode or I_p asymmetries, while the I_p asymmetry usually cannot be measured directly during disruptions.

The magnitude of the measured force in JET agrees with the force on a tilted toroidal wire known as the Noll formula $F_h = B_\phi I_p \Delta Z$ [Nol97]. However, the force on the plasma is non-zero in this model, which points to its incompleteness since a net force on the plasma would lead to displacements at Alfvén speed ($\approx$ µs). When taking into account force balance, the force on the wall resulting from tilting a wire is more than a magnitude smaller than Noll's formula [Pus22]. Both of these models do not consider currents shared between the plasma domain and the conductive structures. In addition, the toroidal asymmetry of the poloidal halo current is not sufficient to explain the forces observed in JET [Ric00a].

Instead, asymmetric toroidal currents in the wall seem to play a significant role. In one proposed theory for the horizontal force known as the source/sink model [Ric00a], the plasma current partly flows through the vacuum vessel as halo currents. Due to the non-homogenous resistivity of the JET vacuum vessel, the halo current pattern in the vacuum vessel has a poloidal contribution interacting with the B_ϕ. EM-calculations of the vacuum vessel with a halo current originating from a source comparable to a kinked plasma lead to forces in the same order as the measured ones [Ric00a].

Whereas in the so-called ATEC model [Roc16] illustrated in figure II.5 b), the toroidal I_p asymmetries result from eddy currents in the vessel that flow between plates wetted by the plasma (blue path). This model also requires a large 1/1 kink mode, which corresponds to a tilting of the plasma column around a horizontal axis. Due to the tilting, only paths between plates in close contact with the plasma become conducting, so that the eddy currents can only flow through the plasma in this region. Furthermore, the vacuum vessel an-isotropies play an important role by making the path through the wetted area more desirable due to its lower resistance. The poloidal current path interacting with the B_ϕ is responsible for the horizontal foce.

Both JET and ASDEX Upgrade have a non-homogeneous vessel resistivity due to bellows between sectors that locally enhance the wall resistance. This favors the current paths through the plasma in the ATEC model and the poloidal current path in the vacuum vessel in the source/sink model. Recent investigations in COMPASS could not resolve the concurring theories [Mat22].

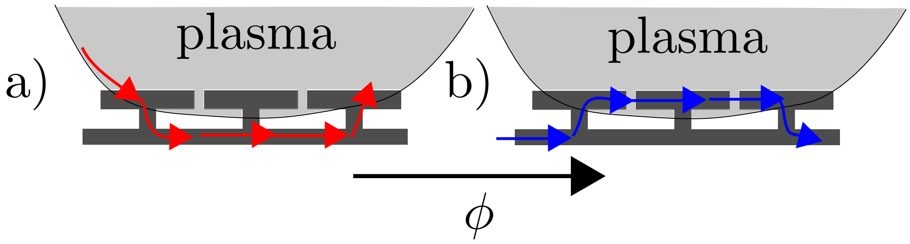

Figure II.5: In the source/sink model shown in a), the I_p asymmetry is explained by toroidal halo currents (red) that flow through part of the vessel, b) while the ATEC model allows the eddy currents (blue) to take the path over the plates wetted by the plasma. The kink in this figure is exaggerated. (Own figure based on [Roc16])

The vertical force in unmitigated disruptions is estimated as 80 MN [Miy11] for ITER and the horizontal force predictions vary from several MN to multiple times this value [Art22], where the larger estimates lie above the safety limits of the components. Therefore, mitigation techniques are an essential feature in current tokamaks and crucial for the operation of future devices with larger energy. One mitigation technique is discussed in the following.

II.3.5 Disruption mitigation by Shattered Pellet Injection

Future devices have to be protected against the thermal loads appearing during the TQ and CQ phase of a disruption as well as against the electromagnetic forces described in section II.3.4. Otherwise, early material aging or damages on components can occur, causing machine downtime or shortening of its life-time. One method of load mitigation relies on the injection of large amounts of material by massive gas injection (MGI) or shattered pellet injection (SPI). The MGI mitigation is used over a variety of machines including JET [Leh13, Ger20], DIII-D [Hol08], Alcator C-mod [Why07], KSTAR [Yu12] and ASDEX-Upgrade [Pau17]. Here, hydrogen isotopes or impurities are introduced by gas valves outside the plasma.

ITER has decided to rely on the SPI technology, where a cryogenic pellet is shattered into small fragments to achieve better material assimilation and deeper deposition than MGI. To test the efficiency of the system in terms of assimilation, radiation fractions and double injection, the technology has been tested in DIII-D [Com16], HL-2A [Xu20], KSTAR [Par21], JET [Jac21] and J-TEXT [Li21].

To answer research question in sight of the ITER disruption mitigation system (DMS), an SPI system was installed in ASDEX Upgrade with double injection capabilities [Dib23]. Simultaneously, the diagnostic system was upgraded with measurements in additional sectors (s. section II.4) and an extensive laboratory analysis was performed to characterize the velocity and size distribution of the shattered pellets by camera imaging [Peh22]. Based on this, recipes for pellets have been developed that can be linked to a certain shatter distribution, giving insight about the real injection parameters in the experiment. This system was used for mitigated VDE experiments in AUG presented in section III.2 as part of the internal program in the 2021/22 campaign and the work of this thesis.

The strategy for mitigation is the following [Leh15]. To mitigate the heat loads, the majority of the thermal and magnetic energy must be converted to radiation to achieve a more uniform heat deposition instead of the narrow heat fluxes occurring during unmitigated disruptions. This can be achieved by high-Z impurities like Neon or Argon that cause a TQ by triggering MHD instabilities through the cooling of the edge plasma [Hu18] and aim to achieve high high radiation fraction. The radiation fraction f_{rad} during a disruption is defined as the ratio of the radiated energy and the available energy for radiation, which can be defined in different ways. One is the sum of the pre-TQ thermal and magnetic energies E_{th} and E_{mag} minus the energy transferred to the conductive structures by induced currents E_{coupl} [Leh13].

$$f_{\mathrm{rad}} = \frac{E_{\mathrm{rad}}}{E_{th} + E_{mag} - E_{coupl}}. \tag{II.23}$$

The radiation decreases the temperature of the post-TQ plasma, so that the CQ time shortens [Pau07], which is in general desirable for force mitigation.

However, a fast CQ can lead to local EM forces and facilitates the creation of REs in high current devices due to the large toroidal electric field [Ros97]. In order to reduce the risk of REs, the density is increased as much as possible to increase collisional drag by injecting a hydrogen or deuterium shattered pellet prior the impurity SPI that triggers the TQ. In case a large RE beam occurs, another low-Z pellet can be injected to expel the impurities and trigger MHD instabilities to deconfine the fast electrons in a benign way [Reu21]. Another proposition is the installation of a non-axisymmetric passive coil, where current is induced in the CQ phase aiming to stochastisize the plasma by resonant and non-resonant perturbations [Boo11, Smi13].

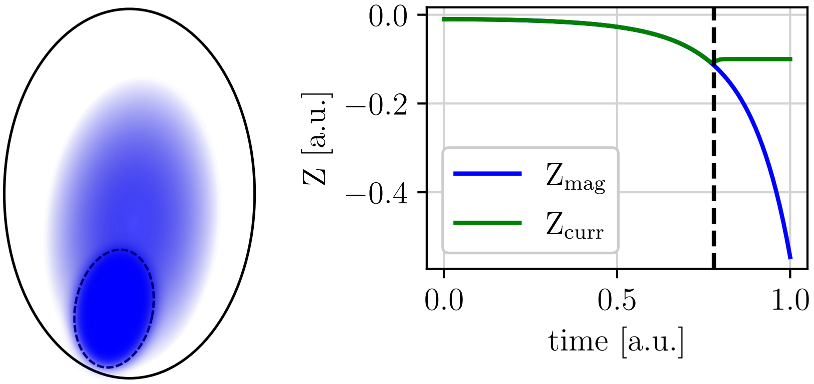

Figure II.6: (Left) An illustration of the toroidal current density in a mitigated disruption. While the plasma core, indicated by the dashed line, continues to move downward, the current density in the halo region keeps the current centroid close to the midplane. (Right) The magnetic axis continues its movement after the TQ (vertical dashed line) occurs. Whereas the current centroid stagnates.

The EM force mitigation also proved to be successful [Hol08, Jac16, Pau17] in current machines, where REs usually are not important. Both the vertical and horizontal forces are reduced significantly after the injection of impurities. However, the mechanism behind the reduction of the former has not been fully resolved yet in the literature and has usually been attributed to the reduction of the poloidal halo currents I_h. We have investigated a theory based on the diffusion of halo currents in cold post-TQ plasmas [Eid11], which is laid out in the following.

The fast current diffusion in the cold, resistive plasma leads to a significant broadening of the halo width to a degree, where a large fraction of the I_p is carried by the toroidal halo currents outside the LCFS. As a consequence, the vertical current centroid, defined as:

$$Z_{\text{curr}} = \frac{\int Z J_\phi \mathrm{d}S}{\int J_\phi \mathrm{d}S} = \frac{\int Z J_\phi \mathrm{d}S}{I_p}, \tag{II.24}$$

with the vertical coordinate Z and the toroidal current density J_ϕ, remains closer to the midplane as indicated in figure II.6. This quantity can be interpreted as the geometric center of the toroidal current distribution of both the closed and open field line region. The phenomenon that the displacement ΔZ_{curr} is smaller after impurity injection was observed in various devices [Pau07, Eid11, Ger21]. Finally, the stagnation of Z_{curr} reduces the vertical force F_z, which is proportional to $I_p \Delta Z_{\text{curr}}$ as can be seen from equation (II.15).

Although this might seem contradictory at first, as it was stated before that halo currents create a vertical force. However, q_{95} tends to increase during the CQ phase with $q_{95} \gg 1$ for $\tau_{CQ} < \tau_{VDE}$, contrary of what happens during a hot VDE. Therefore, the presence of toroidal halo currents does not infer that the poloidal component is large, so that the forces due to I_h remain low. Furthermore, the increase in q_{95} makes the 1/1 kink mode inaccessible, explaining the reduction of the horizontal force [Ger21]

In summary, the reduction of the vertical forces can be attributed to different factors. First, when Z_{curr} does not move significantly during the CQ, the source term of the vertical force $F_z \propto I_p \Delta Z_{\mathrm{curr}}$ is reduced. Second, the poloidal halo currents I_h are typically lower in mitigated disruptions because q_{95} remains large, while this still allows for toroidal halo currents. Third, in case of a fast disruption $\tau_{\mathrm{dis}} < \tau_{L/R}$, the shielding by the eddy currents of the wall can decrease the forces. All of these factors are present in a mitigated disruption, where the latter one only plays a minor role in most of the present devices as $\tau_{L/R}$ is typically smaller or comparable to the disruption time scales.

The theory of the F_z reduction by the current centroid stagnation was laid out in detail in [Sch23b] and the experimental results as well as the corresponding validations with the MHD code JOREK are included in section III.2 and IV.4 respectively.

II.3.6 Summary

This section provided an overview about different aspects of disruptions, while this thesis will focus on hot and mitigated VDEs in particular. In hot VDEs, the loss of thermal energy in the TQ is initiated by a vertical movement and is followed by the CQ. It is characterized by a low q_{95}, which triggers the TQ and is responsible for large poloidal halo currents I_h. The plasma movement leads to large vertical forces and horizontal forces can occur if the plasma current is asymmetric. The CQ duration in a hot VDE is determined by the vertical motion and the boundary heat flux [Leh13].

Above certain plasma energies, mitigation techniques are indispensable to reduce thermal and EM loads on the device. A common method is the injection of shattered pellets (SPI) consisting of plasma fuel or impurities with the aim to dilute the plasma and transfer energy into radiation. A new mechanism for the vertical force reduction was laid out in section II.3.5 that relies on the fact that the geometric center of the toroidal currents inside the PFCs stagnates after the TQ. Impurity mitigated disruptions typically have larger q_{95} and faster CQs, which improves the shielding by eddy currents in the vacuum vessel. In this case, the CQ duration is determined by the post-TQ temperature determined by the radiation balance.

After the overview about different aspects of disruptions, the diagnostics used for analyzing the dedicated experiments in AUG are discussed in the following.

II.4 Disruption diagnostics

In the following, the diagnostics relevant for disruption measurements in ASDEX Upgrade are described briefly. An overview about the diagnostics for disruptions in particular and their location can be found in [Pau11, Pau17, She20].

Halo current diagnostics The occurrence of halo currents, introduced in II.3.3, can contribute to the vertical force on the machine and to heat fluxes to the PFCs by Ohmic heating. Knowing their magnitude, asymmetries and width is essential to determine the loads on the machine. The poloidal halo currents are routinely measured in AUG by shunt measurements to estimate the current via a voltage drop as shown in figure II.7 a). The current follows the red path along a hollow screw which has a bolt on the inside. By measuring the voltage drop between the bolt (at tile potential in yellow) and the end of the bolt (blue), the halo current is calculated. This method assumes that the inductance of the system is not important, which is true for slow variations of the current and a large measurement resistance. The estimate of the bandwidth depends on the dimensions of the shunt measurement and the resistance, with the lowest value being around 1.5 kHz [Tes22].

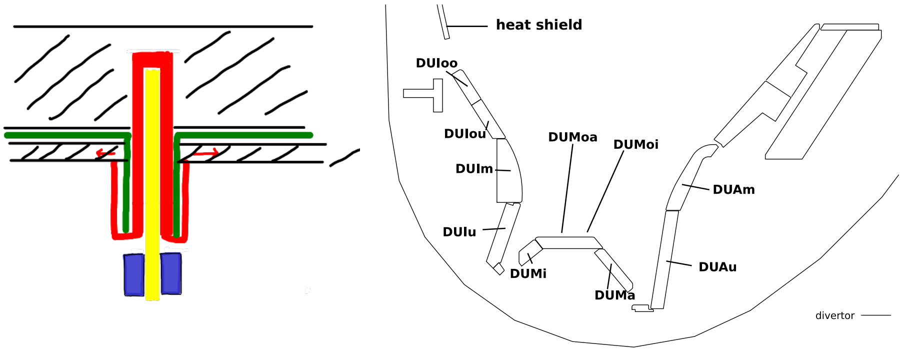

Figure II.7: A sketch of the shunt diagnostic is shown on the left. The halo current flows along the red path, while the voltage drop between the tile (yellow) and the end of the bolt (blue) is measured. (Own illustration inspired by [Tes22]) The figure on the right shows the lower divertor, consisting of the inner divertor (DUI), the baffle (DUM) and the outer divertor (DUA). Each of the parts is covered by multiple tiles in the poloidal direction. The lower part of the heat shield is shown on the left and the tiles covering the PSL on the right.

The shunt measurements are installed in the upper and lower divertor, the heat shield and in tiles covering the PSL. As we are only considering downward VDEs in this thesis, the lower divertor is shown in more detail on the right of figure II.7. In each of the 16 sectors, there are multiple tiles in toroidal direction, which are not all equipped with diagnostics. Figure II.8 provides an overview of the diagnostic coverage in the sectors. There are 4 sectors with complete poloidal coverage with measurements, while the tiles DUIm and DUAm provide measurements in almost all sectors. In sector 4, two of the tiles in each part of the divertor are used for measuring to estimate short scale asymmetries. In case of broken measurements marked in red in figure II.8), the closest tile in toroidal direction was used to compensate in this thesis.

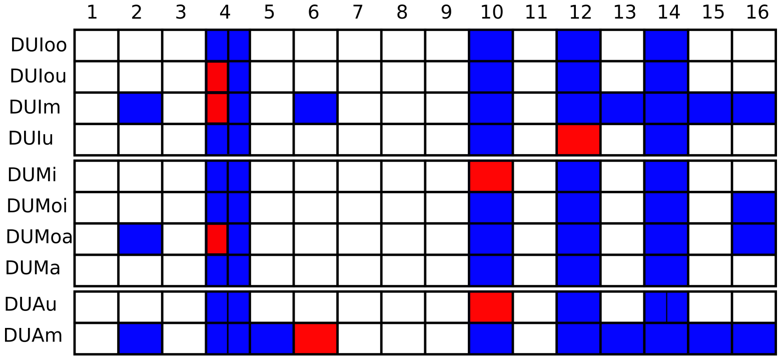

	1	2	3	4	5	6	7	8	9	10	11	12	13	14	15	16
DUIoo				🟦🟦						🟦		🟦		🟦		
DUIou				🟥🟦						🟦		🟦		🟦		
DUIm		🟦		🟥🟦		🟦				🟦		🟦	🟦	🟦	🟦	🟦
DUIu				🟦🟦						🟦		🟥		🟦		
DUMi				🟦🟦						🟥		🟦		🟦		
DUMoi				🟦🟦						🟦		🟦		🟦		🟦
DUMoa		🟦		🟥🟦						🟦		🟦		🟦		🟦
DUMa				🟦🟦						🟦		🟦		🟦		
DUAu				🟦🟦						🟥		🟦		🟦🟦		
DUAm		🟦		🟦🟦	🟦	🟥				🟦		🟦	🟦	🟦	🟦	🟦

Figure II.8: In each sector there are multiple tiles, where only one is equipped with measurements. Sector 4 is an exception with two tiles being equipped with sensors. Four sectors have complete poloidal coverage with measurements. The tiles which where excluded from the measurements are shown in red.

The figures of merit are calculated with the lower divertor measurements with full poloidal coverage (4, 10, 12, 14) unless stated otherwise. The poloidal halo current I_h is determined by summing the current of the inner tiles (DUoo-DUMoi) and the outer ones (DUMoa-DUAm) separately before taking the average of the absolute values. Similar as defined in [Pau11], I_h is calculated in the following way

$$I_h = \frac{1}{4}\sum_{i=1}^{4}\left[\frac{1}{2}\left|\sum_{j=\mathrm{DUIoo}}^{\mathrm{DUMoi}} I_{i,j}N_j\right| + \frac{1}{2}\left|\sum_{i=\mathrm{DUIoo}}^{\mathrm{DUMoa}} I_{h,i}N_j\right|\right], \tag{II.25}$$

where $I_{i,j}$ is the current in tile j located in sector i and N_j is the number of tiles j in toroidal direction. The technical data for the tile dimensions and their number can be found in the appendix B. This assumes that the contact point with the plasma lies between the tiles DUMoi and DUMoa, which is approximately where it is located according to the measurements. Accordingly, the halo fraction (HF) is taken as the ratio of the maximum of I_h and the initial plasma current $I_{p,0}$:

$$\mathrm{HF} = \frac{I_{h,max}}{I_{p,0}}. \tag{II.26}$$

The toroidal peaking factor (TPF) is defined by:

$$\mathrm{TPF} = \left.\frac{I_{h,s}}{I_h}\right|_{t=t_{\max}}, \tag{II.27}$$

and represents the ratio between the halo current $I_{h,s}$ in the sector with the largest magnitude and I_h at the time $t_{\max}$ when I_h is at its maximum. The halo current density is calculated taking into account the area of the tiles determined from CAD drawing.

Apart from the shunt measurements, **Langmuir probes** that are grounded to the vessel potential can be used to measure halo currents [Bri20]. However, most of the probes installed in ASDEX Upgrade are mounted flush to the tiles, which lead to noisy measurements during the disruption due to their small area. Also, the interpretation is more difficult as the poloidal halo current depends strongly on the angle to the magnetic field. Measurements with probes that measure the parallel component of $\mathbf{J}_h$ by protruding into the plasma were performed in COMPASS [Ada22] with the downside of fast degradation of the probes due to large heat fluxes.

Magnetic measurements An essential diagnostic for the plasma state are magnetic measurements allowing for an equilibrium reconstruction and identification of the plasma position, current and shape. The set of diagnostics usually employed for the reconstruction are shown in figure II.9 in blue. Determining the evolution of the current, vessel currents, the PSL current (in AUG) and their asymmetries is crucial to characterize the disruption evolution. While it is possible to measure the plasma current at one toroidal position, the other poloidal magnetic field probes usually saturate during a disruption, rendering them unusable. Moreover, measurements of the vessel currents by jumps in the magnetic field were not possible for the same reason. To overcome this problem, voltage dividers were installed in one additional toroidal plane to allow the measurement of asymmetries. For future disruption studies, the reliability of the magnetic measurements during disruptions has to be improved by updating the diagnostic system.

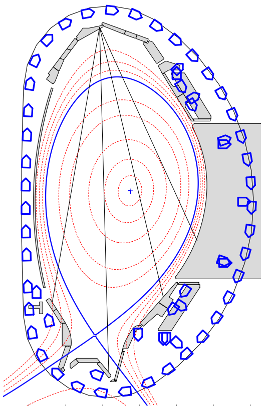

Figure II.9: The cross-section shows the passive components and PFCs in grey, where an equilibrium (#39655) is indicated for reference. The magnetic measurements (blue) provide information about the equilibrium evolution of the plasma. There are different types of bolometers with varying lines of sight. The ones used for estimation of the radiated energy are indicated in the figure. (own figure)

Force diagnostics The global forces on the machine are challenging to estimate as it requires knowledge of the mechcanical model of the machine including the damping and vessel oscillations as done for example in [Ric00b]. An estimate can be given from two systems in AUG.

The first are the measurements of the displacement of the vacuum vessel wit respect to support structures (German *Weggeber)* for the horizontal and vertical direction. However, they are influenced by complex oscillations of the vacuum vessel. The second method allows an estimate of the vertical force by measuring the elongation of the eight suspension rods at the top of the machine holding the vacuum vessel including the PSL. The force is estimated by the following formula (Hooke's law):

$$F = \varepsilon E_m A_r \tag{II.28}$$

with ε [$\mu\mathrm{m\,m^{-1}}$] being the elongation, $E_m = 200\,\mathrm{GPa}$ the elasticity module and A_r the cross-section area of $552\,\mathrm{mm}^2$ per rod.

Radiation The radiation measurements can be done by foil or diode bolometers [Ber14, She20], where the former is used for an estimate of the radiated energy at lower time resolution. Whereas, the latter can be run at a large frequency, but does not allow for a quantitative analysis of the power. Along the installation of the SPI system in AUG, the bolometry system was updated with measurements in more toroidal sectors to detect radiation asymmetries. As a consequence some of the discharges presented in the following will show the results of three sectors, and three of the shots were carried out after the update with measurements in the sectors $\{1, 5, 9, 15, 16\}$. The diagnostic cords used for the analysis are shown in figure II.9.

Density measurement The electron density n_e first gives essential information of the background plasma, its evolution and in the case of mitigation an estimate of the assimilated quantities. In this thesis, we used the data from CO2-interferometry that provides a line integrated value of n_e by estimating the phase shift of a laser beam injected into the plasma. These come with the danger of fringe jumps in case of large gradients occurring during massive material injection making the measurements unusable. The lines of sight are vertical at two different major radii, so that measurements are available for two different positions [Pau17].

II.5 Modeling

The MHD equations presented in section II.1 are used for determining the MHD stability of a plasma state or the evolution of the plasma. In particular, the model allows to simulate large scale dynamics that arise due to MHD instabilities such as ELMs, sawteeth, fishbones or disruptions. The non-linear, extended MHD code JOREK used for this thesis is presented in section II.5.1. It is coupled to the EM wall code STARWALL to include resistive wall effects as described in section II.5.2

II.5.1 The nonlinear, extended MHD code JOREK

The first version of the JOREK code has been developed by Guido Huijsmans since 2002 at CEA with the goal to investigate various instabilities like kink modes and ELMs in X-point geometry [Huy05]. Since its beginnings, the model has been continuously developed and can now modularly include a two temperature model, neutrals and impurities in both a kinetic or fluid implementation, an RE fluid model as well as free boundary simulations. Furthermore, JOREK has been extended for stellarator geometries taking into account the varying shape of flux surfaces with the toroidal angle. A reduced MHD model is used in most cases, allowing for an elimination of fast magnetosonic waves, while a full-MHD model is also available [Pam20]. Based on this principle, problems can be solved in various levels of complexity by switching on different physical effects. An overview about the physics models and their application is given in [Hoe21, Hoe23].

The reduced MHD model The simulation results included in this thesis were obtained with the reduced MHD model of the equations, extended by a simple impurity fluid model in some cases that assumes coronal equilibrium. The reduced version of the equations for the tokamak is based on the assumption that the toroidal magnetic field is dominant and approximately constant in time, so that the total magnetic field can be expressed as:

$$\mathbf{B} = \boldsymbol{\nabla}\psi \times \boldsymbol{\nabla}\phi + F_0 \boldsymbol{\nabla}\phi, \tag{II.29}$$

where ψ is the poloidal flux and $F_0 = RB_\phi$ is constant in space. Furthermore, the following Ansatz is used for the velocity, eliminating fast magnetosonic waves:

$$\mathbf{v} = v_\parallel \mathbf{B} \underbrace{-R^2 \boldsymbol{\nabla} u \times \boldsymbol{\nabla}\phi}_{\mathbf{v}_e} - \frac{\delta^* R^2}{\rho} \boldsymbol{\nabla} p_i \times \boldsymbol{\nabla}\phi, \tag{II.30}$$

where the first term is the velocity in direction of $\mathbf{B}$ normalized by the magnetic field strength, which can be omitted in appropriate scenarios to additionally suppress slow magnetosonic waves. The second term describes the $\mathbf{E} \times \mathbf{B}$ drift in the plasma, where the potential $u = \Phi / F_0$ is used as a stream function for the poloidal velocity. The last term is optional and describes the diamagnetic drift with δ^* defined as $m_{ion}/eF_0\sqrt{\mu_0\rho_0}$ (where ρ_0 is the initial mass density at the magnetic axis).

This kind of Ansatz based reduction of the MHD equations retains the important physics for the price of more complex equations [Hoe21], while it offers a wider range of validity and better conservation properties than ordering based reduced models. Using the reduced model allows for faster computation due to the smaller number of variables and the elimination of fast waves facilitates the use of larger time steps.

In a broad range of applications, this model gives comparable results to the full MHD version with the exception of internal kink modes at finite pressure [Pam20]. The MHD equations in JOREK are based on the visco-resistive MHD equations (II.2), where additional effects coming from trapped particles, kinetics, etc. can be included. Therefore, we call the complete set of equations the extendend MHD equations. In the following, the reduced MHD equations in JOREK are shown with only the diamagnetic drift as an additional effect. More information on the extended models and their application can be found in [Hoe21] and its references.

Physical model In order to obtain the reduced MHD equations, the Ansatz for the velocity and the magnetic field is inserted into the MHD equations (II.2). The evolution of ψ is obtained by projecting the induction equation (II.2d) on $\mathbf{B}$:

$$\frac{1}{R^2}\frac{\partial \psi}{\partial t} = -\frac{1}{R}\left[u, \psi\right] - \frac{F_0}{R^2}\frac{\partial u}{\partial \phi} + \frac{\eta}{R^2}\left(j - j^*\right) + \frac{\delta^*}{2\rho}\boldsymbol{\nabla} p \cdot \mathbf{B} \tag{II.31}$$

where the poloidal component of $\mathbf{J}$ was neglected and the toroidal current density is expressed as $j = -RJ_\phi$. An optional current source term j^* is used to keep the toroidal current density approximately constant. The resistivity is usually chosen to be the Spitzer value [Spi53] following a $T^{-1.5}$ dependence with an optional lower cutoff for numerical reasons. The expression in the first term of the RHS is a Poisson bracket defined as $[a, b] = \partial_R a \partial_Z b - \partial_Z a \partial_R b = \boldsymbol{\nabla} a \times \boldsymbol{\nabla} b \cdot \mathbf{e}_\phi$.

The continuity equation (II.2a) becomes

$$\begin{aligned}\frac{\partial \rho}{\partial t} =& R\left[\rho, u\right] + 2\rho\partial_Z u + 2\delta^*\partial_Z p - \frac{F_0}{R^2}\partial_\phi(\rho v_\parallel) - \frac{1}{R}\left[v_\parallel \rho, \psi\right] \\ &+ \boldsymbol{\nabla}\cdot\left(D_\parallel \boldsymbol{\nabla}_\parallel \rho + D_\perp \boldsymbol{\nabla}_\perp \rho\right) + S_\rho,\end{aligned} \tag{II.32}$$

where the density diffusion is split into the direction parallel ($\boldsymbol{\nabla}_\parallel = \frac{\mathbf{B}}{B^2}\mathbf{B}\cdot\boldsymbol{\nabla}$) and perpendicular ($\boldsymbol{\nabla}_\perp = \boldsymbol{\nabla} - \boldsymbol{\nabla}_\parallel$) to the magnetic field. Note that $D_\parallel$ is only used when $v_\parallel$ is not included in the simulation to eliminate unphysical density gradients along magnetic field lines.

The momentum equation (II.2b) is first simplified by taking into account the gyroviscous cancellation term $\underline{\mathbf{P}}_{gv}$, which is part of the viscous stress tensor. The resulting equation is:

$$\rho\frac{\partial \mathbf{v}}{\partial t} = -\rho\mathbf{v}\cdot\boldsymbol{\nabla}\mathbf{v} - \rho\mathbf{v}_i^*\cdot\boldsymbol{\nabla}\mathbf{v}_e - \boldsymbol{\nabla} p + \mathbf{J}\times\mathbf{B} + \boldsymbol{\nabla}\cdot\left(\underline{\mathbf{P}}_f + \underline{\mathbf{P}}_{neo}\right) + \mathbf{S}_V. \tag{II.33}$$

with $\mathbf{v} = \mathbf{v}_e + v_\parallel\mathbf{B}$. To obtain the evolution equation for $v_\parallel$ and u, a multiplication with $\mathbf{B}$ and the operator $\boldsymbol{\nabla}\phi\cdot\boldsymbol{\nabla}\times[R^2$ are applied respectively. The remaining parts of the viscuous stress tensor come from the fluid $\underline{\mathbf{P}}_f$ stress and neo-classical $\underline{\mathbf{P}}_{neo}$ effects (by the interaction of trapped and passing particles). Details on the form of the stress tensor can be found in the references [Hoe21, Sch09]. The resulting equations for $v_\parallel$ is:

$$\begin{aligned}\rho B^2 \frac{\partial v_\parallel}{\partial t} + \frac{1}{R^2}\rho v_\parallel \boldsymbol{\nabla}_\mathrm{pol}\psi \cdot \boldsymbol{\nabla}_\mathrm{pol}\left(\frac{\partial \psi}{\partial t}\right) &= \frac{\rho}{2R}\left[\psi, v_\parallel^2 B^2\right] + \frac{1}{R}\left[\psi, p\right] \\ &\quad - \frac{\rho F_0}{2R^2}\frac{\partial (v_\parallel B)^2}{\partial \phi} - \frac{F_0}{R^2}\frac{\partial p}{\partial \phi} + \mu_\parallel B^2 \Delta v_\parallel,\end{aligned} \tag{II.34}$$

where $\boldsymbol{\nabla}_\mathrm{pol}$ is the gradient in the R-Z plane ($\mathbf{e}_R\partial_R + \mathbf{e}_Z\partial_Z$). The equation for u has the following form:

$$\begin{aligned}R\boldsymbol{\nabla}\cdot\left(R^2\rho\frac{\partial \boldsymbol{\nabla}_\mathrm{pol} u}{\partial t}\right) &= \left[\rho R^4 \omega, u\right] - \frac{1}{2}\left[R^2\rho, R^2\left|\boldsymbol{\nabla}_\mathrm{pol} u\right|^2\right] \\ &\quad - \left[R^2, \rho T\right] + \left[\psi, j\right] - \frac{F_0}{R}\frac{\partial j}{\partial \phi} + \mu R^2 \Delta\omega\end{aligned} \tag{II.35}$$

In both equations, the stress tensor is reduced to the simplified form of a the spatially constant dynamic viscosity μ, for which a different value in the direction parallel to $\mathbf{B}$ can be chosen as $\mu_\parallel$.

Lastly, the pressure equation has the following form:

$$\frac{\partial p}{\partial t} = -\mathbf{v}\cdot\boldsymbol{\nabla}p - \gamma p \boldsymbol{\nabla}\cdot\mathbf{v} + (\gamma - 1)\boldsymbol{\nabla}\cdot(\underline{\kappa}\boldsymbol{\nabla}T) + (\gamma-1)\underline{\mathbf{P}} : \boldsymbol{\nabla}\mathbf{v} + \eta|J|^2 + S_H \tag{II.36}$$

$$\begin{aligned}\Rightarrow \frac{\partial p}{\partial t} &= -v_\parallel \frac{F_0}{R^2}\partial_\phi p + \frac{v_\parallel}{R}\left[\psi, p\right] - R\left[u, p\right] \\ &\quad - \gamma p\left(\frac{F_0}{R^2}\partial_\phi v_\parallel + \frac{1}{R}\left[v_\parallel, \psi\right] - \frac{2\delta^*}{\rho}\partial_Z p + \frac{\delta^* R}{\rho^2}\left[u, \rho\right] - 2\partial_Z u\right) \\ &\quad + (\gamma-1)\frac{\eta}{R^2}j^2 + (\gamma-1)\boldsymbol{\nabla}\cdot\left(\kappa_\parallel\boldsymbol{\nabla}_\parallel T + \kappa_\perp\boldsymbol{\nabla}_\perp T\right) \\ &\quad + (\gamma-1)\underline{\mathbf{P}} : \boldsymbol{\nabla}\left(v_\parallel\mathbf{B} + \mathbf{v}_e\right) + S_H,\end{aligned} \tag{II.37}$$

Again, the conduction coefficient is split into a parallel and perpendicular part due to the anisotropic transport properties, where $\kappa_\parallel$ is typically several orders of magnitude larger than $\kappa_\perp$ due to the high mobility of electrons along magnetic field lines. The parallel transport is usually chosen to be the Spitzer-Haerm value [Spi53], following a $T^{2.5}$ dependence with an optional upper cutoff for numerical reasons and to take into account the flux limit [Hö10] in a simplified way.

To avoid higher order derivatives in the equations, the toroidal current density j and the poloidal vorticity ω are introduced with the respective definitions of:

$$j = \Delta^*\psi \equiv R^2\boldsymbol{\nabla}\cdot\left(\frac{1}{R^2}\boldsymbol{\nabla}_\mathrm{pol}\psi\right) \tag{II.38}$$

$$\omega = \Delta_\mathrm{pol} u \equiv \left(\frac{1}{R}\partial_R\left(R\partial_R\right) + \partial_Z^2\right)u \tag{II.39}$$

Taking these additional variables into account, the base reduced MHD model solves the equations for seven variables: $\{\psi, u, T, \rho, j, \omega, v_\parallel\}$.

Numerical implementation For solving the equations, the finite element method (FEM), introduced briefly in the appendix A, is used. It requires the transformation of the equations into the so-called weak form by multiplying them with appropriate test functions and integrating over the domain. Furthermore, the variables are represented in terms of basis functions. JOREK uses the Galerkin method, meaning that the basis and test functions belong to the same class of functions, a specific kind of cubic polynomials.

The poloidal plane is discretized in G^1 continuous Bezier patches [Cza08] consisting of cubic polynomials (an extension to higher order elements is available [Pam22]) using an isoparametric approach, meaning that the coordinates are decomposed into the same basis functions as the variables. Due to the continuity constraints on values and their derivatives at adjacent elements, the number of degrees of freedom per node and variable reduces to four. Depending on the application, the use of a flux-surface aligned grid containing one or multiple X-points as shown in figure II.10 can be beneficial to accurately capture the high an-isotropy of the parallel and perpendicular heat flux. Furthermore, the grid can be extended to the PFCs to allow for realistic geometries especially important for SOL physics.

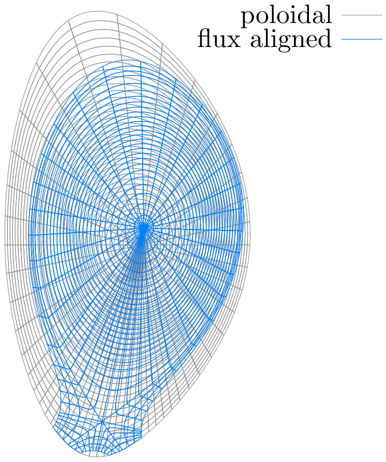

Figure II.10: The initial equilibrium is calculated on the poloidal grid (grey) to allow the optional construction of a flux-aligned grid (blue). Note that a coarse discretization was chosen here for visual purposes.

The toroidal periodicity of the system is exploited by decomposing the variables into Fourier harmonics in the toroidal direction. The temporal discretization is perfomed with an implicit time stepping, alleviating the CFL condition to allow for larger time steps without losing stability. An equation of the form:

$$\frac{\partial \mathbf{A}(\mathbf{u})}{\partial t} = \mathbf{B}(\mathbf{u}, t), \tag{II.40}$$

depending on the physical variables $\mathbf{u}$, can be advanced by linearizing the time step to obtain the form:

$$\left[(1+\xi)\left(\frac{\partial \mathbf{A}}{\partial \mathbf{u}}\right)^n - \Delta t\theta\left(\frac{\partial \mathbf{B}}{\partial \mathbf{u}}\right)^n\right]\delta\mathbf{u}^n = \Delta t\mathbf{B}^n + \xi\left(\frac{\partial \mathbf{A}}{\partial \mathbf{u}}\right)^{n-1}\delta\mathbf{u}^{n-1}, \tag{II.41}$$

where $\delta\mathbf{u}^n$ stands for the change of $\mathbf{u}$ from time step n to $n+1$. Setting $\{\theta, \xi\} = \{0.5, 0\}$ corresponds to the Crank-Nicholson scheme, whereas $\{\theta, \xi\} = \{1, 0.5\}$ is the Gears scheme. A non-linear time stepping scheme as introduced here [Fra15] is available as well. As the massive size of the matrix on the LHS forbids a direct inversion of the system for most cases of interest, an iterative scheme is applied with the direct solution per Fourier harmonic used for the pre-conditioner. A generalization to construct the pre-conditioner based on the interaction of multiple harmonics proved to speed up the simulation in its non-linear phase [Hol21].

Boundary conditions The FEM model allows a flexible setting of boundary conditions of the Dirichlet type, where the value of a variable is fixed to $u = f(\mathbf{u}, t)$ or the Neumann type, where the derivative normal to the boundary is set to $\boldsymbol{\nabla} u \cdot \mathbf{n} = f(\mathbf{u}, n)$ with $\mathbf{n}$ being the unit vector normal to the boundary, pointing outwards.

In the applications presented here, ρ and T are usually fixed to their initial values, while u, ω and $v_{\|}$ are set to 0. In the case of *fixed boundary* conditions equivalent to an ideal wall at the computational boundary, ψ and j on the boundary do not vary in time. For *free-boundary* simulations, see section II.5.2, the poloidal flux and current density on the boundary can vary.

In the region of the target, where magnetic field lines intersect the boundary, special boundary conditions are set. Here, the component of $v_{\|}$ parallel to $\mathbf{n}$ is set to the sound speed according to the Bohm criterion introduced in section II.2. Simultaneously, the heat flux is imposed by:

$$\mathbf{q} \cdot \mathbf{n} = \gamma_{sh} n_e k_B T_e c_s \frac{\mathbf{B} \cdot \mathbf{n}}{B}, \tag{II.42}$$

according to sheath theory (II.11). There are several options to set ρ in this case. A self-consistent evolution would require the inclusion of neutrals in the simulation, as the ions neutralize at the boundary and are scattered back into the SOL, where they either ionize directly or diffuse inside the core before ionization. To simplify simulations, it is also possible to set ρ to free outflow conditions, reflect them completely or a combination both. Here, a complete reflection signifies an instant re-ionization when the particle reaches the computational boundary.

II.5.2 Coupling with EM codes

When ψ is set constant over time at the boundary, it acts like a closely fitting ideal wall and stabilizes modes that are influenced by induced eddy currents in a surrounding conductive wall. In order to take into account the effects of a resistive wall at arbitrary distance, or time-varying external currents in general, an extension to free-boundary is employed. It requires calculating the plasma contribution of B_{tan} on the boundary as well as the contribution from external currents in the surrounding structures and a free evolution of j on the boundary. The necessary boundary condition in reduced MHD is given by the tangential magnetic field on the boundary in the current definition equation [Höl12].:

$$\begin{aligned}\int \frac{1}{R^2} j v^* \mathrm{d}V &= \int \frac{1}{R^2} \Delta^* \psi v^* \mathrm{d}V \\ &= -\int \frac{1}{R^2} \boldsymbol{\nabla}\psi \cdot \boldsymbol{\nabla} v^* \mathrm{d}V + \int \frac{1}{R} v^* \underbrace{\frac{\boldsymbol{\nabla}\psi \cdot \mathbf{n}}{R}}_{=B_{\tan}} \mathrm{d}S,\end{aligned} \tag{II.43}$$

where v^* is the test function and $\frac{1}{R}\boldsymbol{\nabla}\psi \cdot \mathbf{n} = (\mathbf{B} \times \mathbf{n}) \cdot \mathbf{e}_\phi$. $B_{\tan}$ has a contribution from both the plasma and the external currents $\mathbf{I}_w$.

To obtain the plasma contribution, we can either apply a boundary element method (BEM), using the fact that the magnetic field from the plasma can be calculated from the total magnetic field on the boundary [Han15], or alternatively, the **virtual casing principle** [Sha72].

In JOREK, the latter method is commonly used, which states that any field originating from a current distribution inside a closed domain V_p can be represented by a surface current $\mathbf{j}_{\text{equiv}}$ on its surface. Based on the derivation in [AS18], we show the main formalism in the following. Using Ampère's law, the vector potential $\mathbf{A}$ at any point $\mathbf{r}$ outside V_p can be calculated from the virtual current distribution $\mathbf{j}_{\text{equiv}}$ on the surface δV_p as:

$$\mathbf{A}(\mathbf{r}) = \frac{\mu_0}{4\pi} \int_{\delta V_p} \frac{\mathbf{j}_{\text{equiv}}}{|\mathbf{r} - \mathbf{r}'|} \mathrm{d}S. \tag{II.44}$$

The so-called coupling surface δV_p is represented by finite elements and located at the computational boundary of JOREK. Applying the FEM, we can write this as $\underline{\mathbf{M}}_{pe}\mathbf{A}^e = \underline{\mathbf{M}}_{pp}\mathbf{I}^{\text{equiv}}$, where $\mathbf{I}^{\text{equiv}}$ are the degrees of freedom (dofs) associated with the surface current distribution $\mathbf{j}_{\text{equiv}}$ and $\mathbf{A}^e$ are the dofs of the vector potential in the JOREK basis functions. The surface currents are represented in the basis of the EM code.

The expression above can be inverted to obtain the current distribution $\mathbf{I}_p^{\text{equiv}}$. Note that the currents are normalized by μ_0 and the prefactor of 4π is absorbed in the matrix definitions. As $\mathbf{A}$ in JOREK contains the contribution from both the plasma and external currents, we have to substract the external contribution in order to obtain $\mathbf{I}_p^{\text{equiv}}$:

$$\mathbf{I}_p^{\text{equiv}} = \underline{\mathbf{M}}_{pp}^{-1}(\underline{\mathbf{M}}_{pe}\mathbf{A}^e - \underline{\mathbf{M}}_{pw}\mathbf{I}_w), \tag{II.45}$$

where $\mathbf{I}_w$ are the degrees of freedom associated to the wall currents and $\underline{\mathbf{M}}_{pw}$ is the mututal inductance matrix between the coupling surface and the wall structures.

The currents in the structures outside of V_p vary according to the resistive-inductive equation in the following form:

$$\underline{\mathbf{M}}_{ww}\dot{\mathbf{I}}_w + \underline{\mathbf{R}}\mathbf{I}_w + \underline{\mathbf{M}}_{wp}\dot{\mathbf{I}}_p^{\text{equiv}} = \mathbf{U}_e, \tag{II.46}$$

where $\underline{\mathbf{M}}_{ww}$ is the self-inductance matrix of the structures, $\underline{\mathbf{R}}$ the resistance matrix and $\mathbf{U}_e$ is an externally applied voltage and the voltage by time-varying currents in the plasma can be expressed as $\underline{\mathbf{M}}_{wp}\dot{I}_p^{\text{equiv}}$.

Inserting (II.45) leads to:

$$\underbrace{\underline{\mathbf{M}}_{ww} - \underline{\mathbf{M}}_{wp}\underline{\mathbf{M}}_{pp}^{-1}\underline{\mathbf{M}}_{pw}}_{\equiv\underline{\tilde{\mathbf{M}}}_{ww}}\dot{\mathbf{I}}_w + \underline{\mathbf{R}}\mathbf{I}_w + \underbrace{\underline{\mathbf{M}}_{wp}\underline{\mathbf{M}}_{pp}^{-1}\underline{\mathbf{M}}_{pe}}_{\equiv\underline{\tilde{\mathbf{M}}}_{we}}\dot{\mathbf{A}}_e = \mathbf{U}_e, \tag{II.47}$$

where the contribution of the wall currents to the plasma changes $\dot{\mathbf{A}}_e$ needs to be subtracted.

To facilitate the time-stepping, the general eigenvalue problem $\left(\underline{\tilde{\mathbf{M}}}_{ww} - \lambda\underline{\mathbf{R}}\right)\mathbf{x} = 0$ is solved, yielding:

$$\underline{\mathbf{S}}^T\left(\underline{\mathbf{M}}_{ww} - \underline{\mathbf{M}}_{wp}\underline{\mathbf{M}}_{pp}^{-1}\underline{\mathbf{M}}_{pw}\right)\underline{\mathbf{S}} = \underline{\mathbf{D}} \quad \text{and} \quad \underline{\mathbf{S}}^T\underline{\mathbf{R}}\underline{\mathbf{S}} = I_d, \tag{II.48}$$

where $\underline{\mathbf{D}}$ is a diagonal matrix of the eigenvalues of the extended self-inductance matrix and I_d is the identity matrix. The currents are likewise transformed into their eigenvector basis $\underline{\mathbf{S}}\mathbf{I}_w = Y$. Details on this are found in [AS18].

Using the Biot-Savart formula, we can calculate B_{tan} at the JOREK boundary from the surface current distribution and the external currents as:

$$\mathbf{B}_{\text{tan}} = \left(\frac{\mu_0}{4\pi}\int_{\delta V_p}\frac{\mathbf{j}_{\text{equiv}}}{|\mathbf{r}-\mathbf{r}'|}\mathrm{d}S + \frac{\mu_0}{4\pi}\int_{V_w}\frac{\mathbf{j}_w}{|\mathbf{r}-\mathbf{r}'|}\mathrm{d}V\right)\times\mathbf{n}. \tag{II.49}$$

Using again the FEM, the equation above can be transformed into

$$\begin{aligned}\mathbf{B}_{\text{tan}}^e &= \underline{\mathbf{M}}_{ep}\mathbf{I}_p^{\text{equiv}} + \underline{\mathbf{M}}_{ew}\mathbf{I}_w \\ &= \underline{\mathbf{M}}_{ep}\underline{\mathbf{M}}_{pp}^{-1}\underline{\mathbf{M}}_{pe}\mathbf{A}^e + (\underline{\mathbf{M}}_{ew} - \underline{\mathbf{M}}_{ep}\underline{\mathbf{M}}_{pp}^{-1}\underline{\mathbf{M}}_{pw})\mathbf{I}_w,\end{aligned} \tag{II.50}$$

where the matrices $\underline{\mathbf{M}}_{ep}$ and $\underline{\mathbf{M}}_{ew}$ already contain the transformation into Fourier space and projection onto the JOREK basis functions.

Suitable EM codes that represent the conductive structures outside the plasma and the surface hosting the virtual surface current $\mathbf{I}_p^{\text{equiv}}$ perform the calculations of these matrices. JOREK has been coupled [Höl12] to the EM wall code STARWALL [Mer15], where the structures are represented by flat triangles in the thin wall approximation, meaning that they have zero width. The details of the equations and the STARWALL basis functions are presented in [Mer15, AS18]. As the matrices defined above only depend on the geometry of the problem, they are calculated once prior to the run and the time evolution of equation (II.46) is done inside JOREK. The ASDEX Upgrade conductive structures have been imported into STARWALL and benchmarks have been presented in [Sch20] to show the validity for VDEs in particular.

One objective of this PhD project is to apply the formalism above to couple JOREK to the EM code CARIDDI [Vil13] in collaboration with the respective code developers, which allows the inclusion of volumetric structures, holes and multiply connected domains. In addition, detailed CAD models can be imported for the inclusion of the realistic wall geometries. Details on this implementation can be found in section V.

II.5.3 Challenges of VDE modeling

Simulation results of unmitigated and mitigated VDEs with JOREK are presented in section IV based on the AUG experiments described in section III. As modeling large devices is numerically challenging because of the disparity of time scales and high temperature devices requiring better resolution of fine scale plasma structures, it is useful to perform studies in smaller devices to understand the underlying physics and perform first steps of code validation. An overview about modeling activities and present understanding is given in [Art23].

Empirical observations from experiments or high-fidelity simulations can then be used as constraints for simplified models. A range of 2D codes as DINA [Luk96], TSC [Jar86] or CarMa0NL [Vil13] are used to estimate axisymmetric loads including heat fluxes, vertical movement and electromagnetic loads. While some of these codes require inputs on the halo current width and temperature, reducing their predictive capabilities, DINA has been extended to allow for a self-consistent temperature evolution using a power balance model [Kir16]. While linear codes can predict the growth rates of a VDE [Seh16] and can thus be employed in scenario development, non-linear MHD codes are required for a self-consistent evolution of a VDE.

Apart from JOREK, the non-linear 3D full-MHD codes M3D [Par99], M3DC-1 [Jar08] and NIMROD [Gla99] are employed, where the first two rely on a discretization of the whole region (also including the conductive structures and active coils) in volumetric elements and NIMROD employs a Fourier decomposition in the toroidal direction similar to JOREK. While free-boundary simulations are only possible in the reduced MHD version of JOREK (an extension for free-boundary to full MHD is under development), simulations of mitigated disruptions have already been performed in full MHD with fixed boundary conditions. Despite the discrepancies in model and numerics, an extensive benchmark of VDE simulations between JOREK, M3DC-1 and NIMROD [Kre20, Art21b] showed the same dynamics and comparable forces on the machine.

Furthermore, boundary conditions are an important factor in the vertical motion of the plasma as the SOL temperature determines the decays of halo currents [Kre20, Bun20]. In particular, sheath boundary conditions as introduced in section II.2 are essential to model the conditions self-consistently including neutral physics [Bun19], thus, making the simulations more challenging. In particular, the ion saturation current limit proved to be numerically difficult, as shown here in a 2D validation of a hot VDE in COMPASS [Art21b] including sheath boundary conditions. Further validation studies against machines [Pfe18] for hot VDEs have been performed, where the importance of the boundary conditions for the vertical growth rate as well as the halo width and rotation was highlighted. While the vertical force prediction are predicted reliably as for example shown in [Miy11] and [Cla19], the question about the scaling of the horizontal forces remains unclear. Although, it was possible to reproduce the magnitude of the JET horizontal force in [Str17] (while imposing I_p), this was not successful in JOREK yet [Art23]. One possible explication is the absence of a toroidal variation of I_p in JOREK due to the boundary conditions, which however seem to be essential in experiments in JET and in simulations [Str17]. Further validation studies with JOREK are presented in [Art23].

III Experiments in ASDEX Upgrade

The major pillars for understanding physical phenomena consist of theory, real life experiments or computational experiments using appropriate numerical models. Experimental results, providing a direct representation of reality, come with the drawbacks of high costs of running a tokamak and the limitations of the diagnostic systems. Whereas simulations have to respect their respective regions of validity and it can be challenging to keep realistic parameters and various physical effects without rendering them too expensive. Nevertheless, they allow independent variation of parameters to disentangle different influences and exploration of new geometrical and parameter regimes.

In this thesis, both of these methods are explored to improve understanding of the underlying physics and to build a link between theory and reality. This was done by carrying out dedicated experiments in the ASDEX Upgrade tokamak with the purpose to use the results for validating the physical models of JOREK. This chapter contains the experimental observations of hot VDE discharges in section III.1 and SPI mitigated VDEs in section III.2.

III.1 Hot VDE experiments in AUG

Hot VDEs, introduced in section II.3.2. are generally characterized by larger heat loads and electromagnetic forces compared to major or mitigated disruptions. Therefore, understanding the consequences for large machines is paramount. The setup and experimental observations of the dedicated discharges carried out in AUG were described in [Sch23a] and are repeated in the following.

III.1.1 Setup of the hot VDE discharges

Four hot VDE discharges were performed for this study at different levels of plasma current and toroidal magnetic field as listed in table III.1. The resulting equilibria shown in figure III.1 are Ohmic L-modes with no additional heating to facilitate the import in JOREK. Furthermore, these parameters still permit carrying out unmitigated VDEs without endangering the machine integrity. The goal of the I_p variation is to investigate its influence on the halo current width as inspired by previous studies in COMPASS [Ada22], where the halo width varied with I_p due to the effects of the ion saturation current. Also the toroidal magnetic field was varied in one discharge (# 39720) to obtain the same initial q_{95} as in the reference discharge # 39655. Further investigation points are the characteristics of asymmetries and variation in the forces.

Table III.1: The main parameters of the hot VDE discharges in AUG that were performed for this study are summarized in the table below.

shot number	I_p	B_t	q_{95}
# 39655	0.8MA	-2.0 T	4
# 39718	0.6MA	-2.0 T	5.4
# 39720	0.6MA	-1.5 T	4
# 39722	0.4MA	-2.0 T	8

The VDEs start with a linear displacement of 2 cm downward within 22 ms initiated by the position controller starting at 2.97 s, while the PF coil currents are frozen except for the fast control coils (CoI). Due to the better diagnostic coverage in the lower divertor and the higher robustness of the machine to downward VDEs, they were preferred to upward VDEs. After the forced displacement, all PF coils are frozen except for the central solenoid, which still varies due to its long reaction time. In previous hot VDE discharges in AUG, e.g. described by Pautasso [Pau11], the PF coil currents varied during the displacement and thus influenced the movement.

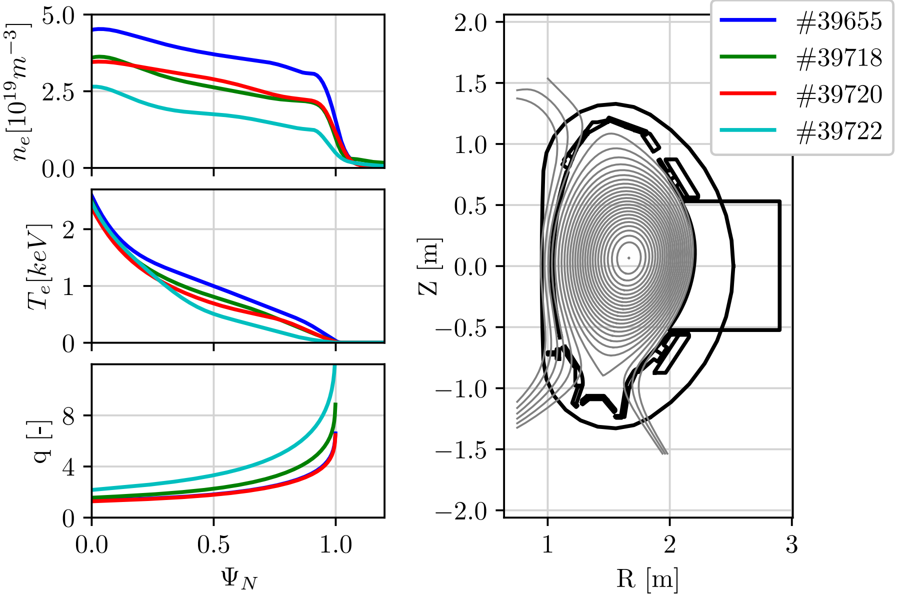

Figure III.1: Density, temperature and q profiles for the four hot VDE discharges before the movement is initiated. The right plot shows the reconstructed flux surfaces of discharge # 39655 as the shape of all cases is almost identical.

The time evolution of the hot VDE discharges is shown in figure III.2. The initial plasma displacement follows the prescribed target value in the control system, before the control system is switched off and the time scale is determined by the decay rate of the wall currents. The Passive Stabilizing Loop (PSL) with $\tau_{L/R} = 0.6\,\mathrm{s}$ contributes most to the VDE stabilization [Sch20] and was installed as the wall alone would not be sufficiently stabilizing [Gru93]. This coil consists of two incomplete loops that are connected by a bridge to ensure antisymmetric currents in the upper and lower loop that are supported with additional structural bridges with higher resistivity [Her10]. After arcing had been observed in the first operational years, resistances were installed to connect the upper and lower loop [Pin94]. Therefore, a net toroidal current flows in the PSL at large voltages as they occur during the CQ phase of a disruption.

During the displacement of the plasma, q_{95} decreases when the outer layers of the plasma are scraped off and current is re-induced in the core [Art20] as depicted in figure III.2 c). Due to the steepening of the current profile at the edge and the reduction of the edge safety factor, low-n current driven modes are triggered that lead to the TQ. The duration and onset of the TQ can not be determined by direct temperature measurements in the downward hot VDEs as they

Table III.2: The discharges show slightly different TQ onset times that occur at different values of q_{95}. τ_{CQ} is relatively short in all the cases, where # 39655 with the largest current has notably the fastest CQ. While the halo fraction is similar, the TPF of the halo currents varies, with # 39722 showing the largest asymmetries. The vertical force reaches up to 180 kN and scales with $I_{p,0}^2$.

shot #	t_{TQ}[s]	q_{95}@TQ	τ_{CQ} [ms]	HF [%]	TPF [-]	$F_{\max}$ [kN]
# 39655	3.073	2.54	2.83	28	1.5	184
# 39718	3.073	3.18	4.17	29	1.6	111
# 39720	3.064	2.46	3.17	34	1.7	94
# 39722	3.078	4.59	4.00	31	2.0	46

are out of sight for the midplane diagnostics. However, the TQ onset time can be determined from a growth in magnetic signals and soft X-ray measurements indicated in figure III.2 by a dashed vertical line. This occurs at an edge safety factor between 2.5 to 4.2 depending on the discharge. The current quench time τ_{CQ} varies from 2.8 to 4.1 ms, where # 39655 with the largest I_p has the fastest CQ. A summary of the hot VDE characteristics detailed in the following is provided in table III.2.

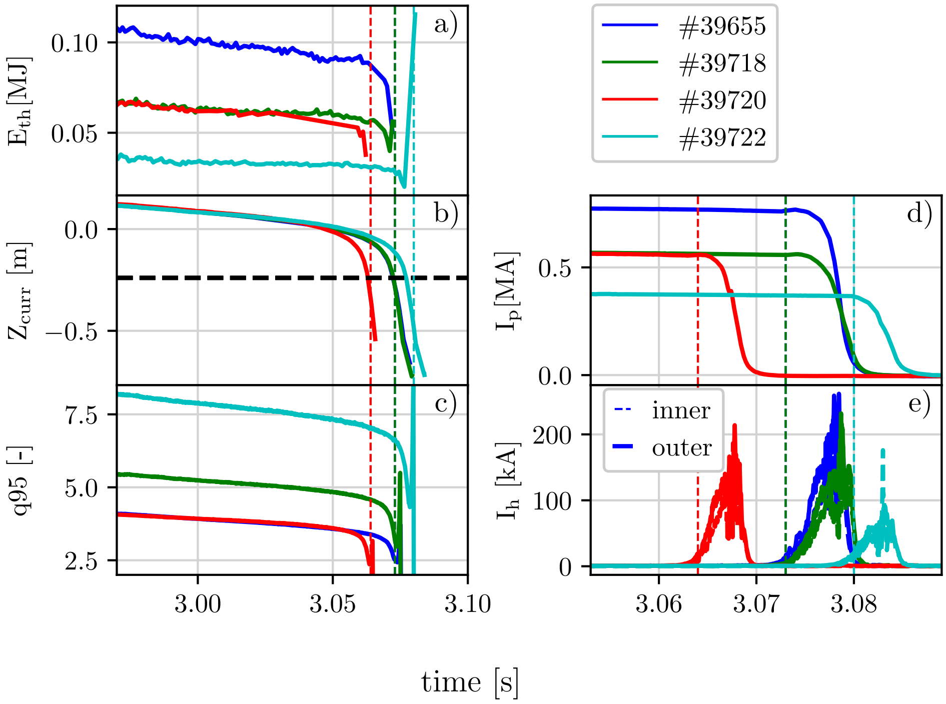

Figure III.2: Dedicated hot VDE discharges: The evolution of the (a) thermal energy, (b) vertical current centroid position, (c) edge safety factor q_{95}, (d) plasma current and (e) halo currents are shown. The vertical dashed line indicates the time of the TQ. The horizontal line in b) indicates at which displacement the X-point touches the wall approximately .

III.1.2 Halo current results

The halo fraction ($\frac{I_{h,\mathrm{max}}}{I_{p,0}}$) of these discharges lies with values around 30 % in the range of previous AUG experiments [Pau11], which tend to be on the high end of the spectrum observed in various tokamaks [Hen07]. While the TPF is in the range of 1.5 to 2, decreasing with I_p, the halo fraction does not vary significantly between the discharges, but fits with the I_p^2/B_t or I_p/q_{95} scaling previously observed [Gra96]. The time evolution of the halo current in different sectors and the TPF are shown in figure III.3, where the TPF at the time of maximum halo current is marked with a circle as this usually used as a reference in disruption databases [Eid15].

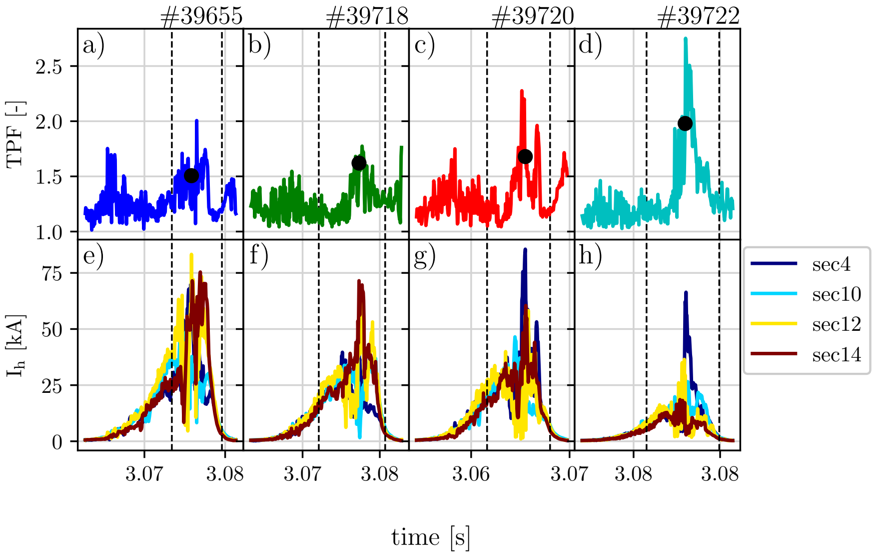

Figure III.3: The first row shows the evolution of the TPF, where the value at the time of largest I_h is marked with a dot. The second row shows the evolution of the halo current itself in the various sectors. The vertical lines mark the times, where I_p decayed from 95 to 10 % of the pre-disruption value respectively.

Secondary MHD activity are likely the cause for the largest asymmetries occurring during the CQ phase. This can be the sign of one or multiple loss events during the CQ, even leading to a second I_p spike in # 39720. The cases with the highest level of asymmetries result from localized activity rather than a rotating mode, as the maximum of the current does not vary between sectors. In figure III.3, one can see that the asymmetry is mostly due to a spike in one sector. Therefore, either the rotation is slower than the CQ time scale or no rotation is present. According to [Sap22], the expected frequency is in the range of 100 to 500 Hz, and therefore too slow to see multiple rotations in accordance to previous observations of up to one rotation during a disruption [Pau11]. However, the discharges # 39655 and # 39718 display some rotation as the maximum of the current continuously displaces between the sectors. This is even more apparent when looking at the tiles with better toroidal coverage [Sch23a].

The halo current width illustrated in figure III.4 does not show significant variation of the halo width with I_p in contrast to previous observations in COMPASS [Ada22]. While the current in the outermost tiles (DUIoo and DUAm) appears lower when normalized to the pre-TQ I_p, they still carry a significant fraction of the halo current. Note also that the measurements at

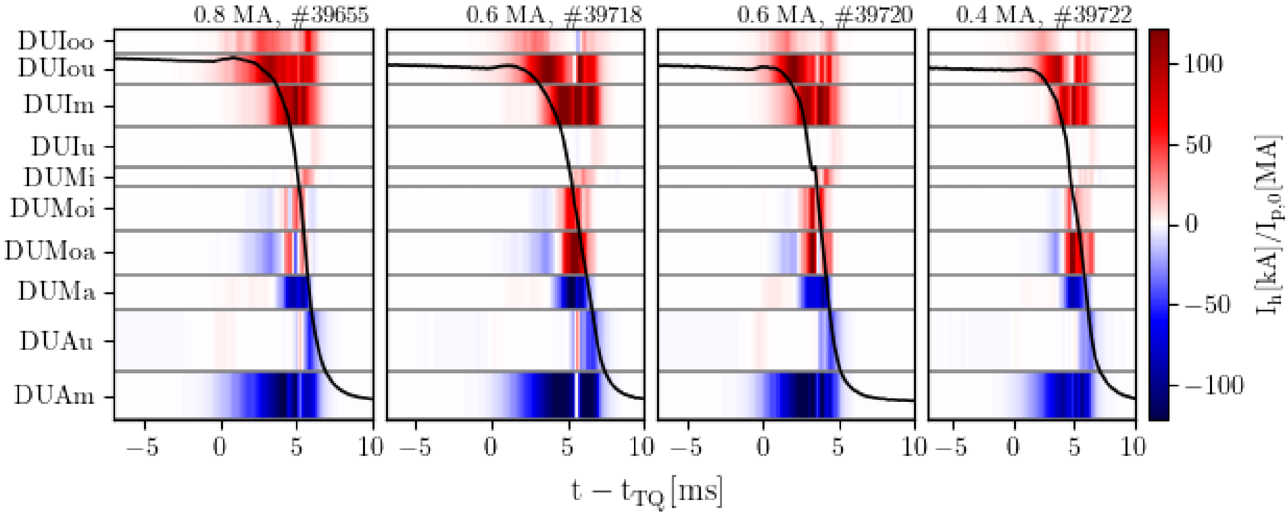

Figure III.4: The distribution of the halo current normalized by the the initial I_p does not show a significant variation of the width with I_p.

some tiles saturated during the large I_p shots and, furthermore, that the current normal to the surface is measured, which depends on the incidence angle of the magnetic field, so that a meaningful conclusion about the halo width dependence with I_p cannot be drawn. The change of sign of the current measurements indicate that the contact point of the plasma is located on the outer side of divertor baffle between DUMa and DUMoa. However, the spatial extent of the tiles leads to some uncertainties in the exact location. Similar to previous observations [Pau11], the tiles in the divertor legs (DUIu, DUAu, see figure II.7) measure less current as they are geometrically shielded during the disruption.

III.1.3 Force measurements

It was already pointed out in section II.4 that the measurement of vertical forces is not straightforward as the whole system needs to be taken into account. An estimation based on the extension of the suspension rods leads to a value in the range of 50 to 180 kN that scales with $I_{p,0}^2$ as pointed out in section II.3.4, which is depicted in figure III.5 a). The time evolution of the vertical force in figure III.5 c) gives indications about the sources of the force. During the forced displacement by the control coils indicated by the first dashed lines, the force increases rapidly due to the mirror currents in the vessel. Afterwards, the force is due to the displacement of the plasma interacting mainly with the PSL. Due to inertia or vessel shielding effects, the peak of the force is after the decay of the plasma current. After the force decreases, the vessel continues to oscillate with some contribution possibly due to the net current that was transferred to the vessel.

The horizontal displacement is more difficult to interpret as the diagnostics are connected to the port and are therefore subject to oscillations. When these perturbations are large, a clear displacement cannot be seen. However, for # 39718 to # 39722, a clear horizontal displacement is observed as shown in figure III.5 d), where opposite sectors show a displacement of opposite sign and equal magnitude. These cases also show the largest TPF observed in the four hot VDE

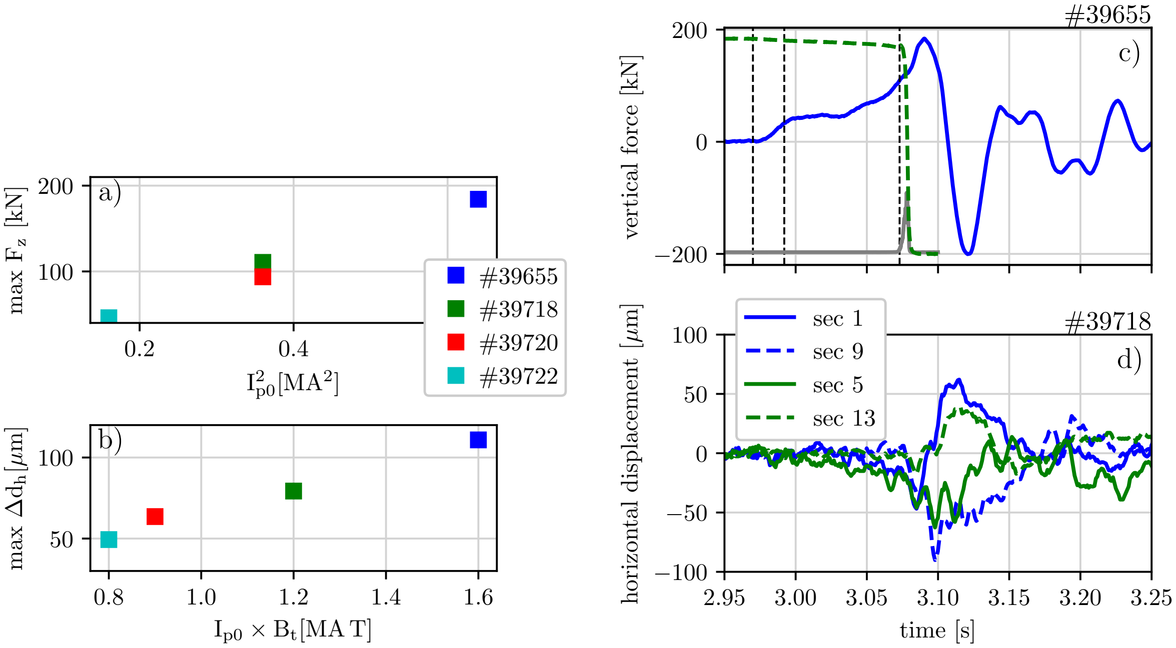

Figure III.5: a) The maximum of the vertical force F_z increases proportionally with $I_{p,0}^2$ and b) the horizontal displacement scales with $I_{p,0} \times B_t$.
c) Evolution of the F_z (blue), where the start of the VDE, the end of the forced displacement phase and the time of the TQ onset are marked by vertical lines. I_p and I_h (green and grey) are given in arbitrary units as a reference. d) The displacement in opposite sectors (indicated by the same color) is of equal magnitude and opposite sign, confirming a small sideways force.

discharges. The direction of the displacement varies between the discharges and there is no sign of rotation in the force. An estimate of the horizontal force impulse in AUG VDEs was given in [Pau11] to be around 220 N s based on the duration of the halo current asymmetries and the vessel damping characteristics. Consequently, this value can only correspond to a minor I_p asymmetry when applying Noll's formula inversely. The sideways impulse in the discharges presented in this section is expected to be similar, as the magnitude of the displacement and halo current asymmetries is comparable. Furthermore, the magnitudes of the displacement scales with $I_{p,0} \times B_t$ as expected from Noll's formula [Nol97] given that the relative asymmetries are the same.

III.1.4 Radiation

The total radiation during a disruption gives an estimate of its importance as a loss channel of the stored energy, which is expected to be smaller in machines with metal rather than carbon based PFCs [Leh13].

The measurements by the foil bolometers illustrated in figure III.6 show the total radiation in three sectors, which are time integrated to 0.35 MJ, 0.11 MJ, 0.13 MJ and 0.07 MJ for # 39655 to # 39722, representing around 20 to 30 % of the energy content of the plasma (E_{mag}+E_{th}), where E_{mag} is given by:

$$E_{\mathrm{mag}} = \frac{\mu_0}{2} R \left(\log\left(\frac{8R}{a}\right) - 2 + \frac{l_i}{2} \right) I_{p,0}^2, \tag{III.1}$$

with R being the major radius, a the minor radius and l_i the internal inductance.

The time resolution of the foil bolometers does not allow an identification of the distribution between CQ and TQ. Whereas measurements by AXUV diods (not shown here) indicate that most energy is radiated during the CQ, also given that the thermal energy of the L-mode is only a fraction of the magnetic one. The radiation peak occurs through a later phase in the CQ, where it is assumed that the LCFS disappeared and the plasma current flows only in the SOL. In the case of a hot VDE, the impurities present in the machine can enter the plasma during phases of MHD activity or the radiation can also occur in the SOL. Whereas, background impurities present in standard operation can play a role in both hot VDEs and major disruption after the plasma cooled down. The peak in sector 16 shown in figure III.6 is related to the interaction with the wall at this location, as could be seen in a camera capture in the same sector. As the radiation fraction is calculated from the average of the sectors, this can lead to an overestimation of its value in this case with localized activity.

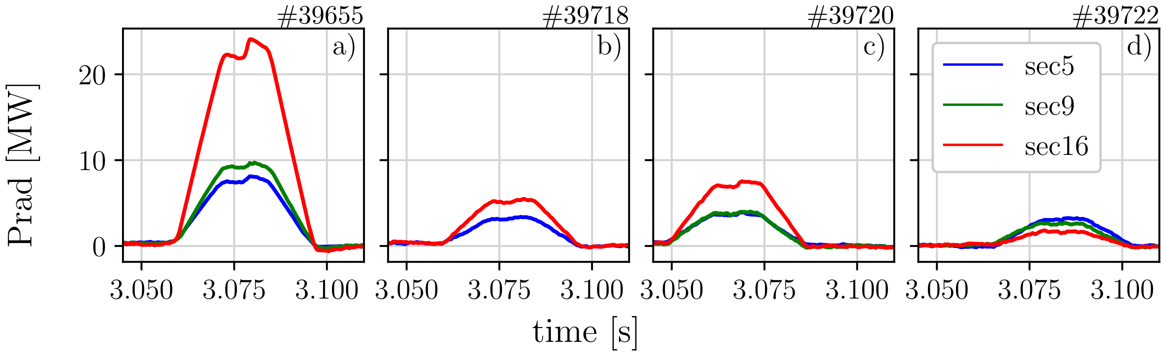

Figure III.6: The measurements of foil bolometers in three sectors show low levels of radiation. Note, that the signals are averaged over time, so that the increase starts before the TQ sets in.

III.1.5 Summary of the hot VDE discharges

The four dedicated discharges that were presented in this section are in accordance with previous observations in AUG regarding the magnitude of halo currents, their asymmetries, the vertical forces and the radiation fraction. They were designed for reproducibility and easy import in a numerical code by choosing an Ohmic L-mode without any additional heating and by using a defined vertical perturbation on the plasma by the position control coils. Furthermore, the settings of the diagnostics were adjusted when possible (bolometers) to increase the time resolution in order to capture the dynamics of the disruption. Therefore, they provide a good basis for code validation.

III.2 Mitigated VDEs

Hot VDEs are known to be one of the most destructive events due to the high heat loads, vertical forces and a high degree of asymmetry. Therefore, mitigation systems like introduced in section II.3.5 are employed to limit the detrimental effects of disruptions. A set of SPI mitigated VDE discharges were performed in AUG in order to study the mitigation efficiency into a displaced plasma. The experimental results were also published in [Sch23b].

Similar studies have been performed in DIII-D [Hol15] with an MGI system and JET [Ger21, Ger23] using SPI, showing that a late mitigation still reduces heat loads, asymmetries and forces. In the following, first the setup of the discharges is laid out in section III.2.1 including an overview of the results. This is followed by the halo current measurements in section III.2.2 and the force and radiation measurements in section III.2.3.

III.2.1 Setup of the mitigated VDE discharges

The SPI system described in section II.3.5 was used for the mitigated VDE discharges described in the following. In total, three discharges have been performed based on the 800 kA hot VDE (# 39655) presented in section III.1.1. The triggering of the VDE is performed again by a forced displacement by the control coils of 2 cm in 22 ms. As the time evolution of the vertical axis is known from # 39655, it is possible to calculate the triggering time of the pellet exactly to induce a TQ at different phases of the VDE, where the selected times are summarized in table III.3. We saw that, first, the vertical axis indeed evolves in a reproducible way for all discharges, and, second, the delay between the trigger time and shard arrival at the plasma boundary is consistently at 24 to 26 ms with the arrival time given by the first radiation increase in the AXUV diodes. The longer times correspond to the cases with larger displacement at shard arrival, while the SPI speed was comparable for the different pellets as listed in table III.3. Overall, this setup proves to be well-defined to study the influence of the injection times on the disruption consequences.

Table III.3: The time of the pellet trigger, of the observation by a camera and of the first light in the AXUV diodes. The speed and lengths as measured by the OPD camera deviate slightly from the nominal values of 230 m s^{-1} and 8.5 mm.

	trigger time	OPD time	arrival time	measured speed	measured length
# 40955	2.988 s	2.997 s	3.012 s	247 m/s	8.48 mm
# 40956	3.031 s	3.040 s	3.055 s	257 m/s	8.55 mm
# 40957	3.043 s	3.052 s	3.069 s	242 m/s	8.4 mm

Because the aim of this experiment is an efficient conversion of the stored energy into radiation and a fast CQ, the injected material consists to 100 % of Neon and the biggest pellet size available was chosen. The nominal pellet length of 8.5 mm and diameter of 8 mm result in 1.7×10^{22} Neon particles [Pap22].

Figure III.7 a) contains an overview of the experimental time traces of I_p and the poloidal halo current I_h measured on the divertor tiles. 3 to 4 ms after the shard arrival at the edge,

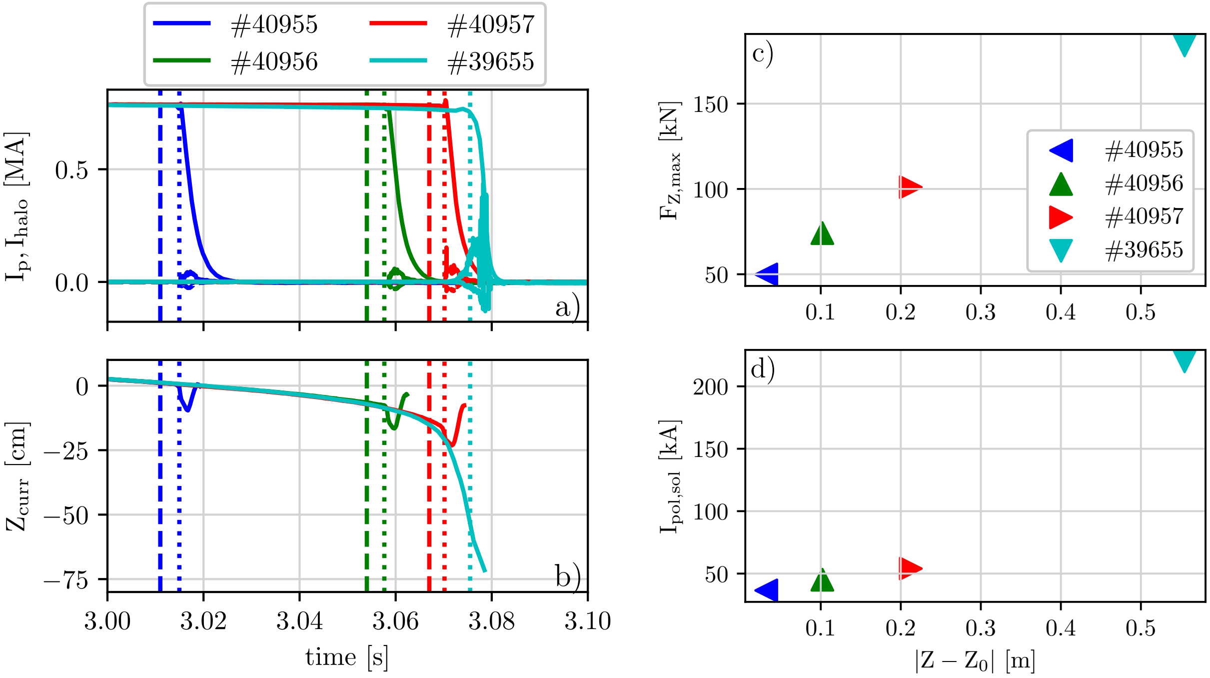

Figure III.7: The shattered pellets are injected at three different time points of the VDE, the dashed line marks the arrival of the shards in the plasma and the dotted one the time of TQ. After the TQ, a) I_p decays on a fast time scale and the poloidal halo currents are reduced in comparison with the hot VDE. Furthermore, the displacement of the current centroid Z_{curr} b) is substantially smaller. Both the c) peak of the vertical force and d) I_h are reduced.

the start of the I_p spike indicates the TQ onset, which is followed by a rapid current decay. The CQ duration varies from 5.0 to 5.4 ms with the later injection exhibiting slightly smaller τ_{CQ}, which are slower compared to the hot VDE with 3 ms. When comparing the dynamics, we observe that I_p initially decays faster in the mitigated cases than in the hot VDE due to the larger resistivity caused by the radiation induced low post-TQ temperature. But, the CQ rate accelerates towards the end in # 39655, leading to an overall faster decay. In contrast to the mitigated disruption, the evolution of the I_p during the CQ is given by the vertical displacement in the hot VDEs, where the relatively hot core carries a larger current density. Therefore, the loss of the LCFS at the end of the VDE accelerates the current decay and the vertical growth rate has a significant impact on τ_{CQ}. Whereas, the resistivity plays the dominant role in the radiation dominated cases.

After the TQ, the current centroid illustrated in figure III.7 b) first shows a small, fast downward excursion before the motion reverses like previously observed in AUG [Pau17]. These measurements are not particularly reliable during disruptions for the reasons described in II.4, but can still give an indication about the movement. The fast downward displacement at the beginning is expedited by the dragging effect [Nak96] that vertically displaces the plasma when a change of l_i occurs during the TQ as described in section II.3.2. This phase is followed by the broadening of the halo currents, stopping the vertical movement, and the loss of the LCFS, leading to a reversal the direction of motion. We will see in section IV.4 that the same qualitative behavior can be reproduced in the simulation.

III.2.2 Halo current measurements

The theory of the force reduction presented in section II.3.5 relies on the broadening of the halo region due to current diffusion in the cold post-TQ plasma with a flat temperature profile in the whole domain. Apart from the stagnation of Z_{curr}, evidence of a broad halo region is required to support this theory. The shunt measurements in figure III.8 confirm that the halo region is wider in the mitigated cases compared to the hot VDEs, where the currents are concentrated in the divertor region. When the plasma is mitigated with the Neon SPI, the halo currents reach up to the heat shields, while the current density remains lower compared to the unmitigated cases. Note that not all tiles in poloidal direction are equipped with measurements on the heat shield, therefore the value for these tiles has been interpolated for the SPI mitigated VDEs.

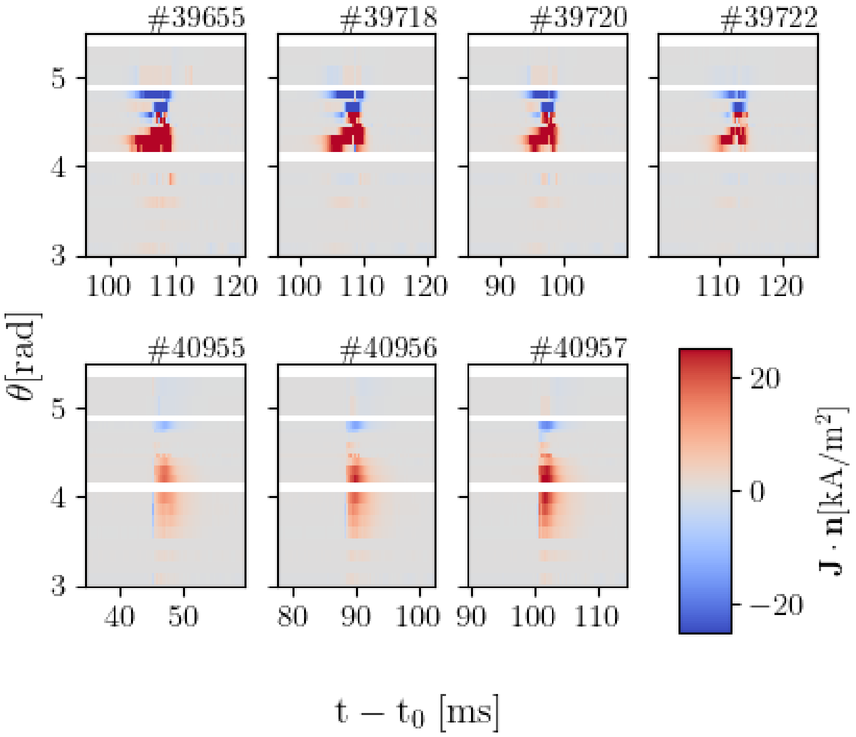

Figure III.8: The halo current density to the tiles in front of the PSL (top), the divertor (center) and the heat shield (bottom) for the unmitigated (1st row) and mitigated (2nd row) VDEs shows a larger halo width in the mitigated discharges. The time t_0 corresponds to the start of the forced displacement.

The magnitude of the poloidal halo current is significantly reduced with values varying from 35 to 54 kA in contrast to the 220 kA measured during the hot VDE # 39655. At the start of the TQ, a negative current layer is observed with opposite sign to the halo currents in the CQ phase. This has not been taken into account for the maximum I_h calculation in figure III.7 d), where the maximum during the CQ is taken. Regarding the asymmetries, the TPF is around 1.1 in all mitigated VDEs shown here, in contrast to a value of 1.5 for the hot VDE analyzed in section III.1.2. The absence of large asymmetries can be due to an increased value of q_{95} that allows the coupling of multiple n modes that even out toroidal variations. However, q_{95} cannot be determined directly by measurements after the TQ onset. In summary, both the magnitude and the level of asymmetry is reduced by the mitigation, while the current profile broadened in addition.

III.2.3 Radiation and force measurements

The injection of impurities aims to distribute the stored plasma energy over a larger surface by transforming it into radiation. To assess the mitigation efficiency, we can calculate the radiated energy during the disruption and compare it to the total energy of the system. Table III.4 summarizes the time integrated radiation energy measured by the foil bolometer system. Compared to the hot VDE discharges, the values are 2 to 7 times larger with a radiation fraction of approximately 55 %, which are on the lower spectrum of measurements during MGI mitigated disruptions in AUG in [Pau07]. Here, the radiation fraction is defined as:

$$f_{\mathrm{rad}} = \frac{E_{\mathrm{rad}}}{E_{\mathrm{th}} + E_{\mathrm{mag}}}, \tag{III.2}$$

similar to [Pau07], whereas the energy coupled to the structure is often subtracted in JET [Leh13] as it is not available for radiation. However, some of these data points come from the time, when AUG was equipped with carbon PFCs and additionally the stored plasma energy is lower in the cases presented here.

Table III.4: The total radiated energy is approximately 0.7 MJ, with a TPF of 1.1.

sector	# 40955	# 40956	# 40957
1	8.33×10^5 J	8.03×10^5 J	7.80×10^5 J
5	6.71×10^5 J	6.54×10^5 J	5.92×10^5 J
9	6.21×10^5 J	6.15×10^5 J	5.72×10^5 J
15	7.56×10^5 J	7.45×10^5 J	7.23×10^5 J
16	8.18×10^5 J	7.84×10^5 J	7.54×10^5 J
TPF	1.13	1.11	1.13
average energy	7.40×10^5 J	7.20×10^5 J	6.84×10^5 J

The radiated energy per sector does not show large asymmetries with a TPF of 1.1, where the sectors close to the SPI shatter head measure slightly higher levels. An overview of the energy losses is given in figure III.9 a), where the radiated energy is calculated from the bolometer signals and the coupled energy similar to what is described in [Leh13]. The magnetic energy in the PSL net current and the toroidal wall current is calculated as an estimate for the coupled energy, neglecting the change of the PF coil currents as they do not vary strongly. The conducted energy is then calculated from the missing energy.

According to this estimate, the heat fluxes reduce to a third compared to the unmitigated VDE. This observation would be consistent with measurements of mitigated upward VDEs in DIII-D [Hol15], where however the downward VDEs showed a smaller reduction for undetermined reasons. Note that the coupled energy is lower than the expected value of around 50 % for mitigated disruptions, so that the heat flux might be overestimated.

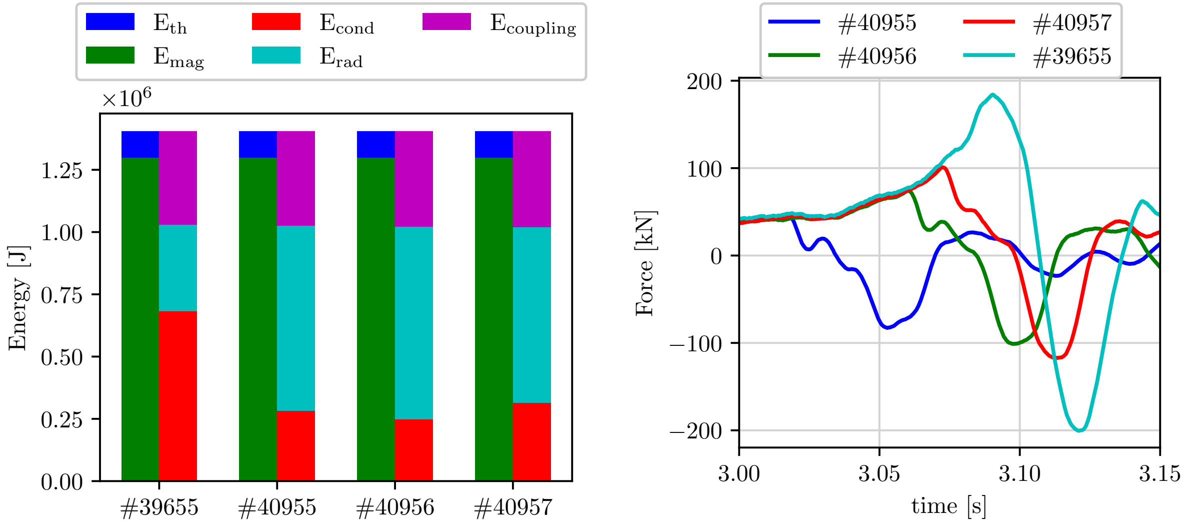

Figure III.9: a) The left block represents the stored energy of the plasma, while the right part shows the losses by radiation, coupling to conductive structures and conduction losses. b) The vertical force is reduced with earlier injection, while the negative peak is still present because of the current transfer into the vacuum vessel.

Figure III.7 c) shows how the peak of the vertical force is reduced with earlier injection, in particular, it is almost linear with $I_p \Delta Z_{\mathrm{curr}}$. For the earliest injection, the force reduces by 70 %, while for the later injection, 5 ms before the TQ in the hot VDE, it is reduced by 40 %. Previous experiments observed a similar reduction even at late injections at the time of TQ [Hol15]. The vacuum vessel oscillates after the I_p decayed completely due to the elasticity of the system and forces from the net current. If the negative peak can be attributed fully to the net current in the vacuum vessel, the downward peak for the unmitigated and mitigated VDEs would be of the same magnitude. However, as the excursion is larger in the case of the hot VDE, part of it is expected to originate from oscillation of the system.

III.2.4 Summary

The series of SPI mitigated VDEs gives insight about the mitigation efficiency of late injection into a moving plasma. A large part of the total stored energy (≈ 50 %) is radiated, where the radiation fraction does not vary significantly with the different injection times. The scaling of the force with the displacement of the plasma at the TQ onset time was found, which supports the theory about force mitigation introduced in section II.3.5. Another important finding is the widening of the halo width in impurity mitigated discharges, which agrees with previous experimental findings [Eid11] and explains why the current centroid movement in the experiment stagnates after the TQ. The broad halo region carries an important fraction of the total current, thus, the geometric center of the toroidal current remains closer to the midplane. At the same time, the small excursion from the midplane suggests a large q_{95} that would reduce the poloidal halo current and their heat loads. Even late injections reduce the mechanical forces and heat loads significantly, and can thus be beneficial if the mitigation system acts too late.

III.3 Conclusion of the experiments

The dedicated discharges in ASDEX Upgrade aimed to set up reproducible, clearly defined VDEs to facilitate the modeling with the JOREK code. Choosing an Ohmic L-mode and the given setup for the VDE trigger, facilitates the modeling with the code and eliminates unwanted influences, e.g. PF coil current variations due to an active controller, from the experiment. Repeating one discharge with the SPI mitigation proved that the VDE movement could be reproduced well

The experimental results for the unmitigated VDEs are within the observations of previous experiments, while the I_p and q_{95} scan allows to analyze their influence on asymmetries and the TQ onset further in the following chapter. Due to the saturation of some of the diagnostics like shunt measurements or magnetic measurements during disruptions, they have to be evaluated with care. Unfortunately, this prevented an evaluation of toroidal I_p asymmetries like previously observed in COMPASS and JET. The SPI mitigated VDE study was the first of its kind in AUG, where usually either the DMS is already triggered at small vertical excursions in unintended disruptions, while dedicated disruption experiments are carried out with a vertically centered plasmas. It showed the efficiency of mitigation at even larger displacements and furthermore supports the theory of force mitigation introduced in section II.3.5. These experiments are also used as a basis for the simulations presented in the following chapter.

IV Validation of JOREK against experiments

> *We live in a fantasy world, a world of illusion. The great task in life is to find reality.*
> – Iris Murdoch

With the knowledge about MHD and disruptions presented in section II and the experimental results in section III, we are able to set up JOREK simulations to validate the code for unmitigated and mitigated VDEs. This is an essential step for building trust in the numerical codes and models to ensure they contain the relevant physics, the parameters are chosen realistically and the code is used within its range of validity. In order to make extrapolations for future machines, we need a sound understanding of the physics in today's devices, a goal this section aims to contribute to.

It starts with the general setup of the simulations in section IV.1, before detailing the results of 2D simulations (section IV.2) and 3D simulations (section IV.3) of hot VDEs. This is followed by simulations of mitigated VDEs in section IV.4.

IV.1 Simulation setup

Simulations of VDEs naturally require free-boundary conditions (see II.5.2) as otherwise, the motion of the plasma would be stabilized by an implicit ideal wall at the computational boundary. The resistive wall modeling of the simulations in the following sections was carried out with STARWALL, which represents structures in the thin wall limit.

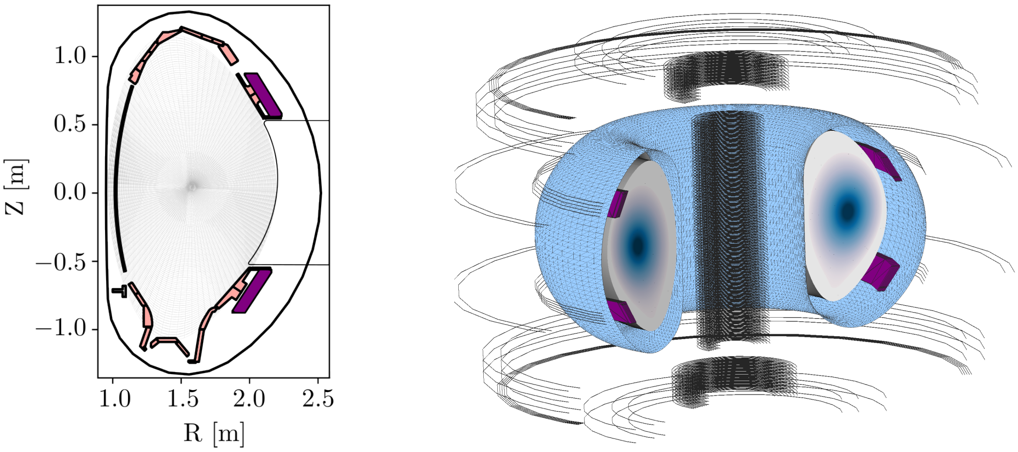

Figure IV.1: The Passive Stabilizing Loop (PSL) marked in violet stabilizes the vertical motion. The PFCs (rose), consisting of the divertor on the top and bottom, the heat shield and the tiles in front of the PSL, are not included in the model. The vacuum vessel surrounds the PFCs and the plasma. b) STARWALL model of the PF coils, vacuum vessel (blue) and PSL (violet).

Figure IV.1 a) depicts the poloidal cross-section of AUG components, where the PFCs, which are not included in the model, are colored in rose and the Passive Stabilizing Loop (PSL) in violet. The Vacuum Vessel (VV) in black surrounds the PSL, PFCs and plasma. For reference, the JOREK computational grid is added in grey. The PSL was included in AUG to stabilize the vertical position because the VV alone, with its large distance to the plasma, does not decrease the vertical growth rate γ_{VDE} sufficiently for the control system to interact [Gru93]. As STARWALL can only represent thin structures, the PSL is modeled by multiple bands in the radial direction to represent its width. Additionally, an inclination was introduced to model the structures more accurately and also leave more room for the computational domain. Taking into account the PSL geometry and copper resistivity, the self-inductance and resistance are $12.7\,\mu\mathrm{H}$ and $23\,\mu\Omega$ respectively, resulting in an $\mathcal{L}/\mathcal{R}$ time of $0.55\,\mathrm{s}$. The STARWALL model is depicted in figure IV.1 b), where the PSL is colored violet and the vacuum vessel blue. An initial validation of the setup was done in [Sch20] by performing a benchmark of γ_{VDE} with the linear MHD code CASTOR3D [Str16], employing, however, a simpler PSL model with vertically straight bands, called *straight PSL* in the following.

With a nominal resistivity of stainless steel ($0.72\,\mu\Omega\,\mathrm{m}$) and the maximum thickness ($15\,\mathrm{mm}$) of the AUG VV , the thin wall resistivity $\eta_{\mathrm{thin}} = \frac{\eta}{d_w}$ calculates to $5 \times 10^{-5}\,\Omega$, where d_w is the wall thickness. However, every two sectors of the VV are electrically isolated from one another and connected by bellows, so that the 16 sectors in AUG form 8 pairs of electrically connected octants. This increases the toroidal resistivity to a value of $3\,\mu\Omega\,\mathrm{m}$ [Gia15]. To take into account the longer path of the eddy currents inside the electrically connected sectors, η_{thin} is chosen to be $3 \times 10^{-5}\,\Omega$. This leads to an estimated wall time of approximately $60\,\mathrm{ms}$ according to the formula $\tau_R = \mu_0 r_w/\eta_{\mathrm{thin}}$ [Han89], where r_w is the radius of the wall cross-section. In applications where toroidal currents dominate instead of eddy currents in the octants, a higher η_{thin} can be applied.

Despite the possibility of creating flux-aligned grids mentioned in section II.5.1, we use a simpler polar grid as the significant displacement of the plasma during a VDE diminishes the benefit of the alignment. However, the extent of the computational boundary was adjusted to be large enough to reach the lower divertor baffle, as shown in figure IV.1 a).

The plasma equilibrium reconstructed with the Cliste code [McC99], based on measured kinetic profiles and magnetic diagnostics at the time of the VDE start, provides the profiles of ρ, T and FF' as well as a ψ map. First, a fixed-boundary equilibrium is solved by the Grad-Shafranov solver in JOREK given the profiles and ψ on the computational boundary. This initial solution is then used by the free-boundary equilibrium solver, which additionally requires the experimental PF coil currents, to re-iterate the calculation including the vacuum part. A more detailed description is given in [AS18].

Realistic parameters for the parallel heat diffusion are chosen by applying the Spitzer-Haerm parallel diffusivity, with an upper threshold of $3.6 \times 10^9\,\mathrm{m}^2\,\mathrm{s}^{-1}$, corresponding to a T_e of $820\,\mathrm{eV}$ to take account the heat flux limit and to avoid numerical instabilities. The heat diffusivity is set thus to:

$$\chi_\parallel = \begin{cases} \chi_{SH}\left(\frac{T_e}{T_{e,0}}\right)^{5/2} & \text{for } T_e < 820\mathrm{eV} \\ \chi_{SH}\left(\frac{820\,\mathrm{eV}}{T_{e,0}}\right)^{5/2} & \text{for } T_e \geq 820\mathrm{eV} \end{cases} \tag{IV.1}$$

with χ_{SH} being the Spitzer-Haerm [Spi53] value corresponding to the initial temperature at the magnetic axis $T_{e,0}$, and T_e being the local temperature.

The plasma resistivity η corresponds to the Spitzer value taking into account a Z_{eff} of 2. Again, there is a cutoff above a T_e of 520 eV for numerical reasons. It was found that the combination of Dirichlet boundary conditions and the Spitzer-Haerm T dependence in the heat diffusivity underestimate the heat flux, and thus increase the SOL temperature. To evaluate the effects of the SOL temperature and to obtain a more realistic heat flux, a minimum parallel heat diffusivity is introduced in some simulations with:

$$\chi_{\|} = \chi_{\|}\left(max\left(T_e, T_{min,\chi_{\|}}\right)\right), \tag{IV.2}$$

which effectively defines a temperature threshold, below which the parallel conductivity is not decreased further. Therefore, a larger value of $T_{min,\chi_{\|}}$ leads to a lower SOL temperatures. The perpendicular particle and heat diffusivity profiles are chosen such that the plasma is in steady state taking into account a particle source and Ohmic heating. If not specified differently, Dirichlet boundary conditions are used for T, ρ, ω and u, while the normal derivative of ψ is determined by STARWALL matrices and j is left free. As a consequence, T and ρ remain at their initial values and ω as well as u are set to 0 on the boundary throughout the simulation. Different sets of boundary conditions that take into account non-zero flows at the boundary are available for MHD codes [Bun19, Spi23] and can be included in JOREK in the future.

The artificial position controller implemented in JOREK [Sch20] initiates the VDE by displacing the plasma by 2 cm within 22 ms using the fast control coils like in the experiment. This setup was first used to model the hot VDE discharges in 2D as described in the following section.

IV.2 2D Simulations of hot VDEs

Hot VDEs are in general challenging to model because of the disparity in the involved time scales ranging from µs for fast MHD events to the resistive wall time scale of several to tens of ms in today's devices. Since they are also expensive to run, axisymmetric codes are often employed to study the 2D dynamics and evaluate loads on the machine. However, they cannot take into account the high asymmetries and large scale MHD activity including reconnection events that occur during hot VDEs. When appropriate constraints are used to take into account effects originating from stochastization and MHD events, it is possible to obtain similar behavior as in 3D simulations [Art23] regarding vertical forces, the CQ time and q_{95} evolution. Here, we focus on the simulations performed for # 39655, as the observations are also valid for the other cases. Some of the results presented in this section are contained in [Sch23a].

IV.2.1 VDE displacement and TQ

Based on the simulation setup described in section IV.1, the displacement phase is modeled to study various influences on γ_{VDE}. It was found that it depends on the geometry and resistance of the conducting structures, the plasma position as well as the SOL temperature T_{SOL}.

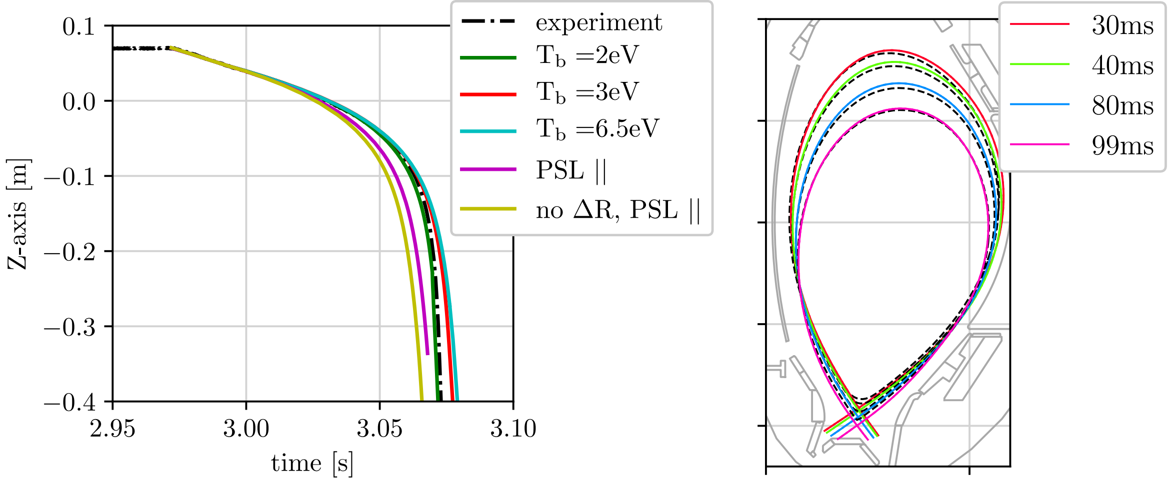

Figure IV.2: a) Different temperatures in the SOL due to different T_b at the computational boundary change the stabilizing influence of halo currents, while a straight PSL worsens the EM coupling to the plasma. In one case, the radial position of the plasma was changed with respect to the experimental reconstruction by ΔR. b) The experimental reconstruction of the separatrix (dashed) matches well with the shape in the simulation over different points in time.

Figure IV.2 a) illustrates how varying different parameters affects the vertical displacement of the plasma. Lower temperatures on the computational boundary that reduce T_{SOL} enhance the decay rate of the stabilizing halo currents, which accelerates the vertical motion, as described already in [Pfe18, Kre20]. Adding the inclination to the coil coil reduces γ_{VDE} since the small distance to the plasma leads to a strong EM-coupling as shown in the same figure. Therefore, including the inclination of the PSL both helps to model γ_{VDE} more realistically and leave more room for the computational boundary. Similarly, when the initial R position of the magnetic axis is shifted by 2 cm towards the center with respect to the experimental equilibrium, γ_{VDE} increases as the effective distance to the stabilizing structures is larger and the field index (II.17) is different.

Table IV.1: The vertical growth was fit over a time span of 10 ms after the active vertical control was switched off. While γ_{VDE} only changes slightly, it has a visible influence on the axis evolution.

	experiment	$\mathrm{T_b}$ =2eV	$\mathrm{T_b}$ =3eV	$\mathrm{T_b}$ =6.5eV	$\mathrm{PSL}_{\|\|}$	no ΔR, $\mathrm{PSL}_{\|\|}$
γ_{VDE} [s^{-1}]	33.63	32.14	32.23	32.40	34.51	35.00
rel. error [%]	-	-4.43	-4.16	-3.66	2.63	4.08

This shows the importance of the geometry of the closest structures and how their distance to the plasma influences the mutual inductance. Further influences on the VDE rate for various equilibria were studied in [Seh16]. Although the values of γ_{VDE} listed in table IV.1 deviate less than 10 % from the experimental value, the time evolution in figure IV.2 a) appears quite different due to the exponential mode growth ($\Delta Z \propto e^{t\gamma_{VDE}}$). By setting the parameters such that the axis displacement fits the experimental time trace, the separatrix shapes shown in figure IV.2 b) agree well over time with the experimental reconstruction.

When the outer layers are scraped off due to the motion, the plasma area reduces at almost constant I_p, resulting in a decrease of q_{95} as depicted in figure IV.3 a), where the simulation follows the experimental values up until the TQ. The evolution of q_{95} is directly related to the displacement as the latter determines the change of the plasma area until the TQ onset in # 39655 occurs at a q_{95} of approximately 2.5, which is also taken as the start time of the artificial TQ in the simulation. To reproduce the loss of the thermal energy, the perpendicular heat diffusivity is scaled up by a factor of 100 to reduce the core temperature on a time scale of $\tau_{TQ,90-20}$=2 ms. Simultaneously, the hyper-diffusivity of the current η_{hyp} is increased to mimic the current redistribution that occurs during the reconnection phase, which leads to the I_p spike in figure IV.3 b). After the temperature decays to a value of around 100 eV, the perpendicular heat diffusivity is reset to a constant value corresponding to $2\,\mathrm{m}^2\,\mathrm{s}^{-1}$ and likewise the perpendicular particle diffusion.

IV.2.2 Influences on CQ phase

The current quench duration and dynamics depend on the post-TQ plasma state, radiation and the vertical growth rate. Secondary MHD crashes were observed in the experiment that are related to asymmetries in the halo current and further losses of the thermal energy.

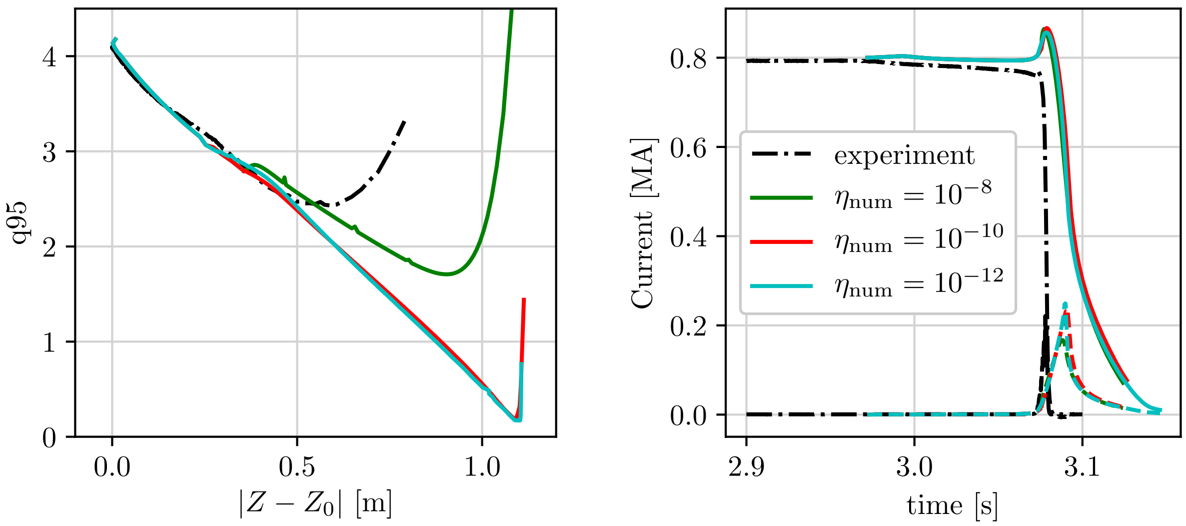

Figure IV.3: a) The safety factor on the edge decreases with the displacement similar to the experiment until the TQ sets in. If the current inside the core is not restricted, q_{95} continues to decrease in 2D simulations. Therefore, the hyper-resistivity was used here to regulate q_{95} during the CQ. b) The halo current and I_p decay are not significantly influenced by η_{hyp}.

Before investigating the influence of T_{SOL}, figure IV.3 a) and b) gives insight about the impact of the hyper-resistivity during the CQ for a $T_{min,\chi_{\parallel}}$ of 0 eV. The absence of non-axisymmetric instabilities in the 2D simulations allows q_{95} to reach a value below unity, which is in reality not possible as kink modes would lead to reconnection events that flatten the current profile and keep q_{95} at a larger value. Therefore, the hyper-resistivity term can be used like in the TQ phase to redistribute the current beyond the LCFS and push q_{95} into a more realistic regime. Figure IV.3 a) shows that q_{95} stays at around 2 with a η_{hyp} of 10^{-8} in JOREK normalized units, while smaller values of 10^{-10} to 10^{-12} allow q_{95} to decrease further. For η_{hyp}=10^{-8}, q_{95} reduces the poloidal halo current I_h by 30 % with respect to the simulations with smaller η_{hyp}, while the toroidal halo current is comparable in the three cases. However, the CQ duration τ_{CQ} is not influenced like indicated by figure IV.3 b) as long as the value of η_{hyp} is not chosen unrealistically large. The threshold for q_{95} can thus be controlled in 2D simulations by a parameter that has to be inferred from 3D simulations or experimental observations.

A balance of Ohmic heating and perpendicular heat transport determines the post-TQ core temperature in the absence of radiation. Whereas T_{SOL} is set by a balance of Ohmic heating as well as parallel and perpendicular heat transport. In reality, the core can still be partially or fully stochastic during the CQ, so that parallel transport is still relevant for the core T, which is an effect not captured by 2D simulations. Therefore, when T is known from experimental measurements or high-fidelity simulations, the perpendicular heat diffusion can be set to an adequate value to obtain the same profile.

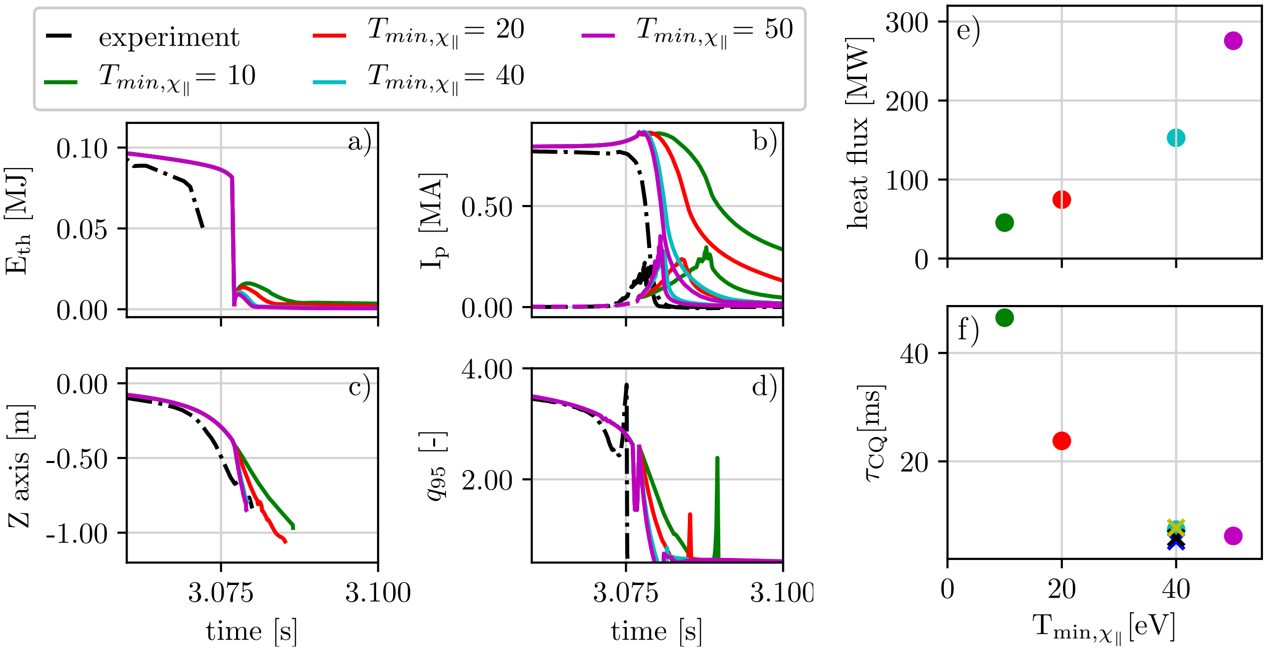

Figure IV.4: The c) vertical motion rate and d) q_{95} evolution correspond well to the experimental time traces until the TQ onset as the diagnostics also become less reliable after this point. The TQ was triggered artificially by large perpendicular heat conduction to lose the a) thermal energy an a time scale of ms. The scan $T_{min,\chi_\parallel}$ results in different e) peak boundary heat fluxes and f) τ_{CQ}, while the b) poloidal halo currents remain comparable. The crosses in f) show the influence of background impurities, which can decrease τ_{CQ} further.

Because of the $T^{-5/2}$ dependence of the parallel heat diffusivity, the heat transport along parallel magnetic field lines becomes inefficient when the plasma cools down, resulting in a post-TQ core temperature in the range of 100 eV. Therefore, the artificial TQ is stopped at this point in the 2D simulation by setting $\chi_\perp$ to a value of $2\,\mathrm{m}^2\,\mathrm{s}^{-1}$ in the whole domain. As T_e on the computational boundary is set to a few eV to avoid halo currents in the far SOL, the parallel heat transport also becomes inefficient in this region, leading to a τ_{CQ} of more than ten times the experimental value of 2.8 ms.

In a next step the influence of the boundary heat flux is evaluated. A lower threshold on the parallel heat diffusivity described by equation (IV.2) is used for this purpose, where $T_{\mathrm{min},\chi_\parallel}$ is varied from 10 to 50 eV. An overview about the simulation results is given in figure IV.4.

Larger heat conduction leads to a colder SOL, consequently accelerating the motion of the VDE (same figure c)) and the scraping off of the remaining core plasma. As the scraped-off current experiences a larger η in the cold SOL, the I_p decay is sped up and the vertical motion accelerated further. As a consequence, τ_{CQ} reduces from 46 to 6 ms with increasing $T_{\mathrm{min},\chi_\parallel}$ as depicted in figure IV.4 f), where the case with the largest heat flux is closest to the value of the experiment.

Figure IV.4 e) and f) show how τ_{CQ} reduces with larger peak boundary heat flux. With a faster movement of the magnetic axis for large values of the parallel heat conduction, q_{95} decreases accordingly as depicted in figure IV.4 d). However, I_h remains on similar levels for all the simulations presented here. The reheating after the TQ is reduced when $T_{\mathrm{min},\chi_\parallel}$ is smaller since the core temperature does not have enough time to recover as shown in figure IV.4 a).

In addition, impurities were included in the case with $T_{\mathrm{min},\chi_\parallel} = 40\,\mathrm{eV}$, where W or C was chosen with a number density n_{imp} of up to 2 % of the initial plasma core density, which reduces the CQ duration further by 20 to 30 %. These values are shown with crosses in IV.4 f). Note that the impurity model employed here is simplified, consisting only of a T dependent radiation function due to a uniform n_{imp} as an energy sink and does not include the increase of n_e or the influence of impurities on η. While we do not know n_{imp} and the species present in the disruption, it is clear that they can contribute to the dynamics and cause a discrepancy to the experiment. A more detailed scan of the influence of different quantities of Neon on τ_{CQ} and the VDE behavior is provided in section IV.4.6.

Another source of discrepancy is the halo width, which requires sheath boundary conditions to be modeled self-consistently as laid out in section II.5.3. In order to estimate the effects of the halo width, a space dependent resistivity is introduced by increasing η by a factor of 100 outside the divertor borders marked in figure IV.5. The restriction of the halo width also changes τ_{CQ} as shown in figure IV.5 d), where narrowing halo width decreases the duration from 21.9 to 8.5 ms when $T_{\mathrm{min},\chi_\parallel} = 20\,\mathrm{eV}$ or from 5.11 to 3.44 ms in the case of $T_{\mathrm{min},\chi_\parallel} = 50\,\mathrm{eV}$. While the majority of the halo current in the unrestricted case in figure IV.5 b) remains within the lower divertor boundaries, including the limit (c) can still have a significant effect.

The inclusion of sheath boundary conditions as well as the ion saturation current limit would both capture the heat flux and the halo width more accurately at the prize of more costly and numerically challenging simulations. This treatment is beyond the scope of this work, but has been implemented in JOREK and used for validation work of the displacement phase of hot

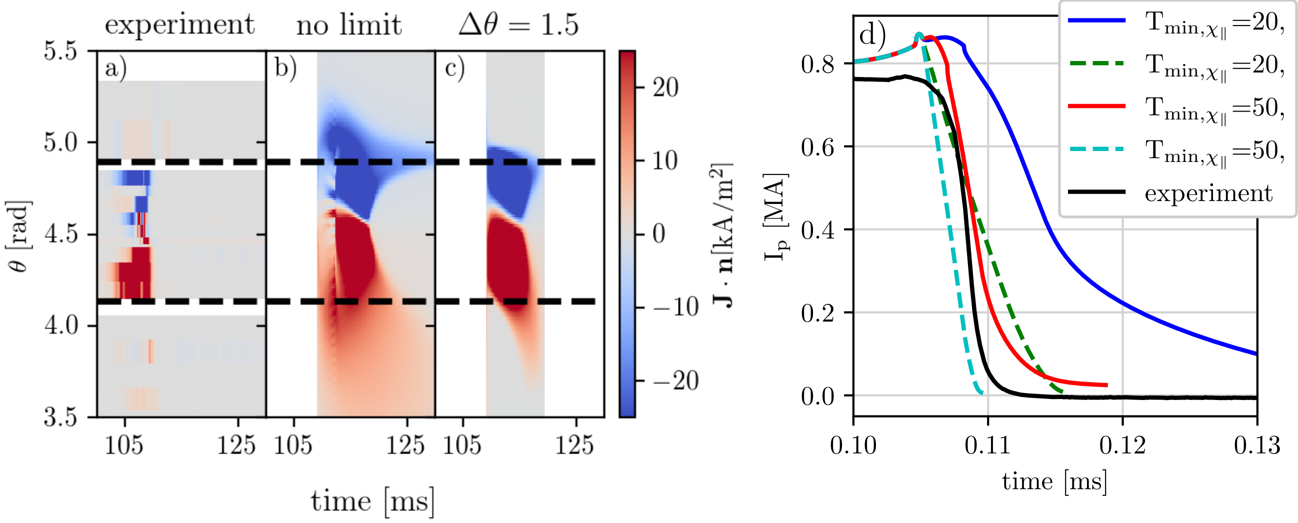

Figure IV.5: With b) no restrictions, the halo width in the simulation is larger than a) the experimental one. When the halo width is reduced by a space dependent η, the current quench duration is also reduced, where the dashed lines in d) correspond to the restricted cases. The current density plots show the case with $T_{\mathrm{min},\chi_\parallel} = 20\,\mathrm{eV}$.

VDEs in COMPASS [Art21a].

In summary, there are various parameters in the simulations that can influence the dynamics and cause deviation from the experimental results. First, the impurity content, which can influence the post-TQ core or SOL temperature, is not known in detail from the experiments. Second, the boundary conditions for the heat flux and the ion saturation current limit have a significant impact on the evolution of the plasma during the CQ as they determine the magnitude of stabilizing halo currents. Third, the non-axisymmetric effects like field line stochastization can lead to larger radial transport of heat, and thus, reduce the core temperature. Also, the limit on q_{95} is an effect not included in the 2D simulations, which limits the current density in the core and change I_h in the SOL.

IV.2.3 Vertical forces

The variation of T_{SOL} by imposing different boundary temperatures and changing the heat flux as described above led to a range of different τ_{CQ}. Similarly, changing parameters like η_{hyp} leads to different changes in the internal inductance during the TQ phase. The latter is related to the flattening of the current profile, where a larger change of l_i causes larger I_p spikes as shown in figure IV.6 a).

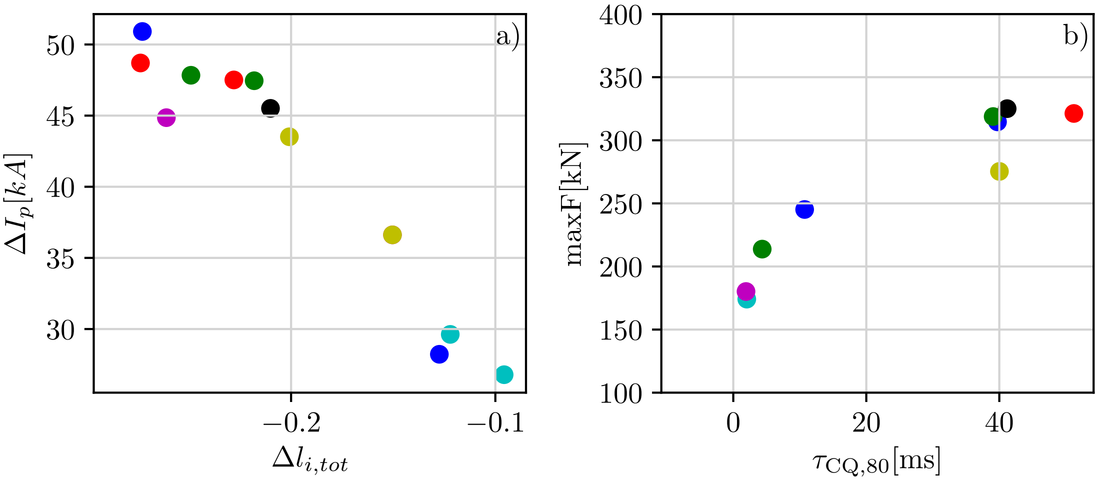

Figure IV.6: a) Larger variations in the internal inductance inside the computational domain leads to larger I_p spikes. b) A shorter CQ leads to a smaller force as the shielding by the wall currents is more effective.

The value of $\eta_{\mathrm{thin},w}$ chosen for the simulation leads to a wall time in the range of 30 to 50 ms. Therefore, the variation of the τ_{CQ} due to scans of parameters like η or $T_{\mathrm{min},\chi_{\parallel}}$, affects the shielding efficiency by the induced eddy currents in the vacuum vessel as shown in figure IV.6 b), where the maximum of the vertical force increases with τ_{CQ}. The vertical force in the simulation is calculated using the formula specified in [Pus15]:

$$\mathbf{e}_Z \cdot \mathbf{F}_w \equiv \int_{\mathrm{wall}+} \left((\mathbf{e}_Z \cdot \mathbf{B})\, \mathbf{B} - \frac{B^2}{2} \mathbf{e}_Z \right) \cdot \mathrm{d}\mathbf{S} - \mathbf{e}_Z \cdot \mathbf{F}_p, \tag{IV.3}$$

where $\mathbf{e}_Z$ is a unit vector that determines the component of the force on the wall $\mathbf{F}_w$ to be evaluated and the surface integral is performed on a closed surface just outside the wall. The total force on the plasma $\mathbf{F}_p$ is approximately 0 as otherwise the acceleration of its small mass would lead to large velocities, therefore only the surface integral is evaluated.

IV.2.4 Conclusion of the 2D simulations

This section contained an initial validation of axisymmetric simulations of JOREK-STARWALL against experimental hot VDE discharges. In summary, we saw that the vertical growth rate can be matched with the experiment, while it remains dependent on parameters as the geometry of passive components, the initial equilibrium position and the SOL temperature T_{SOL}. As the

TQ cannot be carried out self-consistently in axisymmetric simulations, the perpendicular heat conduction and η_{hyp} can be used to model the temperature loss and current flattening. For the subsequent CQ phase, it was found that the BC play an important role in the dynamics by determining T_{SOL} and the halo width. A colder SOL accelerates the VDE motion and, therefore, the scraping off of the plasma current, which then decays fast in the SOL. A scan in a lower threshold for the parallel heat conduction shows that τ_{CQ} can be matched by enhancing the boundary heat flux, while the halo current magnitude is not changed significantly.

The halo width requires the ion saturation current limit to be determined self-consistently, which is only possible when knowing the boundary density and temperature. These simulations are numerically challenging and not part of this work. Apart from the correct BC, external information about an effective heat transport and current hyper-diffusion is needed, which is used to model the effects of 3D MHD activity that are an important factor in hot VDE dynamics. Non-axisymmetric simulations, theory or empirical evidence from the experiment can be used as a guide on how to constrain 2D simulations accurately. E.g. theory would require q_{95} to stay above a certain threshold, likewise simulations or measurements can be used to calculate the effective heat transport through the separatrix. Using these constraints, hot VDEs can be modeled with 2D codes. While some parameters have to be adjusted to fit the experimental time traces, it is still useful to study their influence on 2D dynamics and provide estimates for axisymmetric loads. In conclusion, the magnitude of the poloidal halo currents did not depend significantly on the chosen boundary conditions, and a good match to the experiment was obtained. Furthermore, the vertical force depends on τ_{CQ} with its magnitude being in the same order as the estimated experimental value.

After these preliminary simulation and first observations, we can turn towards advanced non-axisymmetric simulations, which naturally contain the MHD activity that determines the dynamics of the TQ and CQ phases.

IV.3 3D Simulations of hot VDEs

The following section is dedicated to non-axisymmetric simulations of hot VDEs in ASDEX Upgrade, where the focus lies on the TQ phase in section IV.3.1, the CQ dynamics in section IV.3.2 and halo current properties in section IV.3.3. Finally, the forces are analyzed in section IV.3.4.

IV.3.1 Movement and TQ

The setup is the same as described in section IV.1 with the additional inclusion of the toroidal harmonics $n = 1..4$ and the diamagnetic drift according to equation (II.30), without which the equilibrium is unstable against a 2/1 tearing mode. The initial displacement phase is carried out as described in the 2D simulations (see section IV.2.1).

As shown in section III.1.1, the TQ onset time varies between the different discharges in the experiment. To see if the simulations capture this, VDE simulations for # 39655 to # 39722 are carried out up to the time when the thermal energy starts to decay. As the ratio between the edge and on-axis q indicates the plasma stability with respect to kink modes, it is computed for the different VDE discharges and compared to the experiment as presented in figure IV.7. While q_{95} decreases with the displacement, q_0 stays approximately constant as the current density in the core does not vary significantly.

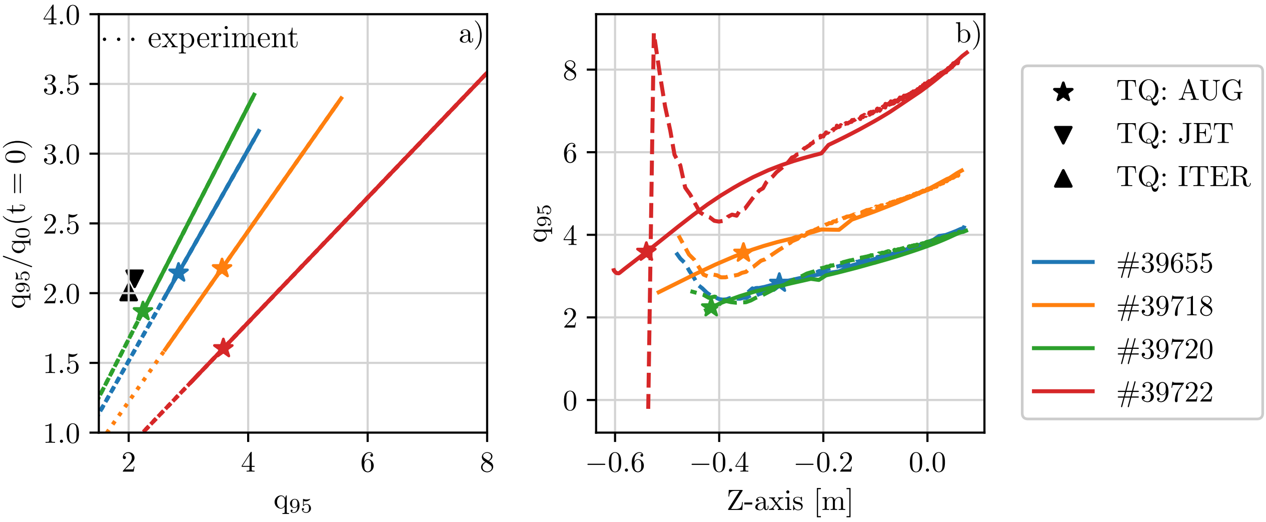

Figure IV.7: a) The ratio of q_{95} over q on axis indicates the stability against ideal kink modes. The onset point of the TQ in the AUG simulations is marked with a star. The experimental traces are shown by dashed lines, where q_0 was taken at the VDE start as the value does not vary significantly over time. Results of hot VDE simulations of JET and ITER [Art23] are indicated by triangles. b) Evolution of q_{95} with time for the hot VDE discharges in AUG and its experimental time traces.

The start of the TQ in the AUG simulation is marked with a star, while additional results from JET and ITER simulations [Art23] are added with triangles. In the simulations, the TQ onset is defined as the time, where the magnetic energies start to increase rapidly. The TQ start occurring at a $\frac{\mathrm{q}_{95}}{q_0}$ of around 2 as shown in figure IV.7 a) is consistent with the stability boundary of the ideal, external kink mode described in [Wes78]. This resolves the question, why the TQ in the different hot VDE discharges in AUG started at different q_{95}. In the cases with lower I_p, q_0 is larger as shown in figure III.1. As a result, the onset point of the mode growth is also shifted, leading to different starting points of the TQ. With γ_{VDE} differing slightly between the discharges, the TQ onset times vary accordingly in time. Future machines will operate at a q_0 of around 1, so the TQ is expected to occur at a value of q_{95} around 2 for hot VDEs. The further evolution of q_{95} during the CQ will be discussed in the following section.

In the simulations shown here, the most unstable mode is commonly an $n = 1$ mode, where the dominant poloidal mode number m is determined by the q value at the edge. In # 39655, for example, the TQ is triggered at a value of q_{95} of around 2.5. Therefore, an external 3/1 kink mode develops together with a 2/1 internal mode as illustrated in figure IV.8. Also a 6/2, 4/2 and other modes are present but remain subdominant. Since the vertical displacement continues during the TQ, the 3/1 mode disappears, while the 2/1 mode dominates after the thermal energy is lost. Whereas, in the discharge # 39722, where the TQ is triggered at a larger value of q_{95}, the 3/1 mode also reaches internally. This simulation is also special because of the absence of a $q = 2$ surface in the core, which makes the 3/1 mode the most unstable. Higher n pressure driven modes can also occur as the edge profiles steepen [Pfe18]. These are also observed here and can contribute to the edge stochastization.

Moreover, the TQ dynamics depend in general on the pre-TQ q-profile. When q_0 is close to 1, the external modes can couple to a 1/1 in the core, which leads to a mixing of the temperature inside the plasma before the energy is lost to the PFCs as described in [Bon86, Art23]. Since the q_0 is above 1 in all the AUG simulations shown here, this is not observed.

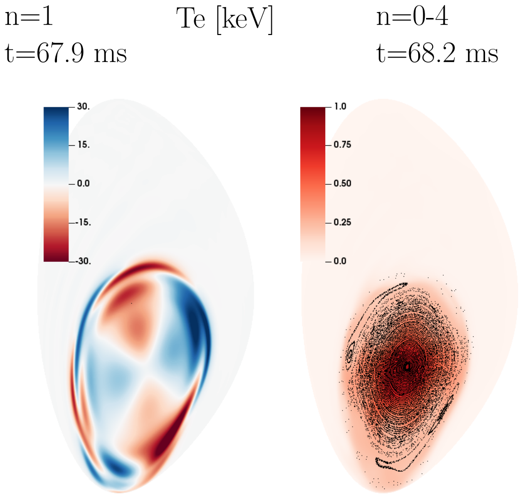

Figure IV.8: The $n = 1$ contribution to the temperature (left) allows to identify an external $m/n = 3/1$ mode together with an internal 2/1 mode. After the modes have sufficiently grown, the edge becomes stochastic and its temperature is lost first as illustrated on the right for the same simulation, where all modes (0-4) are included.

When the mode growth and overlap lead to a stochastization starting from the edge, the temperature is first lost in this area due to the shortened connection length between the plasma edge and the computational boundary, leading to a fast transport by parallel conduction. Figure IV.9 displays the evolution of the thermal energy and the corresponding profiles of T_e and J_ϕ for two different values of $T_{\mathrm{min},\chi_\parallel}$ and one additional case without diamagnetic drift. The core temperature remains constant initially while the core flux surfaces remain intact.

In the simulation with $T_{\mathrm{min},\chi_\parallel} = 20\,\mathrm{eV}$, the change of slope of E_{th} steepens visibly when the flux surfaces in the core become stochastic and the central temperature decreases on a faster time scale (figure IV.9 a)). While the current profile becomes more disturbed, the redistribution and maximum of the I_p spike occur with a delay to the TQ due to the slower time scale of the Shear Alfvén Waves responsible for the flattening [Nar23]. The time scale of the TQ in the $\tau_{TQ,90-20}$ definition lies in the range of 100 µs for the AUG plasmas. The simulations presented here also include diamagnetic drift effects, commonly not considered in simulations of hot VDEs. However, they only delay the TQ onset time slightly due to their stabilizing effect, while the time scale of the TQ is not influenced. Later, in the CQ phase, the diamagnetic drift is only a minor contribution to the flows as the pressure gradient is small.

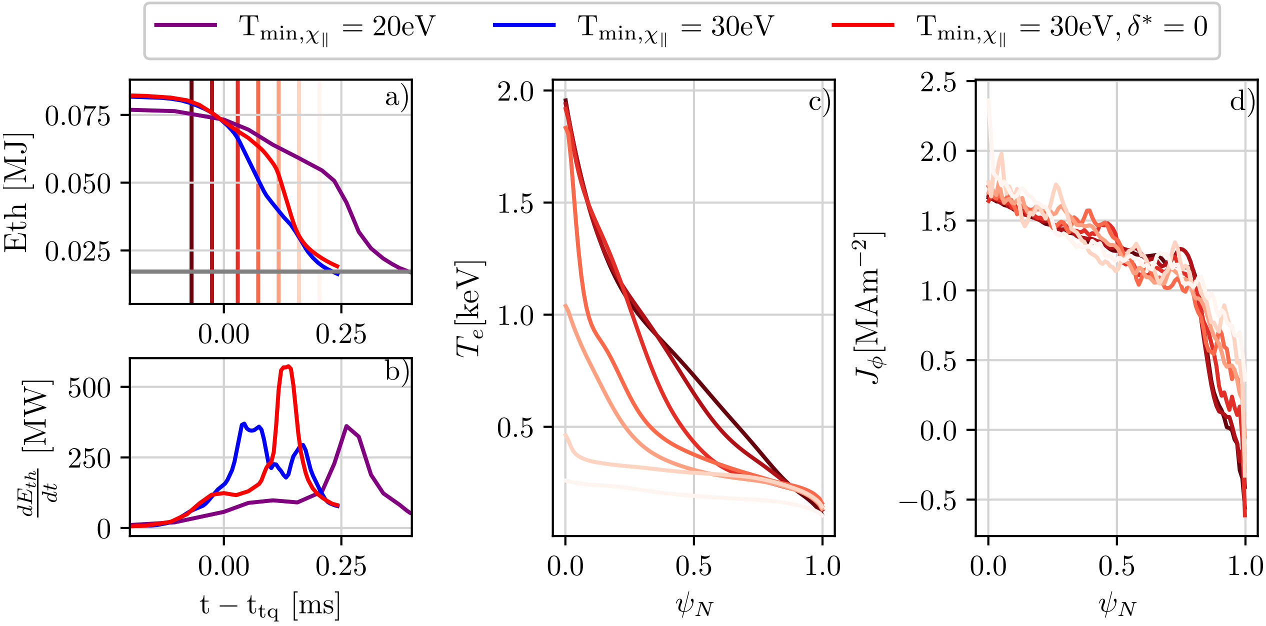

Figure IV.9: The a) thermal energy evolution and b) heat flux for simulations with different minimum values of $\chi_\parallel$. One case does not include the diamagnetic drift effect ($\delta^* = 0$), which changes the TQ onset time, but not the dynamics significantly. The profiles correspond to the case with $T_{\mathrm{min},\chi_\parallel} = 30\,\mathrm{eV}$, where the vertical lines mark the corresponding time slices in the first figure. The temperature decays first at the edge (c) until the plasma becomes stochastic and the core temperature collapses. The current redistribution (d) happens on a longer time scale than shown here. The vertical lines in a) correspond to the profiles on the right.

The final temperature after the TQ is around 100 eV because the parallel conduction becomes ineffective due to its $T_e^{5/2}$ dependence. The flattening of the current profile allows flux surfaces to reform and the core temperature to increase due to Ohmic heating. In reality, the reconnection in the TQ can cause an influx of impurities, which influence the post-TQ temperature by radiation. As the species and amount are unknown experimentally, they were not included in the simulations shown here.

IV.3.2 Current Quench dynamics

A post-TQ temperature in the order of 100 eV, as attainable by parallel conduction in the absence of radiation, would lead to long current quenches, which is not observed in the experiments presented in section III.1. Instead, τ_{CQ} is shortened by the rate of displacement and heat flux to the boundary as shown in section IV.2.2. In the 3D simulations, also secondary MHD instabilities play a role, which will be discussed in the following. Figure IV.10 displays the CQ dynamics for one exemplary case, where $T_{\mathrm{min},\chi_\parallel}$ was set to 40 eV. During the TQ and most of the CQ, the $n = 1$ energy dominates and the $n > 0$ kinetic and magnetic energies remain high during the CQ phase as the plasma is still MHD active. In most of the simulations presented here, the MHD activity imposes a minimum q_{95} during the majority of the CQ phase, which is also present in figure IV.10 c). Below a value of approximately 2, MHD crashes expel plasma current to keep this limit up. Eventually, when the plasma current has decayed significantly and the core area is small, q_{95} reaches a value of 1. The current evolution in- and outside the LCFS in figure IV.10 b) shows that the current inside the core decays quicker than I_p and the toroidal halo currents in the SOL are an important contribution to I_p. In the following the dynamics of the crashes are investigated in detail.

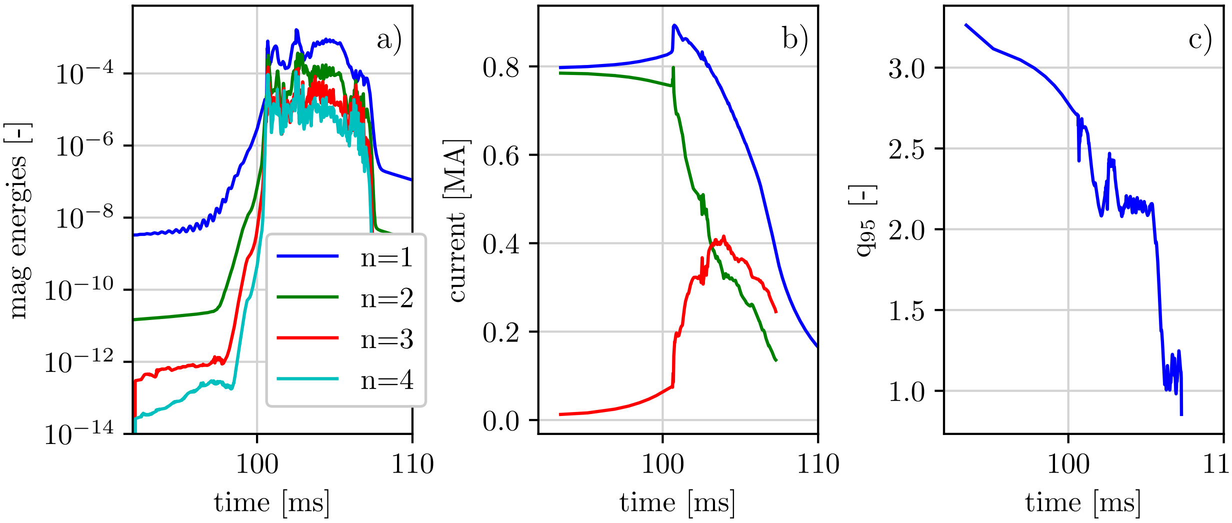

Figure IV.10: The evolution of the a) magnetic energies (n=1-4), b) the plasma current and c) q_{95}. b) The current is subdivided into the total I_p (blue), the toroidal current inside (green) and outside (red) the LCFS. The evolution is shown here for $T_{\mathrm{min},\chi_\parallel} = 40\,\mathrm{eV}$

Crash dynamics Figure IV.11 provides a closer look on the crash dynamics for VDE simulations with different limits on the parallel heat diffusivity $T_{\mathrm{min},\chi_\parallel}$ ranging from 20 to 40 eV. A smaller heat flux to the boundary ($T_{\mathrm{min},\chi_\parallel} = 20\,\mathrm{eV}$) leads to an overall slower evolution of the CQ. The limit on q_{95} is imposed by secondary reconnection events at $t = 103.8\,\mathrm{ms}$ and $t = 106.1\,\mathrm{ms}$ that reduce the central temperature and flatten the current profile. Therefore, also the q-profile becomes flat as shown on the right column of the same figure. These Global Reconnection Events (GREs) redistribute the current beyond the LCFS similar to the TQ.

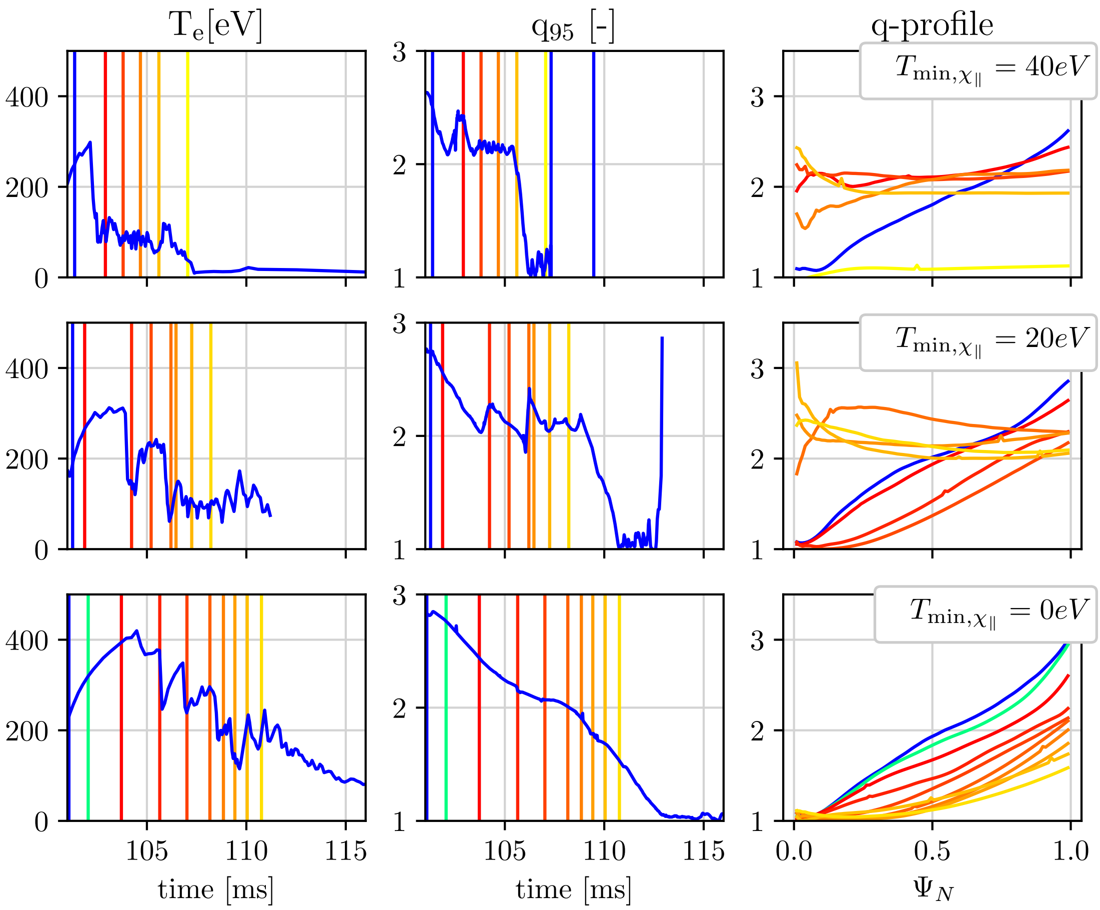

Figure IV.11: Crash evolution for a $T_{\min,\chi_\parallel}$ of 0 eV, 20 eV and 40 eV: The evolution of the central temperature (left), q$_{95}$ (middle) and the q-profile (right) is shown. The vertical lines in the second row mark the time points of the q-profile reconstruction. A larger heat flux leads to a faster evolution of the VDE.

After the GRE, the flux surfaces in the core can reform and the plasma reheats as shown in figure IV.11 a). Only after the current inside the core $I_{p,\text{core}}$ has decayed significantly, q$_{95}$ reduces to 1. $I_{p,\text{core}}$ is at around 25 to 30 % of the initial I_p when q$_{95}$ drops below the threshold.

With a larger parallel heat conduction ($T_{\min,\chi_\parallel} = 40$ eV) and therefore a colder SOL, q$_{95}$ is still limited to values around 2, while the dynamics are slightly faster. Like in the 2D simulations, the movement is accelerated by the colder SOL that suppresses halo currents, leading to a faster scraping off of the edge plasma. Moreover, the flux surfaces remain open during the CQ phase and inhibit the reheating of the plasma center in this case. Instead of several large crashes, q$_{95}$ oscillates around the threshold value until I_p decreased significantly and the core plasma becomes small. When the evolution is slower, the profile relaxation is more violent and less frequent (IV.11 (middle)), while in the cases with larger $T_{\min,\chi_\parallel}$ the relaxation is more continuous and the plasma stays close to the stability boundary (IV.11 (top)).

Under certain circumstances, a q$_{95}$ value of less than 2 can be reached as for the case with $T_{\min,\chi_\parallel} = 0$ eV shown in figure IV.11. In this simulation, $I_{p,\text{core}}$ is larger when q$_{95}$ decreases below 2 with 50 % of the initial I_p. In the following, an analysis of two similar cases with and without GRE are investigated in more detail.

Trigger of the global reconnection event In most simulations, a global reconnection event (GRE) occurs during the CQ phase, limiting q$_{95}$ to around 2 until $I_{p,\mathrm{core}}$ decreases significantly to around 25 % of $I_{p,0}$. However, some exceptions without a GRE exist, allowing q$_{95}$ to decrease while $I_{p,\mathrm{core}}$ is still at around 50 % of $I_{p,0}$. Only when q$_{95}$ reaches a value of around 1, MHD activity sets in to prevent a further drop.

Two simulations are analyzed in more detail. These two cases have a $T_{\mathrm{min},\chi_\parallel}$ of 0 eV and originate from the same simulation. The main difference between them is that the boundary conditions for ρ is adjusted to $\boldsymbol{\nabla}\rho \cdot \mathbf{n} = 0$ at different points in time. This was done to prevent a loss of density along open field lines during the disruption. The BC is applied either before or after the TQ, leading to a ρ two times smaller in the latter case. While a GRE occurs in the larger ρ simulation, there is only local reconnection in the second case. Therefore, they are labeled *Crash* (larger ρ) and *No Crash* (smaller ρ) in the following.

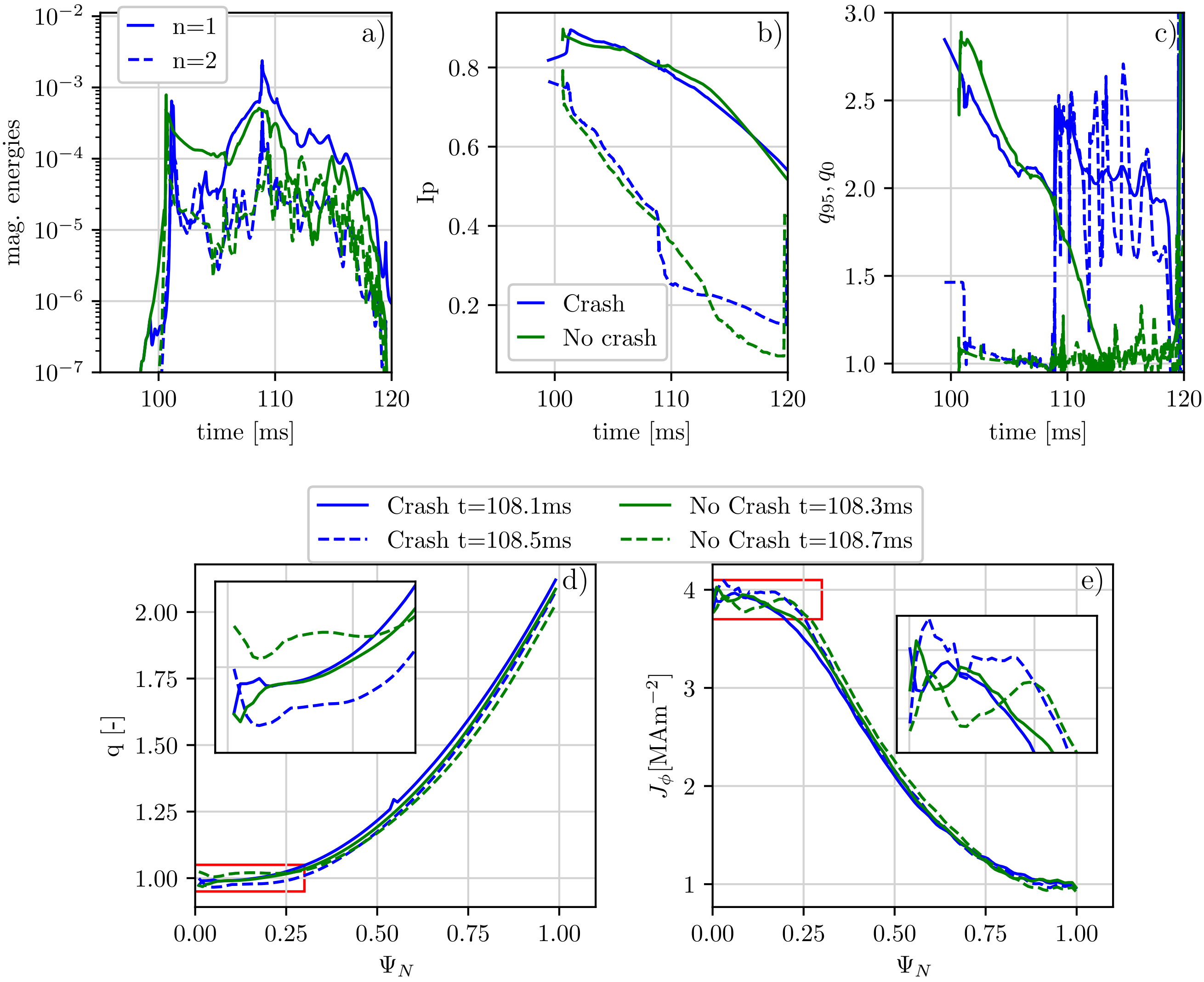

Figure IV.12: The first row shows the time evolution of a) the magnetic $n = 1$ and $n = 2$ energies, b) I_p (solid) and $I_{p,\mathrm{core}}$ (dashed) as well as c) q$_{95}$ and q_0 for the cases *Crash* and *No Crash*. The second row illustrates the q-profile and the flux-surface averaged $n = 0$ current density for two time points close to the reconnection event of *Crash*. The boxes represent the zoom into the red rectangle.

The time evolution of these simulations and their flux surface averaged profiles are illustrated in figure IV.12. The magnetic energy behaves differently despite the similar evolution of the total I_p, $I_{p,\text{core}}$, and the q-profiles. After the TQ, the energies of *No Crash* remain larger, while the non-axisymmetric contribution of *Crash* decays. Also, the temperature profile (not shown here) is comparable but evolves dynamically in both cases. In both simulations, the temperature increases after the TQ after flux surfaces reform due to Ohmic heating, and the vertical displacement continues after the TQ, further decreasing q_{95} as shown in figure IV.12 c). Simultaneously, $I_{p,\text{core}}$ decreases as the outer layers are scraped off. The core is more resistive compared to the pre-TQ plasma, inhibiting a re-induction. When q_{95} reaches a value of around 2, a GRE occurs in *Crash* at around 108.8 ms.

Investigating the profiles close to this event should help to understand the different evolution. However, the q and current density profile depicted in figure IV.12 d) and e) are almost identical. Nevertheless, we note that the q value on the magnetic axis is slightly below 1 in both cases. While the volume where q is close to 1 might seem small in figure IV.12 d), it encompasses around half of the core. Just a few hundreds of µs before the GRE would occur, the current profile in *No Crash* relaxes slightly in the core, pushing q_0 to a value above 1.

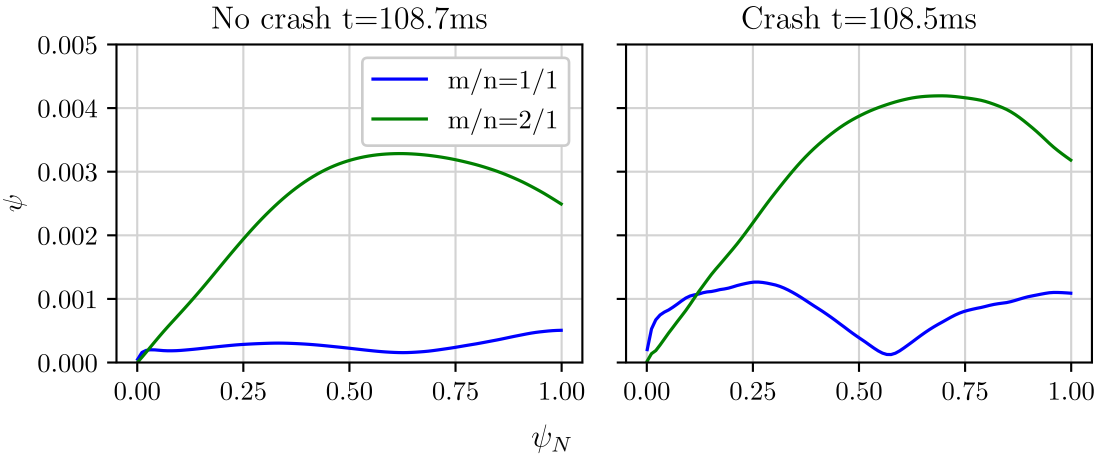

Figure IV.13: The $m/n = 2/1$ and $m/2 = 1/1$ contribution to ψ is shown for *Crash* and *No Crash* shortly before the GRE occurs. Only in the case of the *Crash*, a 1/1 mode in the core is present.

Furthermore, a Fourier analysis presented in figure IV.13 of the $n = 1$ perturbation of ψ shows that *Crash* has a larger $m = 1$ mode in the core as well as a $m = 2$ at the edge. On the other hand, the $m/n = 1/1$ mode is not present for *No Crash*. An investigation of the other cases without GRE shows that none has an $q = 1$ surface in the core. Thus, an interaction between a 2/1 and 1/1 seems to be essential for the GRE. While no GRE exists in *No Crash*, it still shows strong MHD activity and reconnection events occur inside the core. However, they are not violent enough redistribute the current outside the core.

As stated before, *Crash* and *No Crash* only differ in the time points when the boundary conditions were changed, but are otherwise very similar. By comparing the profiles shortly before the GRE, it is apparent how sensitive the dynamics are, where a small relaxation in the core prevented the GRE in *No Crash*. However, due to the non-linear nature of the system, a prediction of the evolution remains difficult.

Global comparison to the experiment Finally, the overall evolution is compared to the experiment in figure IV.14, where the dependence of the CQ duration with the heat flux becomes apparent. The best match is obtained for a $T_{\min,\chi_\parallel}$ of 80 eV, where the CQ rate and waveform match well.

Despite the different evolution time scales, the magnitude of the halo currents is comparable, and therefore, largely independent of $T_{\min,\chi_\parallel}$. Also, the TPF does not vary significantly except for the case with $T_{\min,\chi_\parallel} = 0\,\text{eV}$, which shows a lower TPF. When comparing the TPF at the time of the maximum I_h, the values in JOREK are around 1.2, which is lower than the experimental value of 1.5. However, the time evolution of the TPF behaves very dynamically in the experiment as well as in the simulation. When the whole CQ duration is considered, the TPFs are in a comparable range to the experiment. Note also that the spikes in the halo current in the simulation are more pronounced as the quantity is not averaged over the inner and outer side of the divertor like in the experiment (see eq. (II.25)), but calculated according to equation (II.19), so that small scale fluctuations contribute to I_h.

After comparing the overall dynamics, we are going to have a closer look on the halo currents and forces in the following sections.

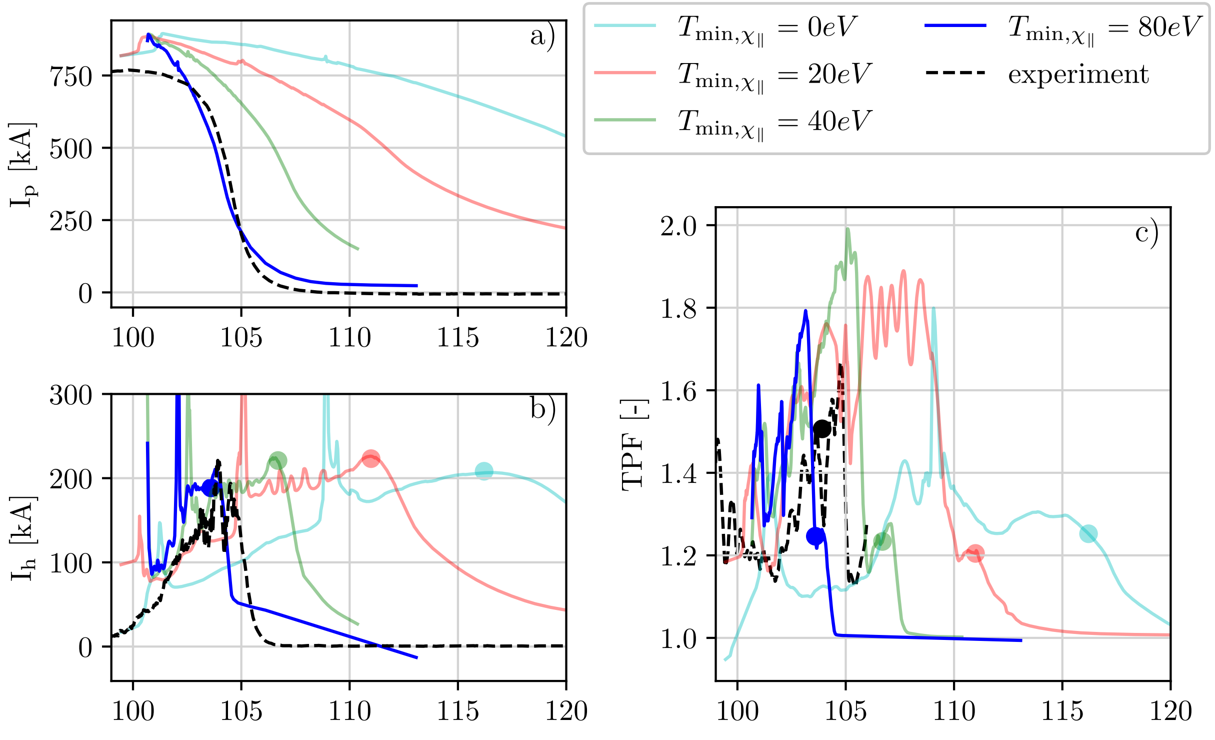

Figure IV.14: The evolution of the a) plasma current, b) poloidal halo current and the toroidal peaking factor of I_h are compared to the experimental time traces with good match for comparable boundary heat fluxes. The maximum of I_h and the TPF at that time are indicated by a circle.

IV.3.3 Halo currents

In the following, we are going to have a closer look at the halo currents. While the magnitude of the halo currents is comparable to the experiment, the 2D simulations described in section IV.2 showed a larger halo current width. The same is true for the non-axisymmetric simulation results illustrated in figure IV.15. However, the halo width decreases with larger $T_{\mathrm{min},\chi_\parallel}$ as the SOL resistivity becomes larger compared to the one in the relatively hot core. In the simulation with $T_{\mathrm{min},\chi_\parallel} = 80\,\mathrm{eV}$, the halo width is comparable to the experiment, which is also the case with the best overall match according to figure IV.14. Sheath boundary conditions required to capture the evolution in the SOL self-consistently are not considered here.

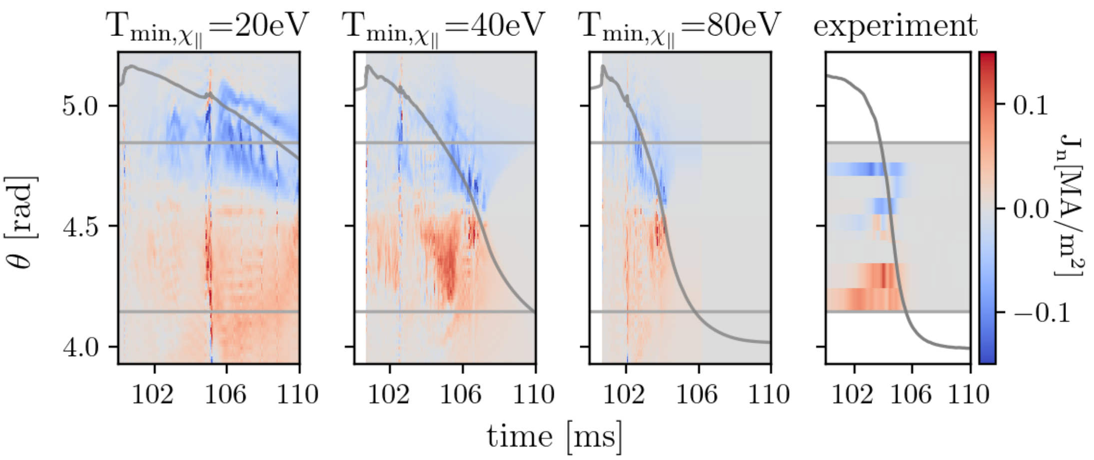

Figure IV.15: The radial width of the halo region for different threshold values of the parallel conduction $T_{\mathrm{min},\chi_\parallel}$ in the range of 20 to 80 eV. The width decreases with $T_{\mathrm{min},\chi_\parallel}$, but is slightly larger than the experimental one. The halo current in the heat shield is not included here since it is negligible as can be seen from figure III.4

The halo current is asymmetric with a TPF in the range of 1.2 to 1.8 as shown in figure IV.14 c). The structures are strongly fluctuating during the TQ phase, during which the plasma reconnects and the current flattens beyond the LCFS. In the simulation, this is results in the I_h spikes in figure IV.14 b) and the large current densities in figure IV.15 at $t = 105\,\mathrm{ms}$ in the left most panel. This phase is not as pronounced in the experimental shunt measurements because the fluctuations average over the spatial extent of the tiles. However, the localized Langmuir probe measurements can capture them (not shown here).

Figure IV.16 displays the 2D pattern of the current density normal to the boundary of the computational domain in JOREK at different time points during the evolution of the VDE for the simulation with $T_{\mathrm{min},\chi_\parallel} = 20\,\mathrm{eV}$. During the TQ phase, there are small scale fluctuations that later evolve into an $n = 1$ pattern lasting over the majority of the CQ. At the time of the larger crashes, a secondary I_p spike occurs as visible on the left of figure IV.16.

After the LCFS is lost, the $n = 1$ pattern vanishes and the halo current is more axisymmetric (not shown). In the same figure, it becomes apparent that the halo current does not rotate as the pattern remains stationary after an initial stage of slow rotation in between 101.52 to 106.36 ms. Figure IV.16, where the ϕ position of the maximum I_h is shown, confirms this

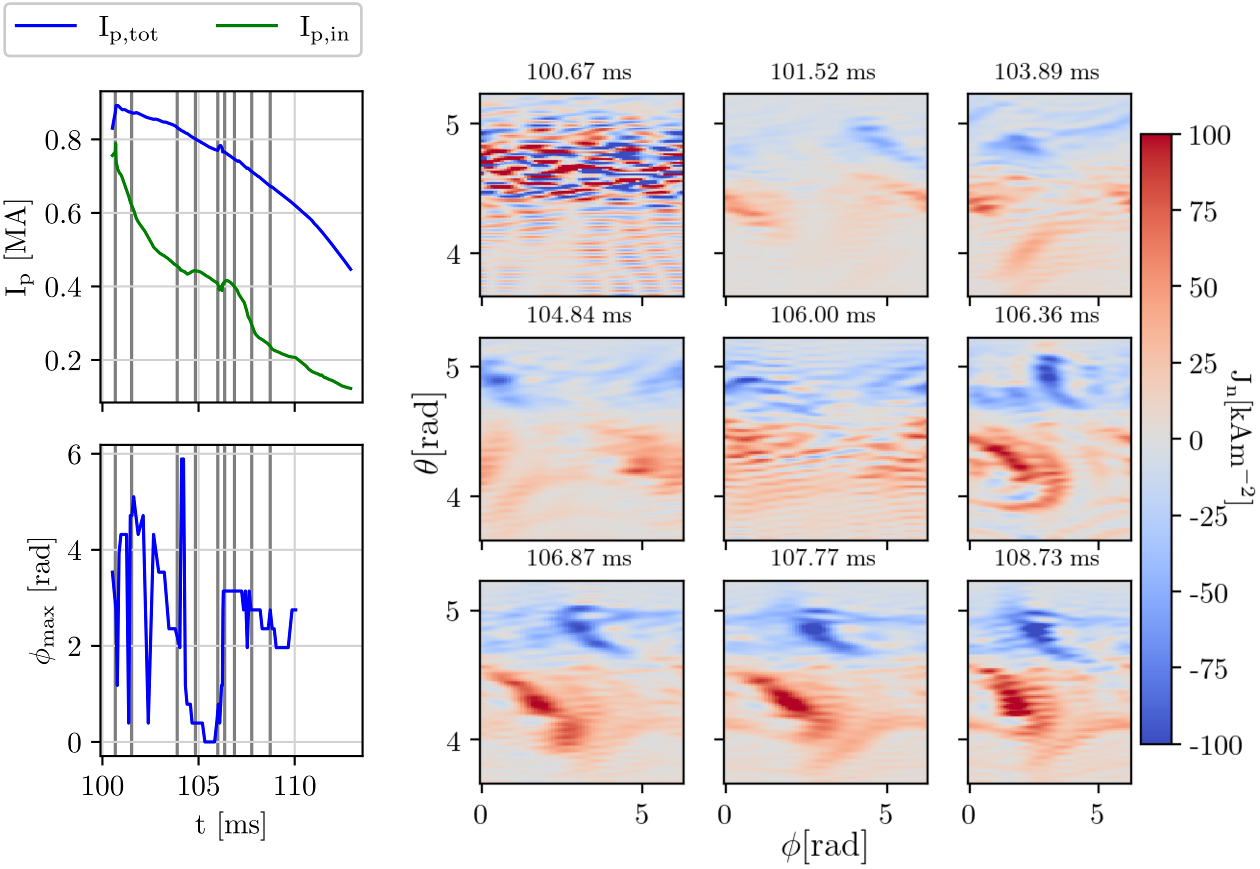

Figure IV.16: The normal current to the boundary strongly fluctuates during current redistribution in the TQ phase, while an $n = 1$ pattern dominates during the CQ. On the left, the total I_p, the I_p inside the LCFS as well as the toroidal position of the maximum I_h are shown as reference, where the time slices shown on the right are marked with vertical lines. The results shown here correspond to the case of $T_{\min,\chi_\parallel} = 20\,\mathrm{eV}$ as a representative example.

intuition. This does not disagree with the experimental results, where there is no direct sign of rotation. However, it is possible that realistic BC are required to capture rotation self-consistently [Pfe18].

IV.3.4 Forces

The vertical forces behave similar to the 2D VDE simulations shown in section IV.6, where the magnitude of the force varies with the CQ duration. In the following, we are going to analyze the origins of the EM loads in more detail. The forces are computed with equation (IV.3), where moving the integration surface allows to evaluate the forces **F** acting on different components. Usually, the surface is chosen to be slightly outside the vacuum vessel (VV) to obtain the net global force on the system comprised of the plasma, in-vessel coils and the VV itself. In turn, positioning it just outside the plasma allows to isolate the halo current contribution, while a location inside the vacuum vessel provides information about the PSL and halo current force combined. Thus, in order to obtain the contribution from the eddy currents in the wall, the latter has to be subtracted from the total force:

$$F_{w,X} = F_{\mathrm{tot,X}} - F_{\mathrm{PSL+halo,X}}, \tag{IV.4}$$

where X signifies the direction on which $\mathbf{F}$ is projected.

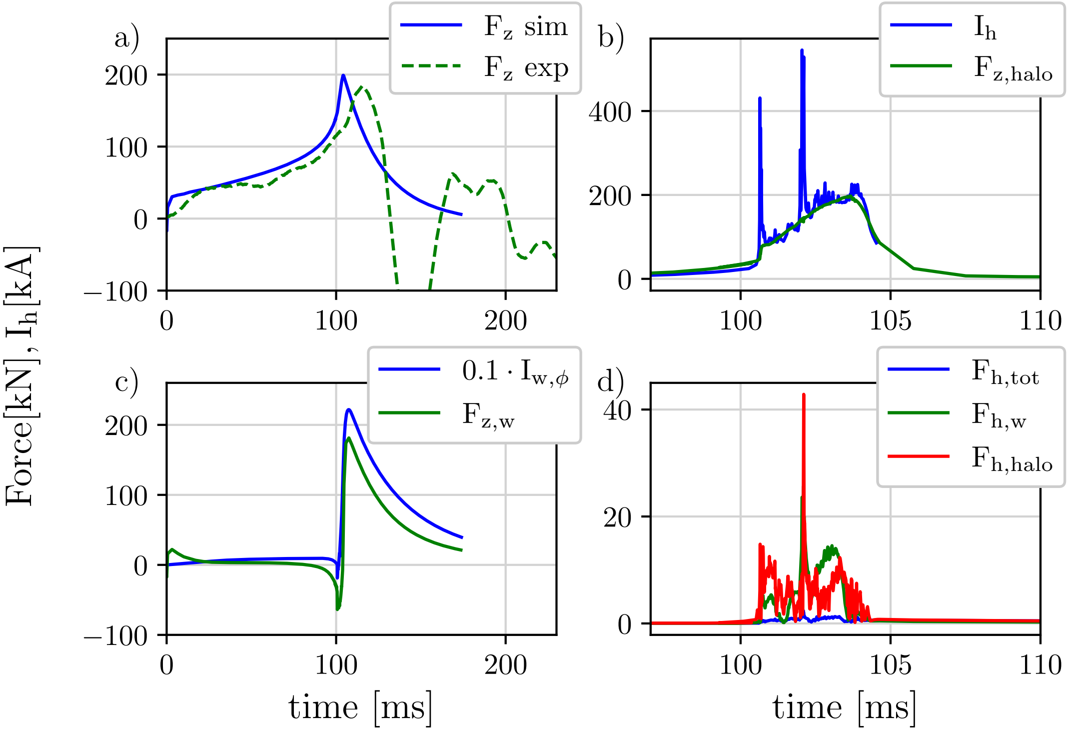

Figure IV.17: a) The global vertical force is compared to the experimental one; the b) halo current contribution is proportional to the net poloidal halo current. c) The vertical force contribution from the eddy currents in the wall is related to the net toroidal current. d) The small total horizontal forces result from a near cancellation of the halo current contribution and the eddy currents. Note the different time scales of the left and right column.

The different components of the forces are depicted in figure IV.17, where the case with $T_{\mathrm{min},\chi_\parallel} = 80\,\mathrm{eV}$ was analyzed since its τ_{CQ} is similar to the experimental value. Regarding the magnitude of the total vertical force, the result is again in the same order as in the experiment and evolves on a faster time scale as the elasticity of the vacuum vessel is not taken into account in the system. The different contributions of the force give further insight on the forces.

The halo current contribution is important for hot VDEs as large halo fractions occur during these events, so that they are responsible for almost the total F_z as shown in figure IV.17 b). The maximum of $F_{z,\mathrm{halo}}$ is around 200 kN, so that they have the largest contribution to the force at the time of the maximum I_h. It is also apparent that the force from the halo current is proportional to the poloidal halo currents I_h that intersect with the computational boundary. As pointed out before, the spikes in I_h originate from small scale fluctuations that do not contribute to the net halo current that flows between the divertor regions separated by the contact point, so that they do not contribute to the force. A benchmark of 3D VDEs between the reduced MHD codes JOREK and the full MHD codes MCD-C1 and NIMROD [Art21a] indicated a good correspondence between the models despite the fact that $\mathbf{J}_\theta$ is reconstructed from the force balance condition in JOREK and the closing path through the computational boundary not being explicitly contained in the model. Here, the relationship of I_h and $F_{z,\text{halo}}$ provides additional confidence in the reduced MHD model.

The contribution from eddy currents in the vacuum vessel F_w is illustrated in figure IV.17 c), where the net toroidal wall current $I_{w,\phi}$ is related to the force contribution of the vacuum vessel. During the downward displacement phase of the VDE at the time 0 to 100 ms, the force from the eddy currents is positive to counteract the plasma motion. Then, the induced eddy currents during the I_p spike reverse the sign of F_w. In the phase leading up to the TQ, the PSL contribution to F_z is the largest.

In the CQ phase, the net toroidal current in the wall becomes positive again and so does the vertical force contribution of F_w. The decay times of the force and net current is determined by the resistive wall time and the interaction with the PSL. In contrast to the experiment, the PSL in our model cannot carry a net toroidal current, so that the contribution to the force will be different than in the experiment in later stages of the current quench when such a current is present.

It was shown in [Cla19] and will be pointed out in section IV.4 that the halo currents alone are not a meaningful measure for the force. In the indicated reference, the halo currents were artificially suppressed, while the global force remained the same because the eddy current contribution compensated for the smaller $F_{\text{z,halo}}$. Instead, the magnitude in a hot VDE is determined by the displacement of the plasma and the shielding efficiency of the vacuum vessel as discussed in section II.3.4. This is a consequence of the force free condition of the plasma.

While the horizontal force in the experiment cannot be estimated directly, the small horizontal displacements of the vacuum vessel suggest the absence of a one of significant amplitude. Also the horizontal force $\sqrt{F_x^2 + F_y^2}$ in the simulation is negligible as shown in figure IV.17 d), with a factor of ≈100 smaller compared to the vertical component. This value is negligible and can be influenced by errors from the integration. The horizontal contributions from the eddy currents in the VV and the halo currents have larger magnitudes, but cancel each other almost completely.

The total sideways impulse during the disruption only accumulates to a value of 17 N s, which is 10 times smaller than the one estimated for AUG [Pau11]. However, it has to be noted that the current sharing between the vacuum vessel and the plasma seems to be the key ingredient of the horizontal force in JET as pointed out in section II.3.4. Since this is not included in our model that does not allow for a toroidally asymmetric plasma current, it is not possible to reproduce the significant horizontal force observed in JET at the moment [Art23]. While the TPF of the halo current is comparable to the experiment in AUG, a large 1/1 kink mode and the sharing of current is required for a substantial horizontal force [Ric09]. This absence can be explained by the q_{95} limit observed in most of the simulations, eliminating an external 1/1 kink mode.

IV.3.5 Summary of 3D hot VDE simulations

The simulations of the non-axisymmetric phase of hot VDEs proved that JOREK-STARWALL is an appropriate tool for investigating their dynamics. It is possible to reproduce key quantities like the TQ onset point due to low-n kink modes, the magnitude of I_h and its TPF as well as the vertical force magnitude. Similar to the 2D hot VDE simulations, the boundary conditions are essential for the evolution during the CQ phase. Setting a reasonable value of the heat flux allows to obtain a comparable τ_{CQ} and halo width to the experimental results.

While the TQ phase is typically challenging to model, it was possible to reproduce the expected τ_{TQ}. However, the simulations of the CQ phase are computationally at least as expensive due to the rich MHD activity. This imposed a q_{95} limit on the plasma in the majority of simulations, most likely linked to a coupling of an external kink and an 1/1 internal mode. The consequence is a global reconnection event that redistributes the current beyond the LCFS similar to what happens during the TQ phase. As the plasma behaves strongly non-linearly, it is not possible to predict this evolution without trustworthy simulations. If the q_{95} limit also occurs in reality in AUG, it could explain the absence of a substantial horizontal force because the responsible 1/1 kink mode is not accessible at large currents.

An analysis of the force contributions showed that the sources vary in the different phases of a hot VDE. At the beginning, the currents in the PSL contribute the most, while in the CQ phase the halo currents become more relevant. However, it will be pointed out in the following section that the magnitude of the global force only depends on the plasma movement in case the wall shielding is negligible.

The heat loads during a hot VDE can cause premature material aging in high energy devices and the risk of horizontal forces make a mitigation system mandatory. The mechanism of the force mitigation is the subject of the following section.

IV.4 Simulations of SPI mitigated VDEs

The experiments of SPI mitigated VDEs in ASDEX Upgrade were described in section III.2. Their results showed that the vertical forces can be reduced significantly with earlier injection, which is one of the reasons this technique is widely employed and foreseen in future high-current machines. However, the mechanism responsible for this reduction introduced in section II.3.5 has yet to be described in detail in the literature.

It is based on the fact, that the displacement of the current centroid, responsible for the largest vertical forces, can be reduced by a broad halo region in radiation dominated disruptions. This keeps the geometric center of the current distribution closer to the midplane and thus reduces the force. The goal of the simulation study presented in [Sch23b] was to further understand this mechanism and investigate the influence of the boundary conditions as well as conductive wall effects. Furthermore, the results were compared to the experiment, providing compelling evidence in support of the theory. Besides the AUG results, the manuscript [Sch23b] contains further simulations for JET and ITER performed by J. Artola and F. Vannini. Only the AUG results obtained as part of this thesis are detailed in the following as a representative example if not stated otherwise.

This section is organized as follows: First, the simulation setup is described in section IV.4.1, before the influence of the halo temperature on the VDE evolution and halo width are investigated in section IV.4.2 and IV.4.3 respectively. Afterwards, the mitigation efficiency for different injection times is presented in section IV.4.4, and the importance of the conductive wall properties for the force reduction is shown in section IV.4.5. Finally, a study on the injection of different quantities of Neon is carried in section IV.4.6.

IV.4.1 Simulation Setup

Due to their reconnective nature, disruptions are inherently non-axisymmetric events and especially the realistic modeling of SPI shards requires a high resolution, a physical model of the shard ablation, as well as the behavior of the cold plasmoid [Hu18]. However, when applying certain restrictions as described in IV.2, 2D simulations can be useful to estimate axisymmetric loads, CQ times, radiation fractions, VDE trajectories, etc. As we are interested mainly in the axisymmetric toroidal halo currents and vertical forces for this study, 2D simulations are sufficient to draw conclusions and study the relevant effects.

The simulation setup is based on the previous work in JOREK (unpublished), where a fluid impurity model with the coronal equilibrium assumption is employed for 2D simulations to study the VDE behavior in the presence of impurities. Furthermore, the most of the simulations presented here are based on the SPI mitigated discharges described in section III.2.

The simulation is performed in 5 phases as detailed in the following:

1. A VDE is triggered like for the hot VDEs described in section IV.2 and the plasma initially displaces the same way.
2. At a specific time corresponding to the TQ in the experiment, the perpendicular heat diffusivity is set to a constant value 100 times higher than the initial value in the core.

3. After the temperature decreases to 10 eV, the second phase of the TQ is initiated by increasing the hyper-resistivity η_{hyp} to flatten the current profile. Its value is chosen to match the I_p spike in the experiment.
4. Finally, Neon is introduced by a uniform impurity density source during a short time as the pellet in the experiment consisted of 100 % Neon. The amount of impurities is adapted to fit the initial current quench rate in the experiment. Note that, in reality, the impurities would trigger the TQ by radiatively cooling the edge and thus triggering instabilities. We are mainly interested in the CQ phase, so the order was switched to simplify the simulation.
5. The last phase consists of the CQ, where the parameters are reset to realistic values with a $\chi_\perp$ of $2\,\mathrm{m}^2\,\mathrm{s}^{-1}$, $\chi_\parallel = \chi_{\parallel,\text{S-H}}(T)$ and $\eta_{hyp} = 0$, which are comparable to the pre-TQ values.

As it was shown in section IV.2, the boundary conditions are not self-consistent, and can influence the VDE evolution. In the case of radiation dominated disruptions like obtained by mitigation with impurities, the heat flux is expected to be less important than for hot VDEs, where the boundary heat flux is the main loss channel for the energy. Therefore, we want to assess the importance of the heat flux for the SPI mitigated VDEs in the following section. Two different methods described below are employed to estimate the importance of the boundary heat flux. This treatment allows us to investigate the influence of the halo temperature, however, not of the halo width independently.

Both are essential for the theory presented in section II.3.5. In the following, we first study the influence of the halo temperature and width separately for one injection time before summarizing the results for distinct injection times.

IV.4.2 Influence of the halo temperature

In this section, the injection time is based on shot # 40955, where the TQ took place at around 3.015 s, which is 45 ms after the VDE start taken as $t = 0$ in the simulation. The results for the other injection times are presented in section IV.4.4.

Variation of $T_{\mathrm{min},\chi_\parallel}$ First, a minimum threshold of the parallel heat diffusivity according to equation (IV.2) is imposed as described in section IV.1. The equilibrium is based on # 39655, which was analyzed in detail in IV.2, where the downward VDE is induced similarly by a forced displacement by the control coils.

Figure IV.18 a) shows the evolution of the vertical and radial current centroid position, the plasma current evolution, q_{95} and $I_p\Delta Z_{\mathrm{curr}}$ with time. Here, ΔZ_{curr} signifies the vertical displacement of the current centroid as defined in (II.24) from its equilibrium position, and $I_p\Delta Z_{\mathrm{curr}}$ is related to the vertical force according to the theory in section II.3.5.

At the triggering time of the TQ at 45 ms, the current centroid moves rapidly downward for 1 ms due to the dragging effect [Nak02] caused by I_p spike induced eddy currents in the VV. In 2D simulations, the current spike is mimicked artificially by increasing η_{hyp}, which leads to a flattening of the current profile. The parameter is chosen such that the magnitude of

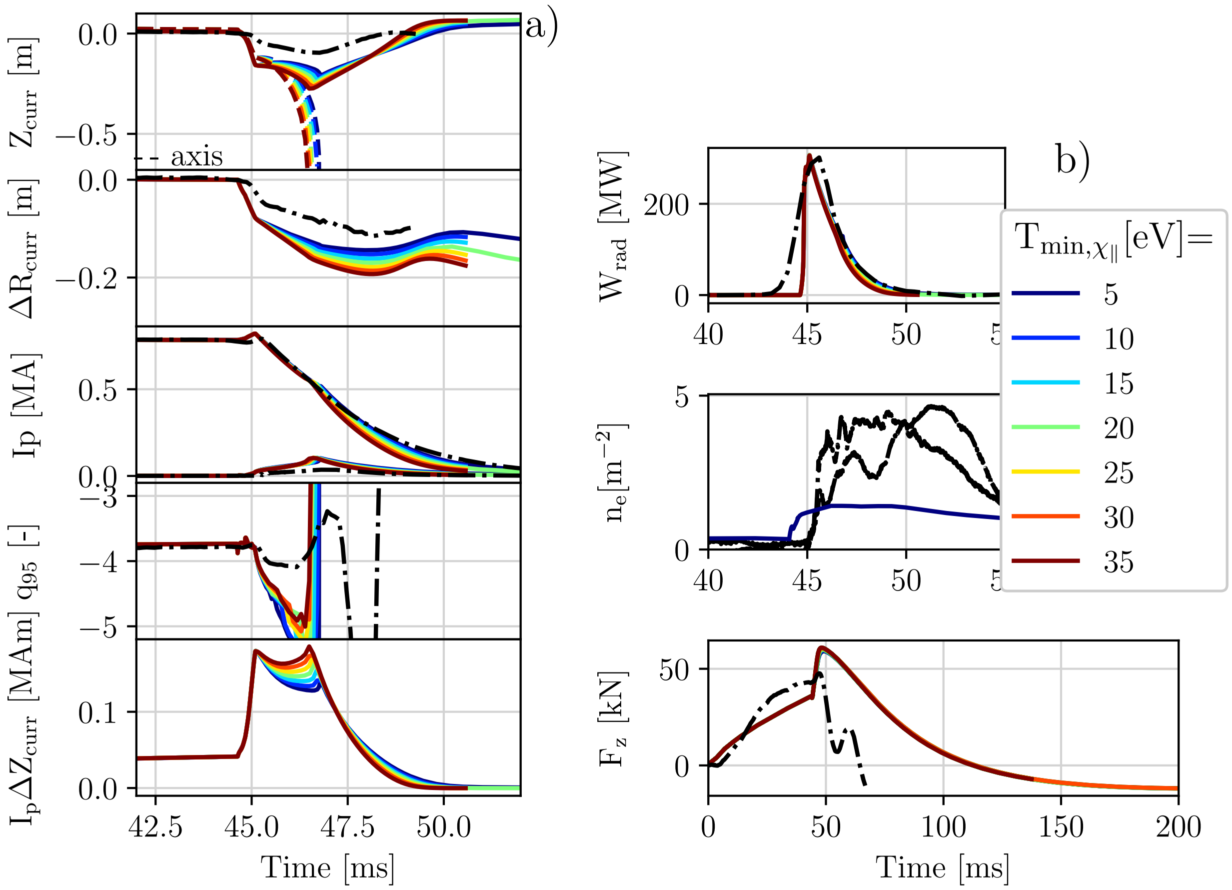

Figure IV.18: Overview of the AUG results of the parallel heat conductivity scan: a) From top to bottom: the vertical current centroid position, its radial displacement, the plasma current and poloidal halo evolution, q_{95} and $I_p\Delta Z_{\text{curr}}$ are shown. b) The comparison of the experimental evolution of the radiation, the line integrated electron density and the vertical force are depicted. The dash-dotted line represents the experimental time traces. (Adapted from [Sch23b])

the spike matches the experiment, assuming that this will give a comparable post-TQ current distribution.

Similarly, the final impurity density of $2.3 \times 10^{19}\,\text{m}^{-3}$ is a parameter adapted to fit the initial current decay rate of the experiment. Finally, $T_{\text{min},\chi_\parallel}$ is varied from 5 to 35 eV during the CQ phase, where a small value signifies slower parallel conduction. The Z position of the current centroid in figure IV.18 (top) remains close to the midplane, while the fast CQ accelerates the magnetic axis motion represented by the dashed lines. The current centroid position matches qualitatively the experiment, which is acceptable due to the uncertainties mentioned in section II.4. This is one essential aspect for the mechanism of the force reduction of section II.3.5, which requires the current centroid stop its displacement after the TQ.

The CQ duration can be matched well in the simulation as depicted in Figure IV.18 c), where the case with the lowest value of $T_{\text{min},\chi_\parallel}$ is closest to the experiment. This indicates that radiation is the primary loss mechanism for the magnetic energy and heat fluxes to the boundary play a minor role, in contrast to the hot VDE simulations, where the heat flux is the main loss channel of the thermal energy. Due to the stationarity of Z_{curr}, the change of the current moment represented by $I_p \Delta Z_{\mathrm{curr}}$ stagnates accordingly before decreasing with the decaying I_p. Furthermore, as predicted in section II.3.4, q_{95} increases due to the fast I_p decay.

The right panel of figure IV.18 shows further comparison to the experiment, where a good match of the vertical force and radiated energy is found. However, the electron density seems to be larger in the experiment.

Variation of n_e^{wall} A second set of simulations was performed with the same setup, apart from the boundary condition of the temperature. Here, the heat flux at the boundary is directly imposed by making use of the following condition [Sta00]:

$$\mathbf{q}_n = \gamma_{sh} n_e^{\mathrm{wall}} c_s T_e \frac{\mathbf{B} \cdot \mathbf{n}}{B}, \tag{IV.5}$$

where γ_{sh} is the sheath transmission factor, n_e^{wall} the electron density at the computational boundary, $c_s = \sqrt{\gamma k_B T / m_i}$ the ion sound speed and $\mathbf{n}$ the normal to the boundary. This is a result from the plasma wall interaction theory presented in section II.2.

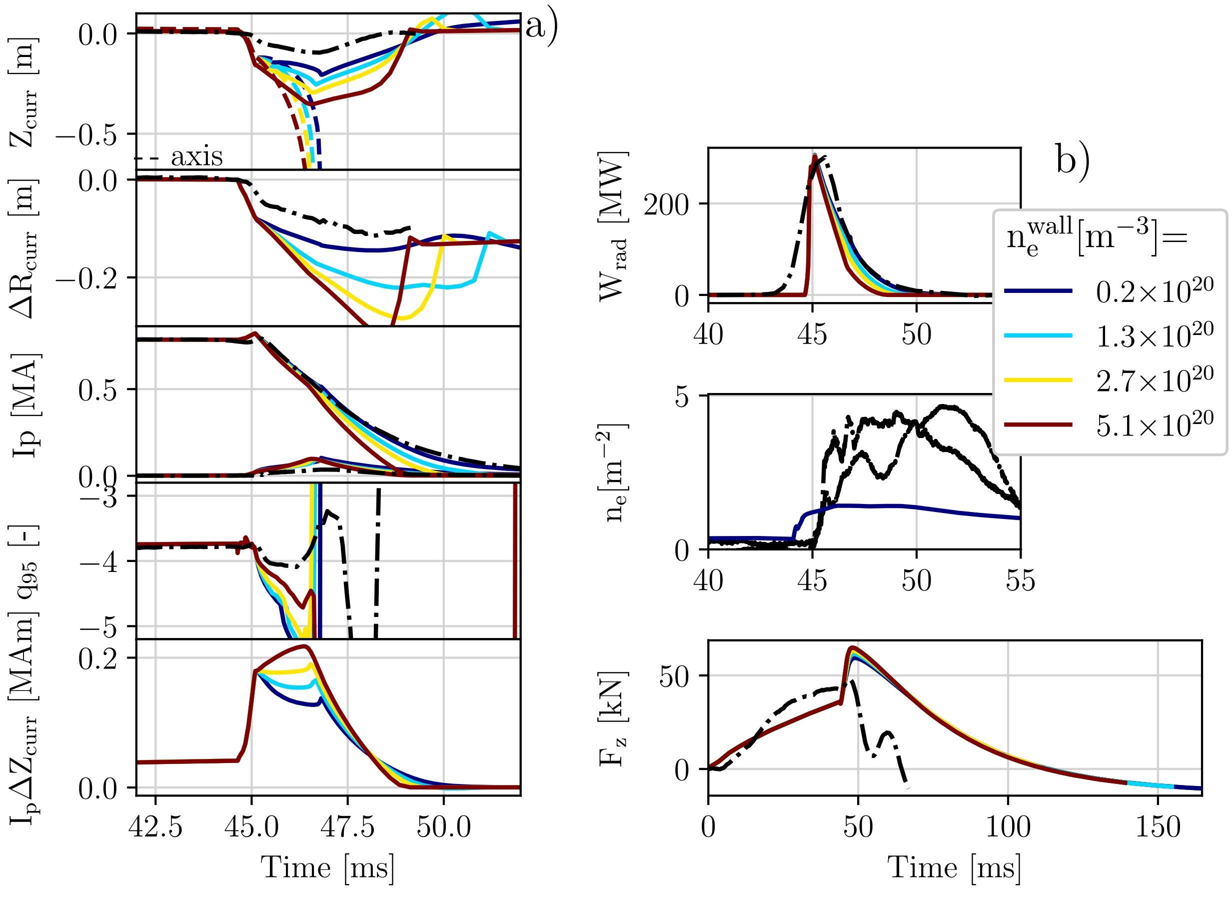

Figure IV.19: Overview of the AUG results of the boundary density scan: a) From top to bottom, the vertical current centroid position, its radial displacement, the plasma current and poloidal halo evolution, q_{95} and $I_p \Delta Z_{\mathrm{curr}}$ are shown. b) The comparison of the experimental evolution of the radiation, the line integrated electron density and the vertical force are depicted. (Adapted from [Sch23b])

While the temperature evolves according to the natural boundary condition, Dirichlet boundary conditions are still used for the density because a fully self-consistent treatment requires neutrals [Art21a] as well as sputtering. Instead, γ_{sh} is varied from its nominal value of 8 [Sta00], corresponding to a scan of the boundary density at a fixed temperature.

In this configuration, $\chi_{||}$ is set to a relatively large value corresponding to 100 eV throughout the whole domain to eliminate temperature gradients along magnetic field lines. When equation (IV.5) determines the boundary heat flux, similar results are obtained as by setting a threshold value on $\chi_{||}$ as shown in figure IV.19.

In this case, γ_{sh} was varied from 0.5 to 12 corresponding to a boundary density of 0.2 to $5.1 \times 10^{20}\,\mathrm{m}^{-3}$. The behavior of the current centroid evolution and the I_p decay time can be matched very well. Also, the peak of the radiation as well as the vertical force are close to the experimental results. Again, the case with the lowest heat conduction, corresponding to a boundary density of $0.2 \times 10^{20}\,\mathrm{m}^{-3}$ at a temperature of 4 to 5 eV would fit best with the experiment.

IV.4.3 Influence of the halo width

In the simulations of section IV.3, we saw that the halo width is overestimated in the JOREK simulations due to the applied Dirichlet boundary conditions. As a broad halo region is a necessary condition of the theory of force mitigation presented in II.3.5, the width of the SOL currents was limited by enhancing η outside a specific region. For this case, the discharge with the latest injection # 40957 is taken as a basis because the plasma is already displaced far at the time of the TQ.

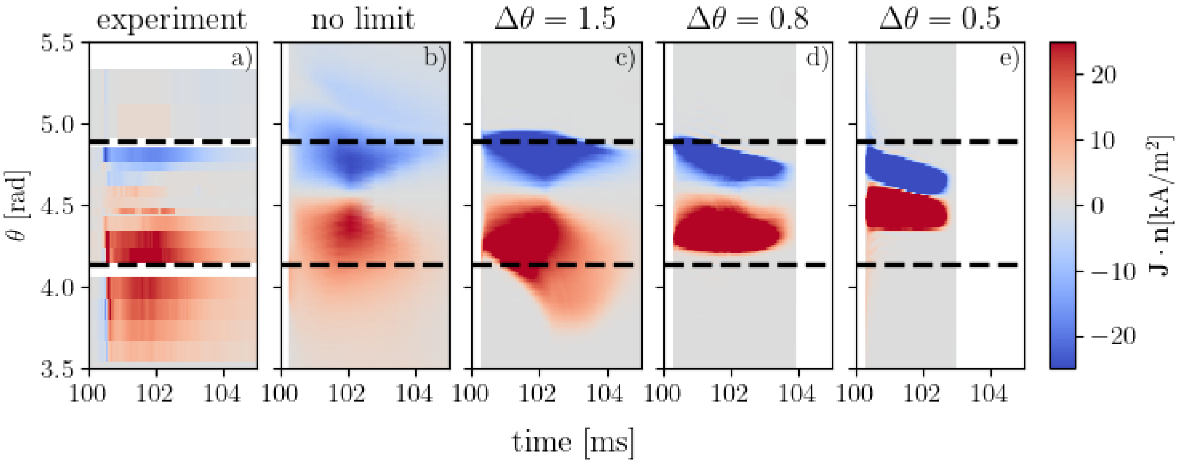

Figure IV.20: The halo width was varied by increasing η outside a region specified by θ on the boundary. The top panel shows the normal current density to the boundary from the experimental measurements as well as from the simulation without and with restricting the width. (Adapted from [Sch23b])

ψ is calculated at two points on the boundary indicated by their poloidal angle θ_1 and θ_2 defining the extent of the halo region. Now, for $\psi > \min(\psi_1, \psi_2)$, η is smoothly increased by a factor of 100 to restrict the halo region to the indicated angles as shown in figure IV.20. Three

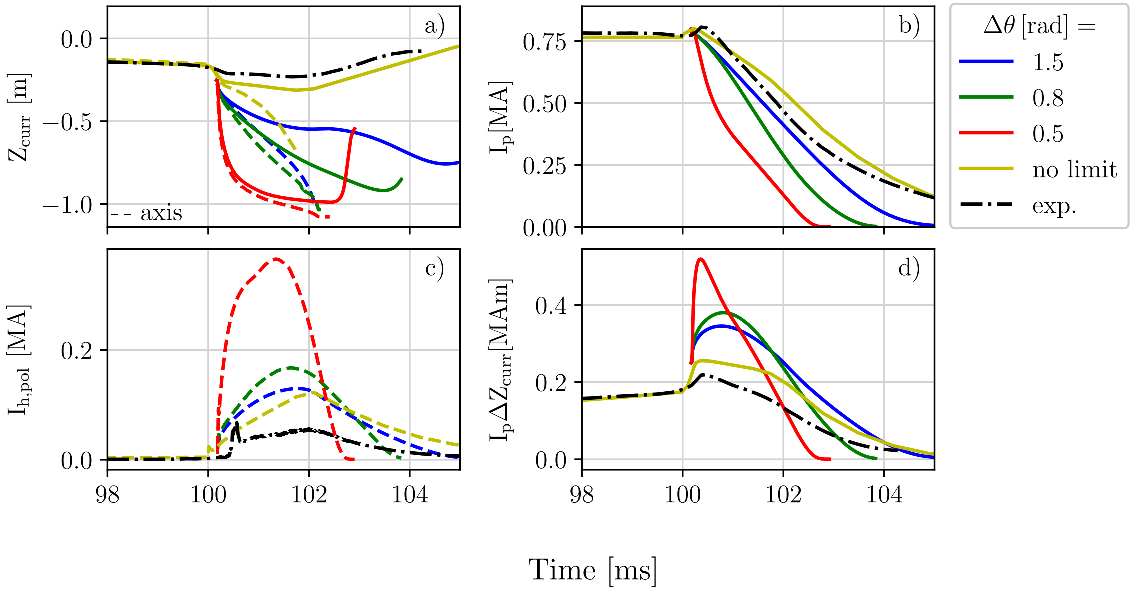

Figure IV.21: Restricting the width of the halo region changes the evolution of a) the current centroid, b) the plasma current, c) the poloidal halo currents and d) the change of the vertical current moment. The dash dotted line represents the experimental time trace. The results without width restriction are closest to the experiment. (Adapted from [Sch23b])

different extents of the halo region with a width $\Delta\theta$ of 0.5 to 1.5 rad were chosen, corresponding to approximately the location of the lower divertor edges. The results of the simulations with and without restriction as well as the experimental time traces are summarized in Figure IV.21.

When the halo width is restricted to the narrow region of the divertor, indicated by the dashed lines, or further, the geometric center of the current distribution is lower. Therefore, the current centroid moves further downward because the halo currents decay outside the specified region. This can be seen in figure IV.21 a), where the magnetic axis and current centroid move at the same rate for smaller halo widths. Also, the motion is accelerated due to the lack of stabilization by the halo currents and the CQ is faster. The same effect was already seen in section IV.2.2, where the halo region was restricted in a similar way. As q_{95} decreases due to the area decaying faster than the plasma current, the poloidal halo current increases (see IV.21 d)). Consequently, $I_p \Delta Z_{\mathrm{curr}}$ increases, and thus, also the force.

In conclusion, the plasma behaves similar to a hot VDE with the characteristic low q_{95}, the closeness between the magnetic axis and the current centroid and large poloidal halo currents when the halo width is restricted. Note that in these simulations, q_{95} was not restricted to a value of 1 by η_{hyp}, which is not realistic due to the stability limit at q_{95}=1.

These results show that a broad halo region is necessary to reduce the vertical forces on the structures, which can only be obtained by a uniform resistivity in the whole plasma region including the SOL. The halo width in the experiment shown in figure IV.20 is comparable to the case without any restrictions by η. This is another evidence that radiation is the primary loss mechanism, so that the boundary conditions only play a minor role in the presence of a large amount of impurities. Instead, the temperature is determined by the balance of Ohmic heating with radiation, which then sets the halo width by resistive current diffusion [Eid11].

IV.4.4 Injections at different times

In section IV.4.2, the simulation results of discharge # 40955 were compared to the simulations for different heat fluxes to the boundary. Now, the setup resulting in the closest match with the experiment was used as a basis for the other discharges, which is the one with a minimum parallel diffusivity corresponding to $T_{\mathrm{min},\chi_\parallel} = 5\,\mathrm{eV}$. However, additional simulations using an imposed boundary heat flux lead to equivalent results. Furthermore, a case with an injection at the initial equilibrium position and the hot VDE simulation presented in section IV.2 are added for comparison. In the following, no artificial limit on the halo width is applied.

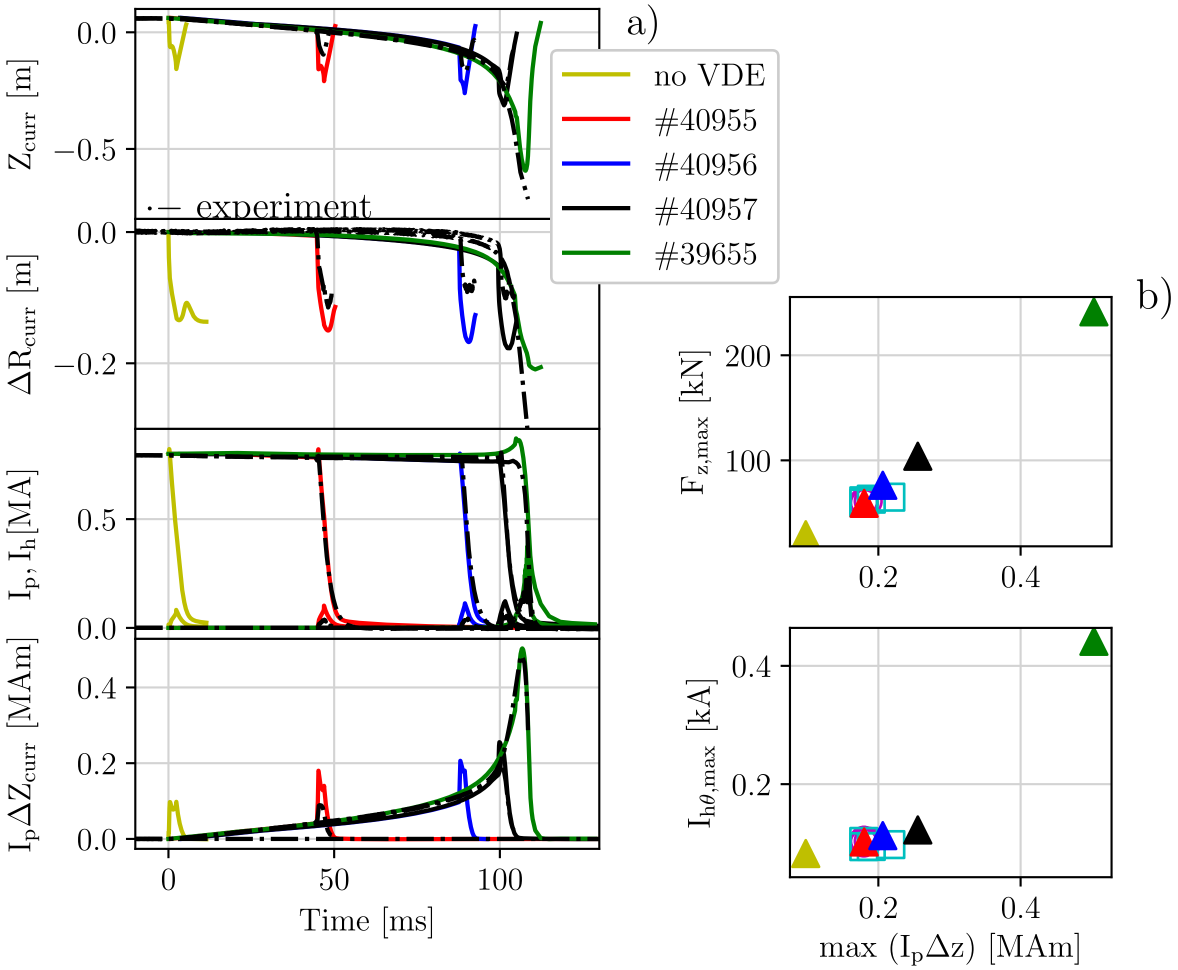

Figure IV.22: The simulations for different injection times (solid) fit well with the experimental time traces (dash-dot). It can be seen that the current centroid in the hot VDE # 39655 displaces further than the mitigated ones and the poloidal halo currents are significantly larger. (Adapted from [Sch23b])

The results summarized in figure IV.22 show a similar behavior for all the mitigated cases: After the injection, the current centroid displaces by around 10 cm downward before its motion stops. Compared to the hot VDE (# 39655), the vertical displacement as well as the poloidal halo currents are significantly smaller and the change of the current moment $I_p \Delta Z$ reduces accordingly. The plasma current decays within 5 ms in all the discharges.

The experimental time traces of the current centroid are qualitatively matched, but no quantitative comparisons are possible due to the way the measurements work. The JET results presented in [Sch23b] can be directly compared to the measurements as magnetic diagnostics remain functional during disruptions and the simulations could reproduce the experimental findings. When comparing the maximum of the force and the halo currents with the maximum of $I_p \Delta Z_{\text{curr}}$ for the discharges as done in figure IV.22 b), it can be seen that $F_{z,\max}$ is linear with $\max(I_p \Delta Z_{\text{curr}})$ and the poloidal halo currents are around four times smaller than for the hot VDE. In particular, there is no direct relationship between I_h and $F_{z,\max}$ in the mitigated disruptions.

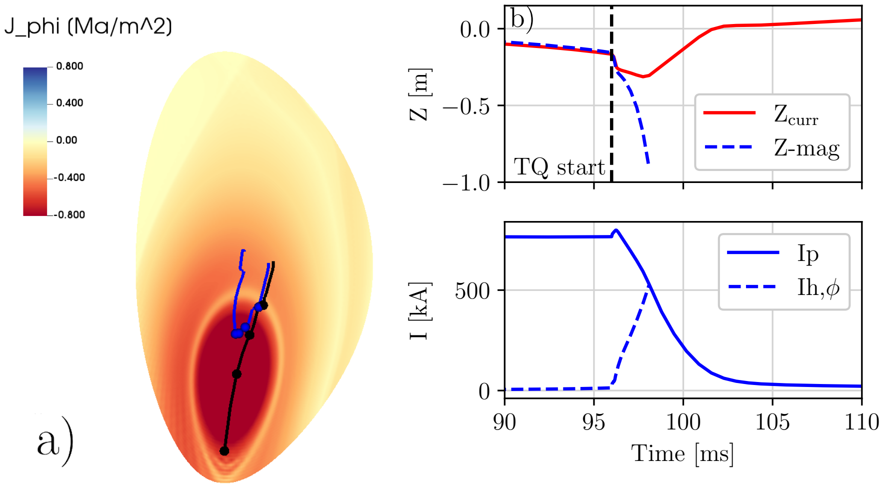

Figure IV.23: a) An illustration of the toroidal current density during the simulation of # 40957. While the magnetic axis continues to move downward with the core (black), the geometric center of the currents (blue) stays centered due to the broad halo region. b) The time evolution of the current centroid and magnetic axis are shown also on the right as well as the plasma current I_p with the contribution from the halo currents.

The relationship between the force and $I_p \Delta Z_{\text{curr}}$ proposed in section II.3.5 is found here and shown in figure IV.22 b). It was shown in this section that ΔZ_{curr} is reduced by the broad halo region, which carries a majority of the current as depicted in figure IV.23. This is only possible in the case of a flat temperature profile in the region inside the first wall, making the resistivities of the core and SOL comparable.

Therefore, we have shown that experimental and simulation results agree with the mechanism of the force reduction introduced in section II.3.5. When the essential ingredient, the broad halo width, was removed, the force is comparable to a hot VDE. Furthermore, the discrepancy between the theory predicting a fast movement of the plasma during the CQ introduced in section II.3.2 and the experiment is resolved. As the theory does not take halo currents into account, it only refers to the movement of the core, which indeed accelerates during the CQ, while the vertical centroid remains stationary. In the AUG simulations, the shielding effects of induced eddy currents in the wall is not important, which is not true for future devices like ITER that have a long resistive wall time. This is investigated in the following section based on simulations of the ITER baseline scenario carried out by F. Vannini in reference [Sch23b].

IV.4.5 Importance of the wall shielding

In the AUG simulations presented above, the shielding of the forces by wall currents does not play a role as the vessel time of a few ms is smaller than the time of the disruption with up to hundred ms. Similar reasoning applies to JET with a wall time of 5 ms [Ric04]. In contrast, the ITER wall time for anti-symmetric currents is 235 ms [Miy11], which can be slower than the duration of mitigated disruptions with early injection. Therefore, the shielding of the induced eddy currents expressed by $F_{v,c}$ in equation (II.21) becomes significant.

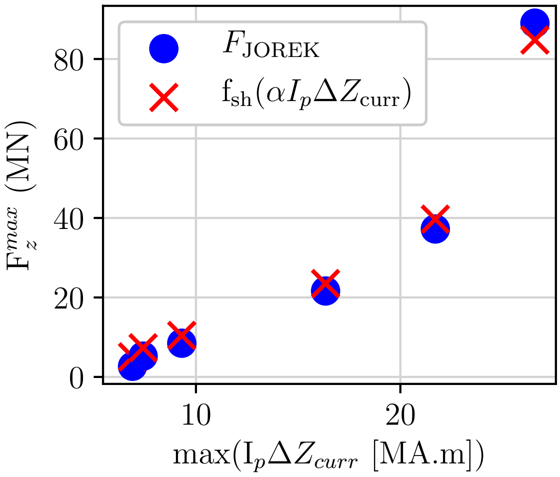

Figure IV.24: The force in ITER simulations reduces stronger than linear when decreasing $I_p\Delta Z_{\mathrm{curr}}$ as the shielding effects of the conductive structures become important. When considering them with the source term, we can theoretically predict the total force when knowing the force between the plasma and the PF coils.

As a result, the force reduces more than linear with decreasing $I_p\Delta Z_{\mathrm{curr}}$ as shown in figure IV.24. In particular, the shielding becomes more effective with earlier injection because the disruption time will become faster than the resistive wall time $\tau_{\mathrm{disruption}} \ll \tau_{L/R}$.

Taking into account the shielding of the source term $F_{p,c}$ one can recover the vertical force found in JOREK ($F_{,\mathrm{JOREK}}$) as shown in figure IV.24. The shielding is expressed by the function $f_{sh}(F_{p,c};(\tau_{L/R},\tau_{\mathrm{delay}}))$ (II.22) with the parameters $\tau_{L/R} = 235\,\mathrm{ms}$ and $\tau_{\mathrm{delay}} = 50\,\mathrm{ms}$ for ITER [Miy11],

In order to obtain this, $F_{p,c}$ is expressed by $\alpha I_p \Delta Z_{\mathrm{curr}}$, which is true to first order assuming that $\frac{\mathrm{d}B_r}{\mathrm{d}z}$ does not change significantly over the cross-section of the tokamak. The proportionality factor α can be calculated directly by the force between PF coils and plasma. Here, however, it was estimated by fitting f_{sh} to the vertical force on the vacuum vessel F_{JOREK}, using the fact that equation (II.22) is linear.

In conclusion, the force reduction can be achieved by either the shielding mechanism or by reducing the current centroid motion. In devices like ITER, both contribute to the reduction of the force as an early mitigation prevents the plasma from moving and ensures a fast disruption.

IV.4.6 On the interplay between CQ time and VDE

After investigating the vertical force and plasma behavior in a radiation dominated disruption in the first part of this section, we will discuss some aspects on the Neon quantity needed for a radiation dominated disruption. In section IV.2, we saw that the CQ duration strongly depends on the VDE growth rate as it determines how fast the core plasma current is scraped off into the cold halo region, where it decays on a faster time scale.

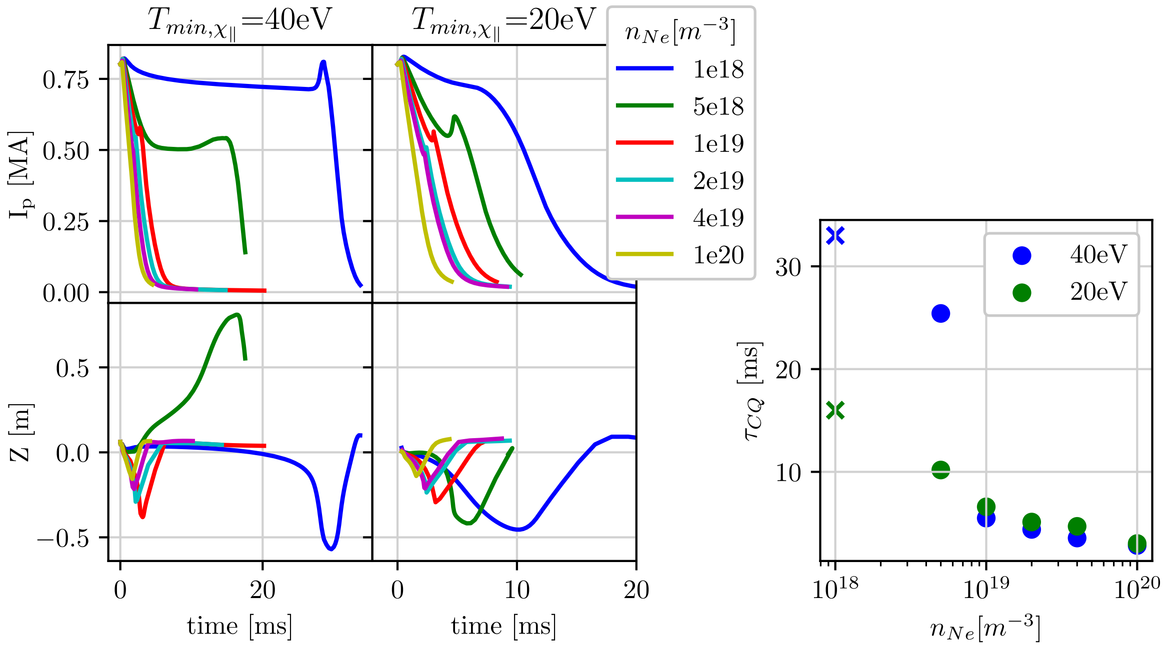

Figure IV.25: Different amounts of impurities were injected into a stationary plasma and the lower heat flux limit was varied. (Left) When the radiation is not sufficient to balance Ohmic heating, the VDE dynamics shown by Z_{curr} in the lower row determine the CQ. (Right) τ_{CQ} decreases with more impurities present. When the CQ time is mainly determined by the VDE, the time between TQ and CQ end has been taken as τ_{CQ}.

Whereas in the mitigated VDEs in this section, the τ_{CQ} is mainly determined by the post-TQ temperature and thus by the amount of impurities injected. In order to see the transition between the hot VDE like disruption and the mitigated one, different amounts of impurities were injected into a healthy plasma and the PF coils were set to a constant current. Thus, the vertical motion is initiated by the dragging effect and the I_p decay. Its direction is more likely downward, as a current flattening leads to a movement in direction to the X-point [Nak96].

In addition to the scan of n_{Ne}, two different heat fluxes were used with $T_{\text{min},\chi_\parallel}$ =20 eV and 40 eV respectively. The time evolution presented in figure IV.25 on the left shows that with more impurities injected, the CQ is faster. However, a minimum amount of n_{Ne} is required to obtain a balance with Ohmic heating. For an impurity density smaller than $1 \times 10^{19}\,\text{m}^{-3}$, the impurity radiation is not sufficient to prevent significant reheating. In these cases, the CQ is dominated by the vertical displacement, similar to hot VDEs. Most of the plasmas indeed move downward, except for one case with a n_{Ne} of $5 \times 10^{18}\,\text{m}^{-3}$ where an upward VDE occurred by chance. The current profile in this case becomes more peaked again after the TQ, as the plasma core reheats due to the low amount of impurities.

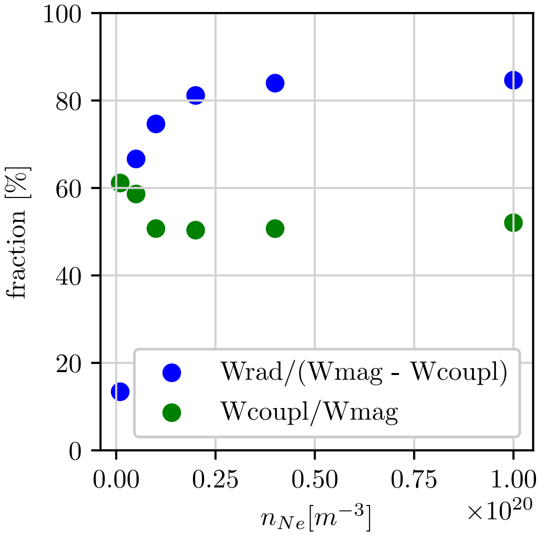

Figure IV.26: The energy coupled in the external conductors is estimated from the Ohmic heating in the plasma based on the simulations shown in figure IV.25. For fast current quenches, it is around 50 %. The radiation fraction of the magnetic energy is estimated to around 80 %

As the post-TQ state is sensitive to the amount of current flattening and the amount of impurities, these results present a simulation study rather than a detailed validation. When the radiation is not sufficient to compensate for Ohmic heating, the CQ sets in after the plasma is displaced significantly and the plasma edge is scraped off. Whereas the plasma remains closer to the midplane in the presence of many impurities. Figure IV.25 (left) shows that the larger the amount of impurities, the smaller is the excursion of the current centroid position. Therefore, a sufficient amount is necessary to spread the current profile beyond the LCFS and allow for an efficient induction of toroidal halo currents.

Figure IV.25 on the right, shows the dependence of τ_{CQ} on n_{Ne}. From this, it becomes apparent that the boundary conditions become more important when the radiation does not dominate the post-TQ behavior and different CQ durations are achieved depending on the limit on the parallel heat conduction. Furthermore, there is an interplay between the radiation and parallel heat conduction when n_{Ne} is not sufficient to cool down the core, but still influences the overall dynamics. Here, the edge temperature plays an important role. A large heat flux to the boundary cools down the edge, so that the impurity radiation can become important in this region and accelerate the VDE. Therefore, an accurate modeling of the heat flux, the impurity radiation and the resistivity are important as the VDE dynamics in this regime is very sensitive to their influence.

In order to estimate the fraction of the available energy that is lost by radiation, it is necessary to know how much of it is transferred to the conductive structures. This can be estimated in the simulation by calculating the Ohmic heating energy W_{Ohm} of the plasma current during the CQ as the magnetic energy W_{mag} is either transferred to the conductive structures or transformed into thermal energy:

$$W_{\text{coupl}} = W_{\text{mag}} - W_{\text{Ohm}} \tag{IV.6}$$

The coupled energy for fast current quenches is around 50 %, resulting in a radiation fraction of the magnetic energy of around 80 % as illustrated in figure IV.26. The total radiation fraction cannot be calculated in this case due to the simplified TQ by perpendicular heat conduction.

IV.4.7 Conclusion for SPI mitigated VDEs

In this section, axisymmetric JOREK simulations were compared to mitigated VDE discharges described in section III.2. They reproduce the essential features of the experiment like the τ_{CQ}, the current centroid evolution, the halo width as well as the reduction of the vertical force.

The increase of the halo width by current diffusion, observed in DIII-D [Eid11] and the AUG experiments in section III.2, leads to a decoupling of the magnetic axis and the current centroid. As a consequence of the toroidal halo current keeping the current centroid stationary, the vertical force decreases. The scan of the SOL temperature in section IV.4.2 intended to assess the importance of the boundary condition on the dynamics. Here, it was found that the cases with lower boundary heat fluxes best fit the experimental data. From this, we conclude that radiation is the primary loss mechanism of the magnetic energy with a radiative fraction $(\frac{P_{rad}}{P_{Ohm}})$ of over 90 %.

The simulations in section IV.4.4 for different injection times showed the proportionality of the maximum of the vertical force and the maximum change of the vertical current moment $I_p \Delta Z_{\text{curr}}$ as predicted in section II.3.4. When the time of the disruption is smaller or comparable to the wall time, the force can be even reduced further due to shielding effects of the conductive structures as shown in predictive ITER simulations in section IV.4.5. The importance of a conductive wall for the force reduction was already highlighted in [Str17, Cla19], while the effect of the reduced ΔZ_{curr} on the force was not investigated. Apart from the vertical force reduction, this mechanism also explains the absence of the horizontal force like observed in mitigated disruptions in JET [Ger21]. As q_{95} increases, the 1/1 kink mode associated to the horizontal forces in JET [Ric04] can not be established.

When decreasing the halo width artificially like done in section IV.4.3, the current centroid and the magnetic axis are coupled again and q_{95} decreases as the area shrinks faster than I_p decays. Consequently, the vertical force increases. In conclusion, a broad halo width leading to a stationary current centroid is essential for mitigating the vertical forces. Otherwise, the current centroid displaces similarly to the magnetic axis, which is unstable below a certain threshold current $I_{p,\text{th}}$, leading to a force $\propto I_{p,\text{th}} \Delta Z_{\text{max}}$, where Z_{max} is the distance between the equilibrium Z-position and the divertor. In this case, the force can only be mitigated via the shielding by induced eddy currents, which can be sufficient in case the wall time is longer than the time of the disruption $\tau_{\text{disruption}}$ like described in [Pus17].

V JOREK-CARIDDI coupling

The previous sections included simulations with the JOREK-STARWALL version of the code. As described in section II.5.2, STARWALL is limited to thin-wall approximations and axisymmetric walls with the possibility of introducing holes. Including simplified coil structures is possible like done for the PSL, however, only with limited degrees of freedom. In the following, we will describe the coupling and benchmarks of JOREK with the volumetric wall-code CARIDDI, starting with the model capabilities in section V.1, followed by a description of the implementation in section V.1.1. The JOREK-CARIDDI model was benchmarked against STARWALL in section V.2 before it was employed for hot VDE simulations in section V.3.

V.1 The CARIDDI code

In contrast to STARWALL, the CARIDDI code offers a more realistic representation of structures by volumetric elements [Alb88, Vil13]. Similar to STARWALL, it is an electromagnetic FEM code for wall current evolution. So far, it was coupled to the 2D linear code CarMa [Por08] as well as the non-linear 2D code CarMa0NL [Vil13] that uses an evolutionary equilibrium approach. The coupling to a non-axisymmetric MHD code like JOREK allows to study the interaction between 3D MHD activity and non-axisymmetric wall structures. Furthermore, the CARIDDI code offers more realistic modeling of virtual diagnostics by including non-axisymmetries and shielding effects by the surroundings as well as more realistic shielding of active coils by the 3D structures. However, one of the most interesting applications is the capability to model halo currents more self-consistently. In particular, the capability to represent multiply connected domains is essential to model the realistic halo current path. So far, the EM coupling with the JOREK code only takes into account induced solenoidal currents in the surrounding wall structures, while halo currents cross the domain between plasma and PFCs. A halo current model was implemented in CarMa0NL [Alb15], including the halo current path in the structures. An extension for JOREK to explicitly consider halo currents is currently under development.

The work of this thesis includes the eddy current coupling between JOREK and CARIDDI in the reduced MHD model, which has also been published in [Ise23b] and is the result of a close cooperation with the CARIDDI developers in the framework of the TSVV project focusing on fast MHD transients[1]. In particular, the simulations with CarMa0NL shown in the following and part of the CARIDDI calculations, as well as the major part of the development inside CARIDDI, were performed by N. Isernia. Whereas, developing the interface with the CARIDDI code as well as the JOREK and STARWALL simulations are work mainly performed by the author of this thesis.

The CARIDDI code solves the time evolution of the current in the external structures given by equation (II.46) and provides the total tangential magnetic field (II.50) at the computational

---

[1] The Theory, Simulation, Validation and Verification tasks are part of a European research program to advance understanding of fusion processes to predict the outcome of future devices `https://euro-fusion.org/eurofusion-news/advanced-computing-grants-for-fusion` (accessed 16.01.2024)

boundary of JOREK. Here, the elements consist of optionally pentahedra or hexahedra, where the current density $\mathbf{J}$ is described by the current vector potential $\mathbf{T}$, so that their solenoidality is guaranteed as $\mathbf{J} = \boldsymbol{\nabla} \times \mathbf{T}$. The background of the implementation and the mathematical formulation were laid out in [Ise22, Ise23b] so that the coupling process is merely sketched out in the following section to provide its underlying principles. More details about the representation inside CARIDDI and their integration methods are available in the references.

V.1.1 Implementation of the coupling

Integrating the external domain of CARIDDI into the reduced MHD model of JOREK requires several steps to exchange information between the codes, as illustrated in a simplified way in figure V.1. The colors of the paths refer to certain parts of the calculation that will be highlighted in the following. While JOREK only needs minor adaptions due to the similarities of the coupling scheme to STARWALL, some additional modifications were necessary inside CARIDDI to treat the information coming from JOREK and provide the matrices needed for the time evolution and the boundary conditions.

In the first step, the magnetic flux ψ of JOREK has to be represented by equivalent currents on a thin shell surrounding the plasma using the virtual casing principle by solving the weak form of Ampère's law:

$$\int \mathbf{w}_k \cdot \psi \boldsymbol{\nabla} \phi \, \mathrm{d}V = \frac{\mu_0}{4\pi} \int \mathbf{w}_k \cdot \int \frac{\mathbf{w}_j \mathbf{I}_{\mathrm{eq},j}}{|\mathbf{r} - \mathbf{r}'|} \mathrm{d}V' \mathrm{d}V, \tag{V.1}$$

where $\mathbf{w}$ are the CARIDDI edge basis functions and $\mathbf{I}_{\mathrm{eq},j}$ are the coefficients of the equivalent currents. In practice, Gaussian integration is used, where ψ is evaluated at the point on the JOREK computational boundary closest to the Gauss point on the equivalent shell. The shell consists of thin, hexahedral elements and the geometric center can be chosen to be inside or outside the JOREK boundary or overlapping. Rewriting (V.1) as matrices, normalizing the current with μ_0 and absorbing the remaining coefficients in the matrix definition, we obtain:

$$\underline{\mathbf{M}}_{pw} \psi^e = \underline{\mathbf{M}}_{pp} I^{\mathrm{equiv}} \tag{V.2}$$

As ψ in JOREK contains both the plasma and the contribution from external currents, the external contribution has to be subtracted to obtain the plasma equivalent currents $\mathbf{I}_p^{\mathrm{equiv}}$:

$$\mathbf{I}_p^{\mathrm{equiv}} = \underline{\mathbf{M}}_{pp}^{-1} \left(\underline{\mathbf{M}}_{pe} \psi - \underline{\mathbf{M}}_{pw} \mathbf{I}_w \right), \tag{V.3}$$

where the matrix $\underline{\mathbf{M}}_{pe}$ contains the projection of the JOREK basis functions onto the CARIDDI ones and $\underline{\mathbf{M}}_{pw}$ provides the contributions of the wall currents $\mathbf{I}_w$. This corresponds to equation (II.45), with the general 3D vector potential replaced with ψ due to the reduced MHD assumption. The multiplication with the inverted self-inductance matrix $\underline{\mathbf{M}}_{pp}$ then leads to $\mathbf{I}_p^{\mathrm{equiv}}$. Note that the currents are not explicitly calculated in the final formulation, as only the matrices derived from it are necessary. We can identify this equation with the paths marked in red in figure V.1.

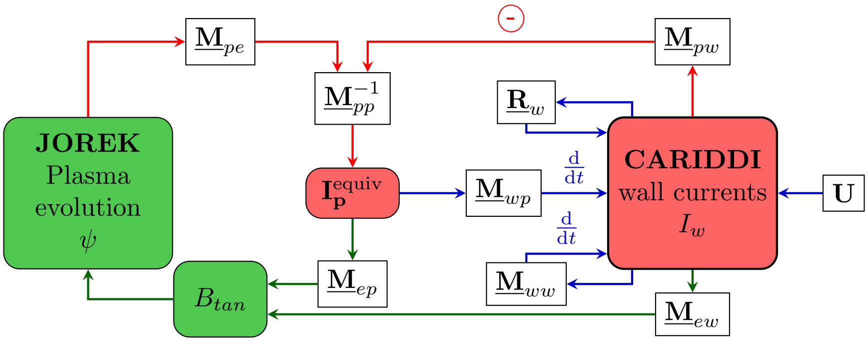

Figure V.1: Diagram of the information flow in the coupling. The colors of the paths represent the contributions to the equivalent current, the wall current evolution and the tangential magnetic field. The boxes marked in green represent quantities expressed in the JOREK basis functions, the ones marked in red in the CARIDDI basis functions.

In the second step, the ingredients for the time evolution of the wall currents are assembled. The wall currents evolve self-consistently according to the following equation equivalent to (II.46):

$$\underline{\mathbf{M}}_{ww}\dot{\mathbf{I}}_w + \underline{\mathbf{R}}_w\mathbf{I}_w + \underline{\mathbf{M}}_{wp}\dot{\mathbf{I}}_p^{\text{equiv}} = \mathbf{U}, \tag{V.4}$$

which requires the induced voltages due to the changing plasma currents $\underline{\mathbf{M}}_{wp}\dot{\mathbf{I}}_p^{\text{equiv}}$, the evolving wall currents $\underline{\mathbf{M}}_{ww}\dot{\mathbf{I}}_w$ as well as the resistive decay of the wall currents $\underline{\mathbf{R}}_w\mathbf{I}_w$. Additionally, an external voltage $\mathbf{U}$ can be specified. The blue paths in the diagram V.1 represent equation (V.4). The mutual inductance and self-inductance matrices, as well as the resistances, are calculated within CARIDDI using the usual approach described in [Vil13]. Analogous to the STARWALL implementation described in section II.5.2, a similarity transform in the form of a general eigenvalue problem is performed on the derived matrix $\underline{\tilde{\mathbf{M}}}_{ww} = \underline{\mathbf{M}}_{ww} - \underline{\mathbf{M}}_{wp}\underline{\mathbf{M}}_{pp}^{-1}\underline{\mathbf{M}}_{pw}$ and $\underline{\mathbf{R}}_w$ as defined in equation (II.48). The time evolution is performed inside JOREK, given the matrices calculated by CARIDDI.

Finally, JOREK requires the specification of B_{tan} on the computational boundary, which consists of the plasma contribution $\underline{\mathbf{M}}_{ep}\mathbf{I}_p^{\text{equiv}}$ and the external contribution by wall currents $\underline{\mathbf{M}}_{ew}\mathbf{I}_w$, where the matrices contain the Fourier decomposition and the projection on the JOREK basis functions. $\mathbf{B}_{\text{tan}}^e$ thus has the following form:

$$\mathbf{B}_{\text{tan}}^e = \underline{\mathbf{M}}_{ep}\mathbf{I}_p^{\text{equiv}} + \underline{\mathbf{M}}_{ew}\mathbf{I}_w, \tag{V.5}$$

where the magnetic field is calculated from the Biot-Savart law and coefficients are again absorbed into the matrices. While the magnetic field is computed by CARIDDI, the JOREK interface provides the tangential vectors and performs the projection on the Bezier basis functions of JOREK as well as the Fourier decomposition.

CARIDDI provides the matrices defined in table V.1 to JOREK, which proceeds to calculate further derived matrices needed for the time stepping like in the STARWALL coupling [Höl12].

All matrices required for the free-boundary evolution in JOREK depend on the geometry

Table V.1: Matrices calculated inside CARIDDI that are transferred to JOREK.

Name	Origin	Function
$\underline{\mathbf{M}}_{ee}$	$\underline{\mathbf{M}}_{ep}\,\underline{\mathbf{M}}_{pp}^{-1}\underline{\mathbf{M}}_{pe}$	Vacuum solution of ψ
$\underline{\mathbf{M}}_{ey}$	$\left(\underline{\mathbf{M}}_{ew} - \underline{\mathbf{M}}_{ep}\underline{\mathbf{M}}_{pp}^{-1}\underline{\mathbf{M}}_{pw}\right) S$	Contribution from wall currents in eigenvector basis
$\underline{\mathbf{M}}_{ye}$	$\mathbf{D}^{-1}\underline{\mathbf{S}}^T\underline{\mathbf{M}}_{wp}\underline{\mathbf{M}}_{pp}^{-1} M_{pe}$	Vector potential from plasma at wall position
$\underline{\mathbf{M}}_{yy}$	$D^{-1} = \left(\underline{\mathbf{S}}^T\underline{\tilde{\mathbf{M}}}_{ww}\underline{\mathbf{S}}\right)^{-1}$	Self-inductance matrix of external structures in eigenvector basis (diagonal)
$\underline{\mathbf{S}}$	$\underline{\mathbf{S}}$	Result from the eigenvector problem; transforms current into eigenvector basis
$\underline{\mathbf{S}}^{-1}$	$\underline{\mathbf{S}}^{-1}$	Transforms currents back into the original basis

of the plasma boundary and wall structures as well as the resistances of the latter. Since this information does not change over time, the matrices only need to be calculated once before the JOREK time evolution.

A series of analytical tests was carried out in [Ise23b] to validate the presented formulation. For this, the $\mathbf{A}$ was calculated for a tilted wire, projected on the JOREK basis functions and multiplied with $\underline{\mathbf{M}}_{ee}$ to obtain $\mathbf{B}_{\text{tan}}$. Finally, this was compared to the analytical result. In order to represent the full B_{tan}, the full MHD form of the coupling scheme was required.

After performing the first tests, it was found that the accuracy of the integration in CARIDDI needed to be improved to obtain accurate results at the JOREK boundary when hexahedral elements were used. The difficulties come from the fact that the elements of the coupling shell are toroidally elongated due to the finer discretization of the poloidal plane, making multiple Gauss points in the toroidal direction necessary. As the magnetic field has to be calculated very close to the coupling shell, these inaccuracies have a large influence on the magnetic field and, thus, the plasma evolution. This problem was eliminated by introducing more Gauss points in the toroidal direction, so that a sufficiently high accuracy could be achieved [Ise23b]. In STARWALL, the thin triangles allow a semi-analytical approach for integration [Mer15], so that a high integration accuracy can be achieved with coarser discretization.

In the following, the benchmarks between JOREK-STARWALL and JOREK-CARIDDI are presented.

V.2 Benchmarks between JOREK-STARWALL and JOREK-CARIDDI

For further verification, several benchmarks between JOREK-STARWALL (JS) and JOREK-CARIDDI (JC) were set up to test the free-boundary coupling in both axisymmetric and non-axisymmetric situations. In the 2D cases, the code CarMa0NL [Vil13] was also used as a further benchmark tool, since it differs in the physics model but shares the wall structures with JC. First, a freeboundary equilibrium is set up in section V.2.1, followed by a VDE test case in section V.2.2. For the 3D benchmarks, a tearing mode case is performed in section V.2.3 and finally, the start of a hot VDE is calculated in section V.2.4, where the insertion of a port breaks the axisymmetry of the wall.

V.2.1 Free-boundary equilibrium

A calculation of a free-boundary equilibrium in JC, JS and CarMa0NL based on the equilibrium of the AUG discharge # 39655 used in the previous section starts the series of benchmarks. As CarMa0NL only allows specific shapes of the current and pressure profiles and does not consider currents outside the SOL unless explicitly given, the equilibrium was simplified, so that it can be imported into all the codes. Furthermore, CarMa0NL only evolves the pressure p instead of ρ and T seperately.

Therefore, we assume a constant density throughout the whole domain in JOREK for simplicity and set the temperature to obtain the same p profile. The coil currents from the experiments were used both in STARWALL and CARIDDI, for which the PF coil system of AUG was also included as structures. With the given profiles and PF coil currents, the same equilibrium is obtained by all the codes. This is a first indication that the vacuum magnetic field and external field is calculated correctly and furthermore that the PF coils are implemented in the same way.

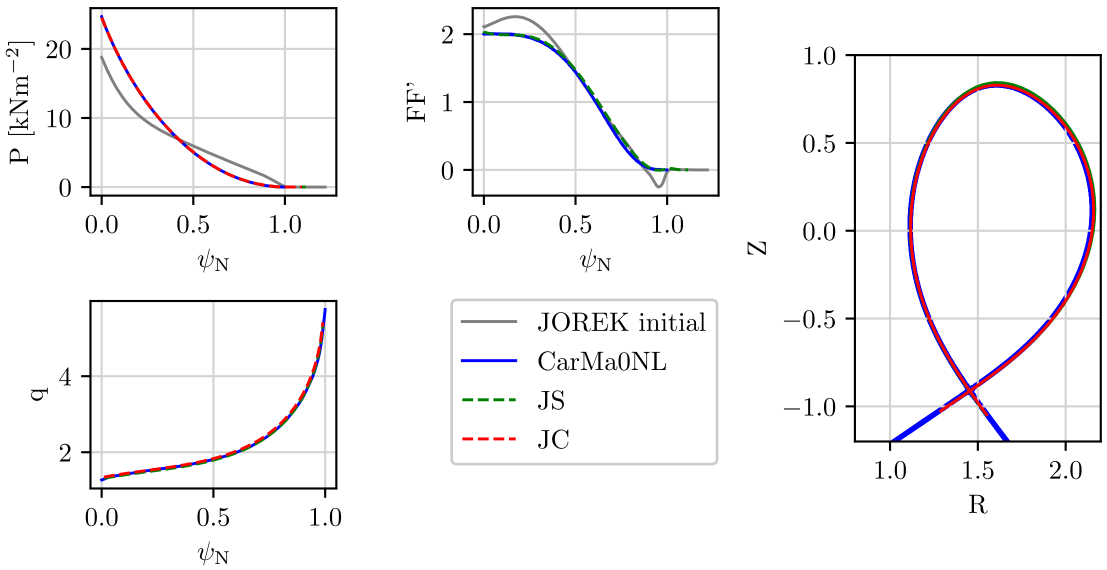

Figure V.2: The profiles of section IV.1 were modified to be compatible with CarMa0NL. The equilibria obtained by the JOREK-CARIDDI (JC), JOREK-STARWALL (JS) and CarMa0NL are nearly identical.

V.2.2 VDE benchmark with STARWALL, CARIDDI and CarMa0NL

Next, a VDE test was set up, where the geometry, position, and conductivity strongly affect the plasma evolution, which is thus a valuable test for the model. In order to make a direct comparison between JS and JC possible, the model of the passive structures was simplified. An axisymmetric wall model with a thin wall (of finite thickness) was constructed in CARIDDI. Similarly, the PSL was simplified to consist of two unconnected loops with a rectangular cross-section consisting only of one degree of freedom (no local eddy currents). This is similar to the STARWALL setup, where the PSL is modeled with two independent loops with several bands in radial direction for this setup.

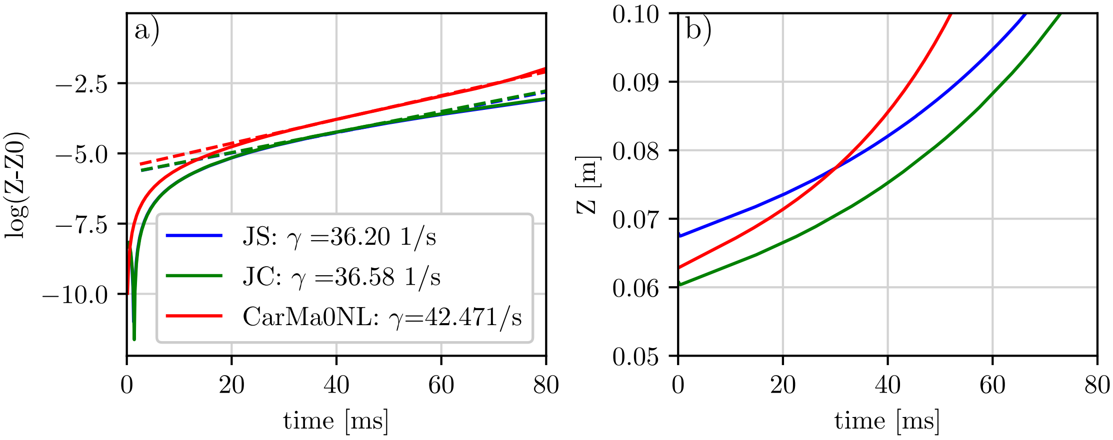

Figure V.3: a) The vertical growth rates (corresponding to the slope of the dashed lines) between the JOREK-STARWALL model (JS) and the JOREK-CARIDDI (JC) model are very similar, while CarMa0NL shows a faster evolution due to the different physics models. b) The slightly different initial position also influences the evolution of the magnetic axis. (adapted from [Ise23b])

The resistivities of the wall and coil were set up to be equivalent between the two models and the same equilibrium as described above is taken as a basis for the VDE evolution. Here, the vertical motion is initiated by an upward vertical kick with the fast control coils by varying their current anit-symmetrically by 2.5 kA.

The slightly different initial positions lead to a different time evolution of the magnetic axis position as shown in figure V.3 b). However, the vertical growth rates indicated in figure V.3 a) show almost identical values for the models JC and JS. While JC and CarMa0NL share the same model of the passive structures and PF coils, the physical model of the latter uses an evolutionary equilibrium approach and does not allow halo currents unless explicitly specified. Therefore, the disparity in the growth rate between the JOREK model and CarMa0NL is suspected to result from this difference.

An indication for this is the evolution of the PSL current with the axis displacement illustrated in figure V.4. The good correspondence between the JS, JC, and the CarMa0NL results demonstrates that the coupling between the plasma and wall are similar in all the cases. Only the time points prior to the plasma touching the computational boundary are compared, as oth-

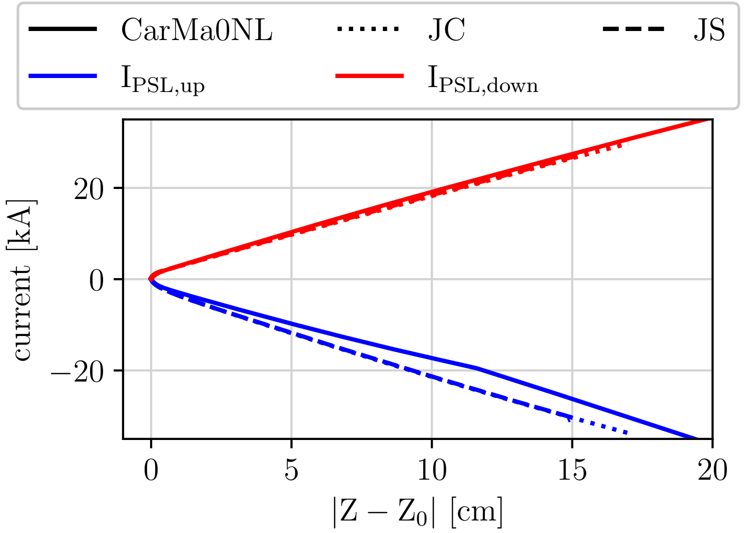

Figure V.4: The evolution of the upper and lower PSL current with the vertical displacement is similar for the JC, JS and CarMa0NL simulations, indicating that the coupling between the plasma and the passive structures is similar. (reproduced from [Ise23b])

erwise, the different physics models of JOREK and CarMa0NL would make a direct comparison more difficult.

V.2.3 Tearing modes

The following benchmark consists of a tearing mode in the no-pressure limit aiming to verify that the coupling procedure also works for non-axisymmetric cases. For this, two different set-ups were used as described in the following.

Axisymmetric wall First, a large aspect ratio case is chosen, leading to elongated elements in the wall and coupling surface due to the finite number of elements chosen in toroidal direction. The plasma has a major radius of 10 m with a circular cross-section of a radius of 1 m. The initial profiles are unstable to a 2/1 tearing mode that is influenced by the wall resistivity. In particular, the q-profile was adjusted to move the $q = 2$ surface close to the computational boundary to enhance the coupling to the axisymmetric wall of circular cross-section located at a distance of 10 cm.

The nominal wall resistivity η_w of $5 \times 10^{-7}\,\Omega\,\mathrm{m}$ is varied to compare the results of JS and JC over a range of growth rates. The corresponding $\eta_{\mathrm{thin},w}$ in STARWALL is $1 \times 10^{-4}\,\Omega$ as the axisymmetric wall in CARIDDI has a thickness of 5 mm. Due to some initial problems with the integration accuracy of hexahedral elements, the wall and coupling shell in CARIDDI are discretized by pentahedral elements in this case, which makes it more similar to the STARWALL elements. The growth rate was measured during the linear growth phase of the $n = 1$ magnetic energy. Figure V.5 shows that a good agreement can be achieved over different orders of magnitude of the wall resistivity ranging from the no-wall limit to the ideal wall limit. This

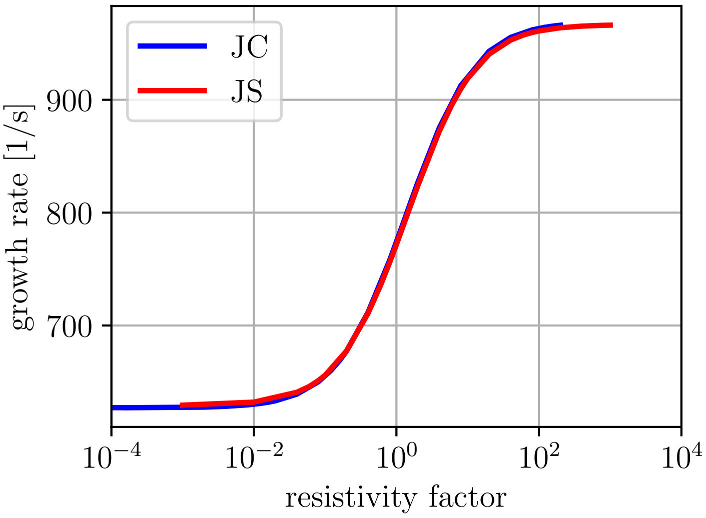

Figure V.5: The growth rates of the tearing mode between JS and JC match well from the ideal wall limit to the no wall limit. The resistivity factor is the scaling factor of the nominal η_w. (reproduced from [Ise23b])

shows the successful implementation for the coupling also for the $n > 0$ harmonics.

Non-axisymmetric wall After this proof of principle for the non-axisymmetric scenario, an asymmetry was introduced in the wall in the form of a localized port at the bottom with a poloidal extent of 50° and a toroidal extent of 30° as illustrated in figure V.6 (right). In STARWALL, the port is modeled by artificially increasing the wall resistivity in the defined region. The wall outline corresponds to the AUG shape, and an artificial equilibrium was set up with the plasma boundary close to the wall, removing the PSL. Like the previous case, the equilibrium is a zero pressure case, which is unstable to a tearing mode. The FF' profile was adjusted to move $q = 2$ surface close to the computational boundary and enhance the coupling to the conductive wall.

The simulations are carried out with the $n = 1$ and $n = 2$ harmonic included in CARIDDI and STARWALL. In the standard case with an axisymmetric wall, the tearing mode starts growing due to finite initial perturbations in JOREK, while the $n = 2$ mode energies remain on noise levels as shown in figure V.6 (left). After the $n = 1$ mode has reached a specific energy, it non-linearly triggers the growth of the $n = 2$ mode with twice the $n = 1$ growth rate.

When the port is introduced in the wall, the $n = 2$ mode grows earlier due to an $n = 1$ perturbation in the wall currents. As the $n = 1$ mode directly drives the growth rate of the $n = 2$ mode by linear coupling by the wall currents, their growth rates are equal. On the right of figure V.6, the effect of the port on the wall currents is illustrated. The helical currents induced by the growth of the $n = 1$ mode are inhibited, allowing the coupling of modes. However, the port needs to be sufficiently large to change the growth rate of the $n = 1$ mode. For this, more ports would be required to change the effective resistivity of the wall significantly.

After performing benchmarks separately for the setups with $n = 0$ and $n > 0$ separately, we

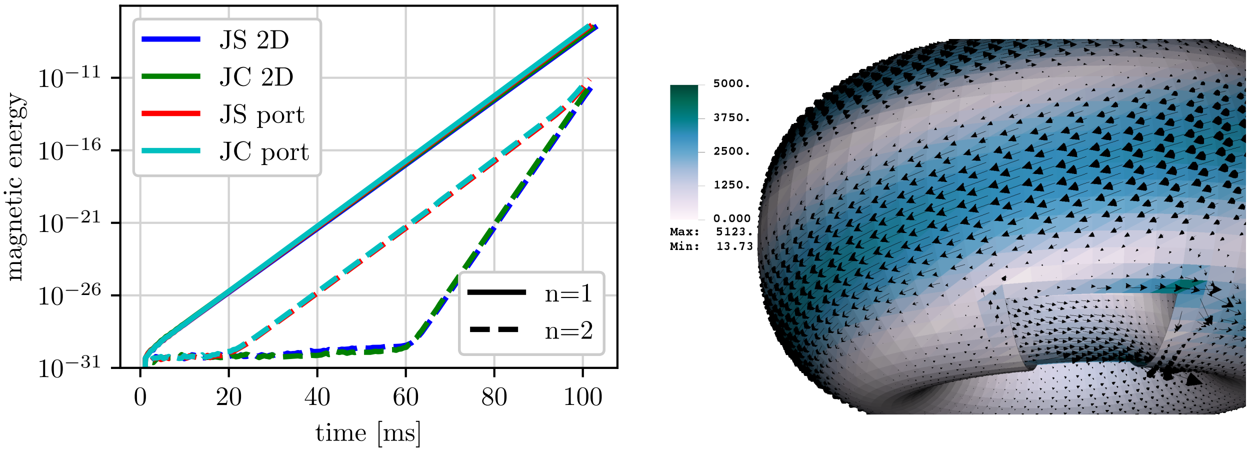

Figure V.6: In the case without ports (2D), the $n = 1$ mode triggers the growth of the $n = 2$ mode non-linearly after it reaches a certain energy. In the presence of a port, the $n = 2$ mode grows earlier due to the linear coupling by the non-axisymmetric wall (reproduced from [Ise23b]). On the right, the wall currents in the presence of the hole are illustrated.

perform the start of a 3D VDE simulation with JS and JC in the presence of a non-axisymmetric wall.

V.2.4 Asymmetric wall benchmark

Hot VDE dynamics have both a significant $n = 0$ and $n > 0$ contribution as the axisymmetric vertical motion triggers low-n modes after the outer layers of the plasma are scraped off. In order to make STARWALL and CARIDDI comparable, the conductive structures are chosen to be simple, as STARWALL only has limited capability to represent complex wall structures. Therefore, similar to the case presented above, a rectangular port is introduced on the outer midplane of the wall, and the PSL is removed to enhance the effect of the non-axisymmetric wall. Two different port locations are chosen: one at the midplane and the other at the lower side of the wall. They both have a poloidal extent of 50° and a toroidal one of 30°. The equilibrium is based on AUG # 39655, as described in section IV, and the downward VDE is triggered by a kick in the fast vertical control coils of 2.5 kA.

As described in the previous section IV, the scraping off of the plasma edge during the vertical motion reduces the edge safety factor as shown in figure V.7 b). Due to the absence of the PSL and the relatively large distance to the wall, the plasma motion is faster compared to the simulations presented before. The presence of the port slightly accelerates the vertical motion represented by the dashed and dotted lines in figure V.6 a). This is because the eddy currents are perturbed and, thus, are less efficient in stabilizing the plasma motion.

Additionally, perturbations are introduced in the plasma by the non-axisymmetric wall currents as indicated by the higher $n = 1$ and $n = 2$ energies shown in figure V.6 c) and V.6 d). The ramp-up of the control coils induces mirror currents in the wall structure that are deviated by the port and thus become non-axisymmetric. Therefore, the midplane port causes more

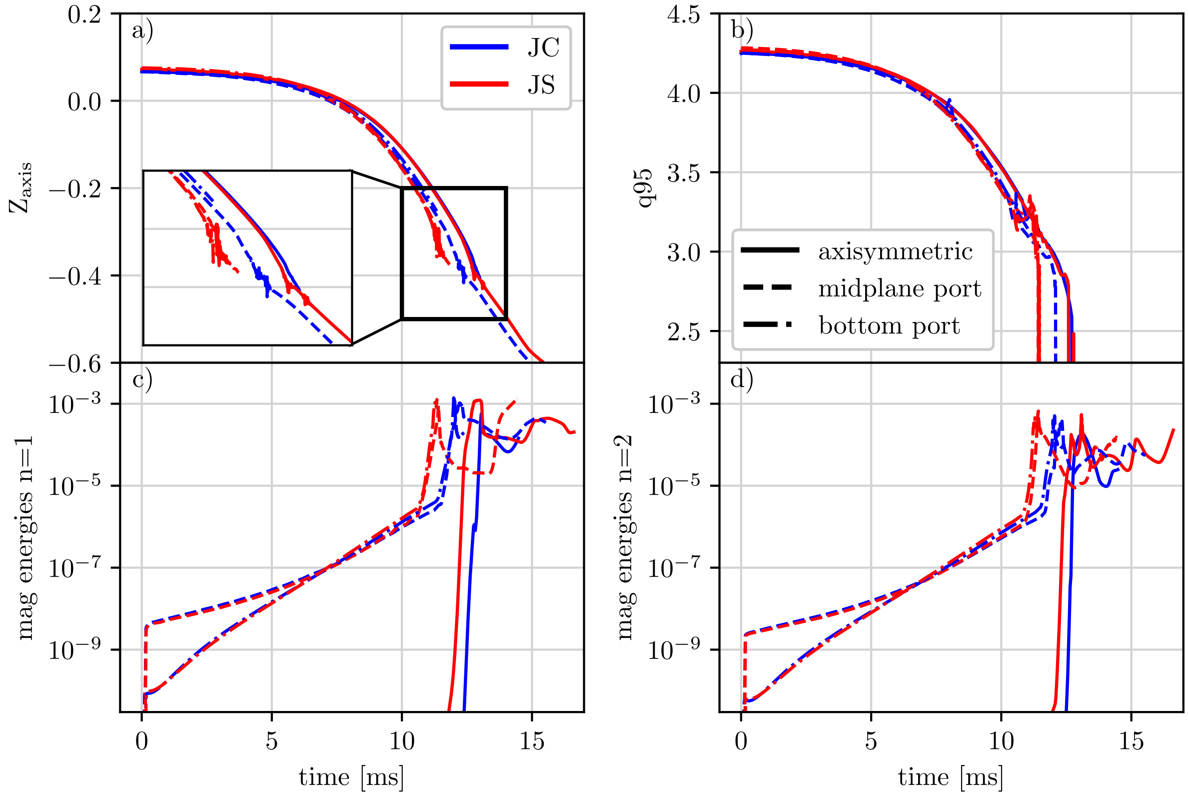

Figure V.7: The a) magnetic axis and b) q_{95} evolution is not influenced significantly by the presence of the port. The c) $n = 1$ and d) $n = 2$ magnetic energies grow earlier due to the $n = 1$ perturbation induced by the wall currents. The TQ onset point is slightly earlier in the presence of the port. (reproduced from [Ise23b]).

significant energy perturbations as it is closest to the control coils that are located on the top and bottom of the midplane just outside the vacuum vessel. In contrast, the energies in the case with an axisymmetric wall increase later due to the non-axisymmetric plasma modes. The results of this section verified the newly established coupling between JOREK and CARIDDI by performing several benchmarks for both axisymmetric and non-axisymmetric cases.

V.3 AUG VDE with realistic wall structures

The goal of coupling JOREK and CARIDDI is to allow for self-consistent simulations of non-axisymmetric plasmas with realistic 3D, volumetric wall structures. While the coupling of halo currents and adequate boundary conditions are needed to be fully self-consistent, we will investigate in this section the effects of the 3D wall structures of AUG on the evolution of a VDE in the eddy current model.

V.3.1 Presentation of AUG structures in CARIDDI

The passive stabilizing loop The PSL [Her10] model of CARIDDI illustrated in figure V.8 is more complex that the one implemented in STARWALL, which was designed to only capture the stabilizing effects against the vertical motion. The model has been constructed previously for simulations of AUG structures with CARIDDI and can now also be used for JOREK simulations thanks to the coupling.

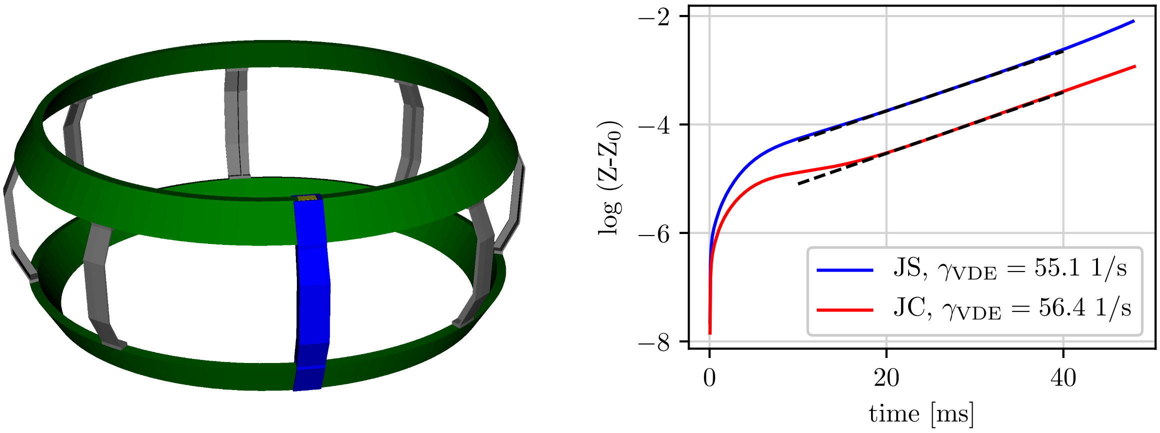

Figure V.8: (Left) The PSL consists of two loops (green) that are connected via a conductive bridge (blue and yellow) to enforce an anti-symmetric current in the loops to stabilize vertical motion. The loops are also closed by a resistor to avoid arcing events. The structural steel bridges (grey) are electrically isolated from the loops and set to a large resistivity. (Right) The vertical growth rate between the PSL model of STARWALL (JS) and CARIDDI (JC) is comparable.

A conductive bridge connects the two toroidal loops made of copper, which are closed by resistors to avoid arcing events. In reality, these resistors are made of rods on top of the PSL, while in the model, they are connected directly by a structure with the same resistance as the rods (not visible in the figure). The bridge connects the loops to enforce a toroidal anti-symmetric current during a VDE that can stabilize the vertical motion and not interfere with the break-down (the current change in the central solenoid). Inside the model, this is done by connecting the outer side of the bridge (blue) electrically with the right ends of the loop while it is isolated from the other end. Vice versa, the left ends of the loop are electrically connected to the inner part of the bridge (yellow). The inner and outer bridges are electrically isolated.

Apart from these features, the PSL model of CARIDDI also allows local eddy currents to flow as it contains multiple elements in the width and height of the loops. In contrast, the STARWALL model only allows a global current. This offers the possibility of investigating the shielding effects of active, non-axisymmetric coils like the resonant magnet perturbation (RMP) coils used to suppress edge instabilities (ELMs) or shielding effects for magnetic diagnostics.

The resistivity for the current path relevant for vertical stabilization, that flows anti-parallel in the two toroidal loops, is at 23 mΩ, while the inductance of the system is 13.2 µH. Tests within CARIDDI have shown that the time constant $\tau = \frac{\mathcal{L}}{\mathcal{R}}$ of this eigenmode is approximately 0.7 s [Ise23a], close to the literature value of 0.6 s. Previous calculations of the STARWALL model have shown that similar values are obtained [Sch20].

A 2D VDE simulation with JS and JC using the advanced PSL model in figure V.8 (Right) in contrast to the simplified one shown in figure V.3 indicates that the models are able to capture the stabilizing effect on the vertical motion equally well.

Vacuum Vessel While the vacuum vessel alone cannot sufficiently stabilize the plasma motion at relevant elongations, it still influences the growth rate as shown in [Sch20]. The STARWALL model only contains a simplified, axisymmetric vessel as described in section IV.1. In contrast, the CARIDDI model also includes the port extensions and resistive bellows that electrically isolate every two sectors as indicated in figure V.9.

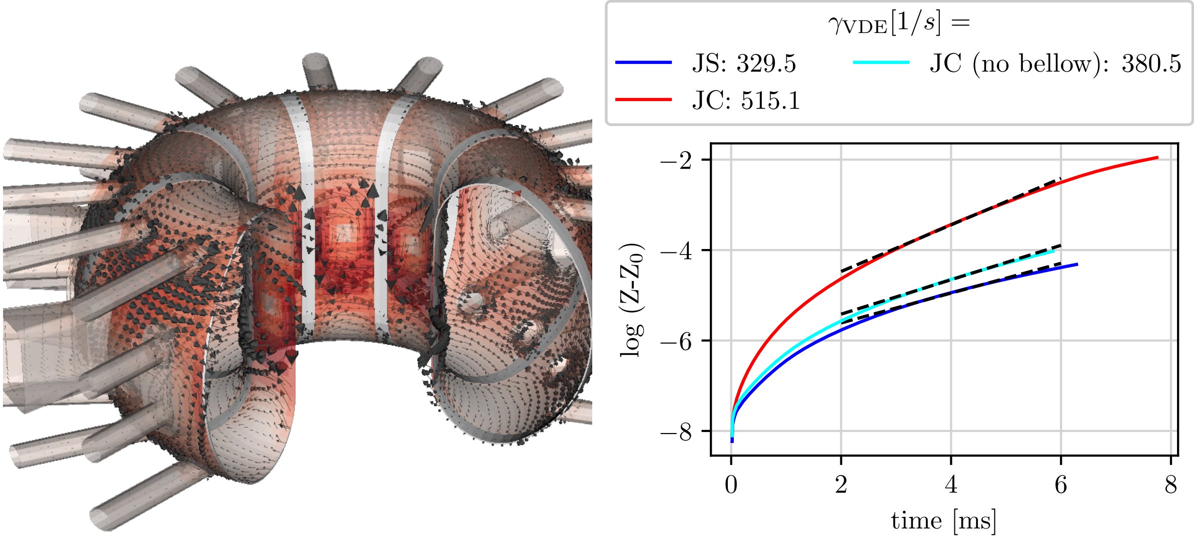

Figure V.9: The CARIDDI wall model contains the port extensions as well as the resistive bellows marked here in white. Therefore, in the case of a VDE, eddy currents form within the electrically connected sectors, as indicated here. The vertical growth rate is significantly larger compared to figure V.8 due to the distance of the VV to the plasma.

The vessel sectors consist of steel of a resistivity of 0.72 µΩ m. Measurements estimate the resistivity of the vacuum vessel including the bellows [Gia15] to 3 µΩ m or the toroidal resistance is given as 0.28 mΩ, which results in an effective resistivity of the bellows of 1.96×10^{-5} Ω m [Zam14]. Using these values, we compare the vertical growth rate of STARWALL with the CARIDDI one. The growth rates are comparable when setting up a homogeneous resistivity with the nominal value of 0.72 µΩ m. However, when the resistivity of the bellows is enhanced, the growth rate is larger with $515\,\mathrm{s}^{-1}$ than the JS one with $330\,\mathrm{s}^{-1}$ as shown in figure V.9 on the right. The wall currents circulate in eddies inside the sectors, when the η_w is non-homogeneous due to the larger resistivity in the bellows. As the validation to the AUG VDE was successful before with the homogeneous wall, the resistivities still need to be adapted to fit to the experiment.

V.3.2 3D VDE with realistic wall structures

Based on the CARIDDI model with bellows shown in the previous section and the realistic PSL, a simulation of a non-axisymmetric VDE is set up like described in section IV.3.

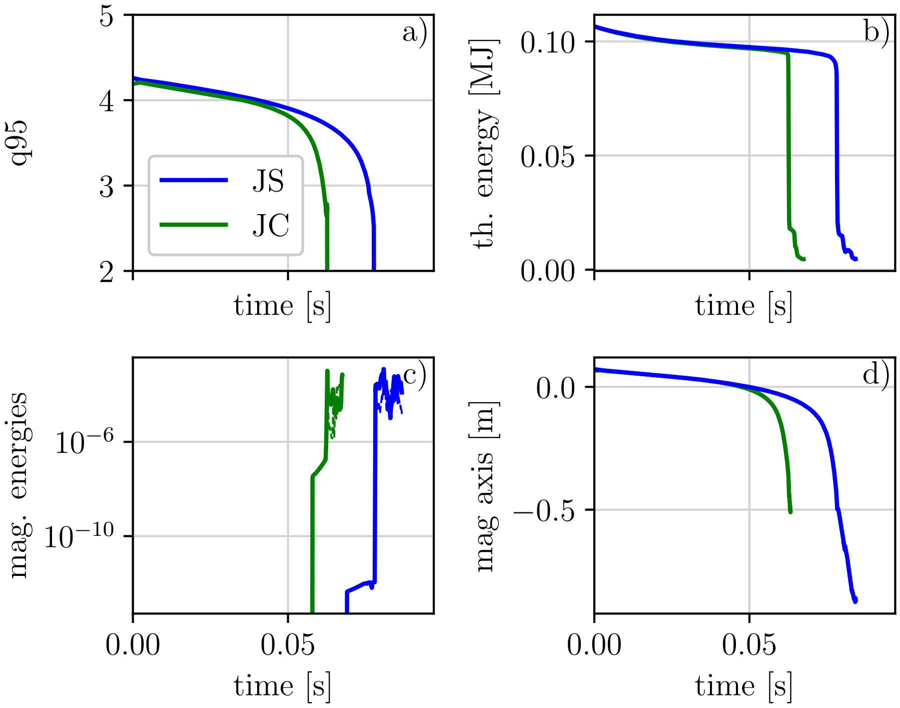

Figure V.10: Preliminary hot VDE simulations with the complete AUG structures show a faster movement (d) than in the comparable JS model. However, the time scale of the b) TQ is comparable, while the d) $n = 1$ and $n = 2$ energies are slightly higher in JC during the TQ. Due to the faster movement q_{95} decreases faster and the TQ sets in earlier.

The results of the preliminary simulations are shown here. Like stated before, the additional resistivity of the bellows expedit the vertical motion as seen in figure V.10 d). Accordingly, q_{95} will decrease on the same time scale, so that the TQ sets in earlier, but still at the same value of q_{95} for both simulations. Similar to the simulations shown in section V.2.4 with a single port, the $n = 1$ energy is initially larger due to the non-axisymmetric currents flowing in the vacuum vessel. In contrast, the toroidally symmetric VV in AUG does not increase the $n = 1$ energy, so that it starts from a lower initial perturbation. In both cases, the $n > 0$ modes were activated when the magnetic axis reached a position of $Z = -0.1\,\mathrm{m}$, which still give sufficient time for the evolution before the TQ sets in. However, the TQ time scale remained the same in the two simulations despite the slightly higher magnetic energies in the JOREK-CARIDDI simulation due to the non-axisymmetric wall currents.

First simulations of the CQ phase not shown here suggest a similar behavior between JC and JS, but require more detailed analysis for a final conclusion. In particular, the horizontal forces due to the non-axisymmetric wall structures need to be analyzed, which is work under development for the JOREK-CARIDDI simulations.

V.4 Conclusion of the JOREK-CARIDDI coupling

The benchmarks presented here and the analytical calculations from [Ise23b] show the validity of the JOREK-CARIDDI (JC) coupling for wall eddy currents and the vacuum calculation. The same formalism of the virtual casing principle as in JOREK-STARWALL (JS) is used, so that, for comparable set ups of the conductive structures, the results between the two models are very close to each other. Furthermore, a 2D benchmark with CarMa0NL provided a close match of the free-boundary equilibrium and the 2D VDE simulation compared to JC and JS.

This new established model allows the investigation of the effects of volumetric structures and, in future, also the inclusion of self-consistent halo currents. While JC and JS showed comparable results in the cases shown here for both axisymmetric as non-axisymmetric walls, the full capabilities of the CARIDDI conductive structures have not been explored yet. As it offers more freedom to model realistic wall structures, it can capture shielding effects for virtual magnetic diagnostics and additional degrees of freedom of other conductive structures (e.g. the PSL).

The simulations shown here provided a proof of principle of the JC coupling as a basis for future studies. Furthermore, the ASDEX Upgrade structures were characterized, with comparable vertical growth rates for the PSL and axisymmetric walls. However, the wall with bellows showed larger growth rates due to the changed current path of the eddy currents. This remains to be investigated as the axisymmetric wall model of JS was carefully validated before against experimental measurements.

VI Conclusion

> *A job is never truly finished. It just reaches a stage where it can be left on its own for a while.*
> – Neil Young, Waging Heavy Peace: A Hippie Dream

The results of the PhD project presented in the chapters III to V covered different aspects of the simulations of Vertical Displacement Events in JOREK as the overall goal of the work was to prove the reliability of the non-linear MHD code JOREK presented in section II.5.1 for the application of unmitigated and mitigated VDEs. To this extent, dedicated experiments were performed for code validation and the respective simulations were carried out. Finally, the JOREK model was enhanced by the coupling to the CARIDDI code for volumetric, realistic wall structures. In the following, the different aspects of the thesis are summarized and *points for future work are highlighted.*

VI.1 Unmititated VDEs

Unmitigated VDEs are associated with large heat loads and electromagnetic forces as the plasma comes into contact with the wall while it still has its initial temperature and current. Predictive simulations for future devices are needed to estimate whether the material components can withstand these events and how many of these scenarios are acceptable. Towards this goal, the experiments of hot VDEs in ASDEX Upgrade (AUG) (see section III.1) were designed to provide a basis for the code validation. Their results lie in the range of previous observations and a scan of the plasma current and B_ϕ allowed to see the dependence of asymmetries and forces on the parameters.

The simulations in JOREK presented in section IV.2 and IV.3 reproduced key quantities like the TQ onset due to low-n kink modes, the TQ time scale, the halo current magnitude, and the vertical forces. It was shown that the boundary conditions greatly influence the evolution of the hot VDE as the boundary heat flux represents the main loss channel of energy. Therefore, by scanning the parallel heat flux in the SOL, we could determine that at a value of the parallel conduction corresponding to a Spitzer-Haerm conductivity at a T_e of 40 to 80 eV, the current quench duration was matched as well as the wave-form of the I_p decay. Also, the halo width is closer to the experimentally measured one for these conditions.

The CQ dynamics are sensitive to the plasma state: when a $q = 1$ surface is present, it was found that a global reconnection event prevented q_{95} from decreasing below two until I_p in the core decreases to 20 to 30 % of its initial value. This can explain the absence of a significant horizontal force in AUG, as a $q_{95} \gg 1$ prevents an external 1/1 kink mode, which is responsible for the horizontal force in JET. *However, it remains for future work to investigate if this occurs in the experiment, which is challenging due to the absence of current density measurements during the disruption.*

The experiments provided valuable insight into the dynamics, while some measurements, like the magnetic diagnostics, saturate. *Future upgrades are planned for the magnetic diagnostic system as well as for the electron density measurements, which would allow for a more detailed analysis and measurements of the* I_p *asymmetry. Furthermore, direct measurements of the heat flux were not possible for this thesis, which would offer important points for comparison.*

After this validation activity, we can trust the JOREK model better for the simulation of unmitigated VDEs. However, note that the boundary conditions must be set with care as they are crucial for the dynamics. *Furthermore, the extension of JOREK to allow for currents crossing the boundary and, thus, realistic current path in the structures will also make simulations of the* I_p *asymmetry possible, which is essential to capture the horizontal force.*

VI.2 Mitigated VDEs

The mitigation methods to reduce the adverse effects of disruptions must work reliably for future machines. An important question is the mitigation efficiency for late mitigation and the reduction of the EM-forces, which was both studied in this thesis. A theory was presented in section II.3.5 to explain the force mitigation by the presence of significant toroidal halo currents in the SOL. This requires the existence of a broad halo region and the stagnation of the current centroid as a consequence. Both were observed in the SPI mitigated VDE discharges presented in section III.2, where the halo region is significantly broader compared to the hot VDE discharges. The large radiated energy fraction for all experiments indicates an efficient mitigation even for late injections into an already displaced plasma.

The corresponding simulations presented in section IV.4 reproduced key quantities such as the current centroid displacement, the vertical force, and the peak radiation. It was confirmed that the large predominantly toroidal halo currents reduce the current centroid displacement and that q_{95} remains large due to the fast current decay.

A scan of the boundary heat flux confirmed that it is negligible in radiation-dominated disruptions, as most energy is lost by radiation. Thus, the simulations with the lowest heat flux corresponded best to the experiment. It is interesting to note that the CQ duration in the mitigated scenarios is longer compared to the hot VDEs in the experiments investigated here. As the CQ duration τ_{CQ} is dominated by radiation in the former and by heat conduction as well as the VDE rate in the latter, we can assume that the presence of the strong radiation sinks reduces the heat loss to the PFCs significantly.

The shielding effects are also important in machines like ITER, where the resistive wall time is significantly longer, as shown in the respective simulations. Therefore, force mitigation can be established by reducing the source of the force (reducing the displacement of the current centroid) or by increasing the wall shielding (reducing the disruption time scale below the resistive wall time). The absence of the horizontal force in mitigated disruptions is due to the absence of the 1/1 kink mode as q_{95} increases after the TQ.

While in machines like AUG, runaway electrons do not occur naturally during disruption as the vertical displacement of the core is faster than the RE growth time, they become essential in *high current devices due to the large avalanche amplification factor. In order to take them into account self-consistently, fluid or kinetic runaway models need to be coupled to the simulation to investigate if and how many REs are generated. The current redistribution beyond the LCFS can help to reduce the current seed as fast electrons would be lost right away along the open field lines.*

VI.3 Coupling of JOREK and CARIDDI

The coupling of JOREK and the volumetric wall code CARIDDI was performed successfully for the eddy current model. A series of benchmarks with the JOREK-STARWALL model showed the reliability of the results for both axisymmetric as well as non-axisymmetric simulations. Moreover, the effect of non-axisymmetric walls, which can provide additional perturbations to the plasma, was investigated. This will allow the simulation of more realistic wall structures that can be derived from CAD models. *Future applications will be the investigation of shielding effects from volumetric structures, more realistic modeling of magnetic diagnostics and the interaction between non-axisymmetric plasmas and wall structures.*

The ASDEX Upgrade conductive structures of STARWALL and CARIDDI were also compared. While VDE growth rate is comparable with both PSL models, the CARIDDI model can also represent net currents, the currents in the bridge as well as skin effects to some degree. Including bellows in the vacuum vessel changes the path of induced eddy currents and accelerates the vertical growth rate. *The resistivities still need to be adjusted to match again the experimental trajectories.* However, the overall evolution of a hot VDE is similar in the JOREK-STARWALL and JOREK-CARIDDI simulations. *Further investigations are necessary to determine the influence of the non-axisymmetric wall for the forces and plasma evolution. Moreover, extending JOREK with a self-consistent halo current model, including asymmetries of I_p, is necessary to reproduce the sideways force in JET and will allow predictive simulations for future devices.*

Acknowledgements

First of all, I would like to thank my supervisors Sibylle Günter and Matthias Hölzl for giving me the opportunity to continue my research as a doctoral student after already providing support during my previous studies. In particular, thanks to Sibylle for making space in the busy schedule for meetings, for which Karl Lackner's presence was also highly appreciated for his all encompassing knowledge in fusion.

I'm deeply grateful to Matthias for encouraging me to stay in research and his constant support throughout the project. In spite of the constant amount tasks, you always find time when it is needed and I'm always surprised how you quickly find the source of any problem. Apart from providing an exciting research project with all the challenges I could wish for, I would never have expected that it would also include overcoming snowy mountains and long marches.

Also, I would like to thank Geri Papp for being the scientific counsel for the project and who made it possible to have dedicated experiments in ASDEX Upgrade. Without this, the project would not have progressed in the way it did and I'm very grateful that you were the bridge between theory and experiment.

On this note, I would also like to thank Marc Marascheck, Bernhard Sieglin, Louis Giannone, Alexander Bock, Dominik Brida, Irene Zammuto and Matthias Bernert, who helped in setting up the experiments, data access and diagnostics. It was a lot of fun to get insight into the operation and to learn about the practical side of research. Special thanks to Mike Dunne for providing the equilibria of the discharges and to Louis for taking the time to investigate possible improvements of the magnetic measurements. This project could build up on the extensive work and knowledge about disruptions of Gabriella Pautasso.

A big thank you to Anja Bauer and the secretary team for quickly responding to questions and their competence in guiding through administration work.

The installation of the SPI system is the result of an enormous amount of work, and I am grateful for the ITER Organization for allowing the use it for the VDE shots. Here again, special thanks to Geri Papp and Paul Heinrich for the support in designing the discharges and the helpful discussions.

I would like to thank Javier Artola for introducing me to the world of VDEs, and sharing his wisdom about disruptions. I take your curiosity and striving for understanding as a role model for my research. In this context, I would also like to thank the ITER organization, for making a research stay in Cadarache possible, during which the SPI validation project got its final shape. Also, a big thank you to Francesco Vannini for his interest and his work for the project.

The JOREK-CARIDDI project would not have been possible without the support and dedication of Fabio Villone, Guglielmo Rubinacci, Nicola Isernia and Salvatore Ventre, who offered access to their code and put a lot of effort into its realization. I would also like to thank them for the stay in Napoli during the project. I am especially grateful to Nicola Isernia, whose hard work was essential and who welcomed me into the Neapolitan life. I hope you felt as welcome

here.

I am very happy to see the JOREK community at IPP grow towards a great team in the last years. So thanks to the fellow PhD and Postdocs Andres Cathey, Rohan Ramasamy, Fabian Wiescholllek, Verena Mitterauer, Francesco Vannini, Weikang Tang, Hannes Bergström, Felix Antlitz and Raffaele Sparago for discussions about work and non-work.

Apart from this, I would like to thank old friends and new ones, for accompanying me on this journey. In particular, to Sabine, Maria and Milena who make me feel like no times has passed. To Wolfgang, Corinna and Jakob who made the first year of a pandemic feel like a wholesome time, and who I feel very lucky to continue to have in my life. A Daniel para estar un companero devenido amigo. To former office mates and people who share the life at IPP, Michael, David, Benedikt, Jonas, Magdalena and Andrej. To the book club people, Marco, Natalia, Mario, Rohan, Verena, Johanna and Jelena for bringing back the pleasure of reading. To Andres, Paula, Luna and Ada for bringing joy. To my family, who would always believe in me with and without understanding. And most of all, to Javi, for all the happiness y estar muy puto.

A Finite Element method (FEM)

The finite element method is a way to solve a partial differential equation (PDE). While FEM theory is complex, we aim to provide a general idea on how it is applied and advantages of this method. More details can be found here [Bre08]. The main idea is that the solution space V is approximated by a subspace V_{sub} in which the FEM solution resides. So, instead of solving the equation

$$L\mathbf{X} = \mathbf{f}, \tag{A.1}$$

where L is a differential operator acting on $\mathbf{X}$, the **weak form** of the equation is solved. The weak form is obtained by projection on the subspace by multiplying (A.1) with the test function v^* and integrating over space:

$$\int v_i^* L\mathbf{X} = \int v_i^* f \tag{A.2}$$

In practice, the solution is less constraint by this operation, e.g. second derivatives are avoided by integration by parts. Therefore, the solution space only needs to be C^1 continuous, while the strong form requires the solution to be C^2 continuous if L contains a second derivative.

The second ingredient of FEM is the discretization of space into elements of various shapes (triangles, Bezier patches, etc) and the decomposition of variables into basis functions as:

$$X = \sum x_i w_i^*, \tag{A.3}$$

where w_i^* is the basis function and x are the coefficients. The goal is now to find the coefficients x_i, so that the residual

$$\mathcal{R} \equiv \int v_i^* \left(L\mathbf{X} - f \right). \tag{A.4}$$

is minimized. Using the decomposition of $\mathbf{X}$, we obtain:

$$\mathcal{R} \equiv \int v_i^* \left(\sum_j L x_j \mathbf{w}_j^* - f \right) \tag{A.5}$$

$$= \sum_j x_j \int v_i^* L \mathbf{w}_j^* - \int v_i^* f, \tag{A.6}$$

as x_i are just prefactors. The test function v^* and basisfunction w^* are chosen, so that the integral can be computed analytically and we end up with with a linear equation system of the form:

$$Mx = f_w \quad \text{with} \tag{A.7}$$

$$M \equiv \int v_i^* L w_j^* \quad \text{and} \quad f_w \equiv \int v_i^* f \tag{A.8}$$

In case the test and basis function originate from the same function space, the method is called the **Ritz-Galerkin** method.

B Divertor data

In order to calculate the halo current according to (II.25), the number of tiles in toroidal direction is needed, as measurements are installed in the single tiles. Also, in order to calculate the current density, the area of the tiles was extracted from CAD drawings as well as their position calculated with respect to the center at R_{geo}=1.58 m and Z_{geo}=0.05 m. The values are listed in table

Table B.1: The divertor areas extraced from CAD drawings, their poloidal position and the number of tiles in toroidal direction for each divertor component are listed.

Name	A [cm^2]	θ	N$_{\text{tor}}$
PSL up	3.30		96
PSL down	3.35		96
DUAm	1.38	4.80	128
DUAu	1.73	4.74	128
DUMa	1.21	4.68	64
DUMoa	1.40	4.58	64
DUMoi	1.40	4.52	64
DUMi	0.54	4.47	64
DUIu	1.83	4.43	64
DUIm	1.20	4.39	96
DUIou	0.81	4.29	96
DUIoo	0.63	4.19	96

C References

[Ada22] Adamek, J., Artola, F., Loarte, A., et al. Current density limitation during disruptions due to plasma-sheaths. *Nuclear Fusion*, 62(8):086034, 2022.

[Alb88] Albanese, R. and Rubinacci, G. Integral formulation for 3D eddy-current computation using edge elements. *IEE Proceedings A Physical Science, Measurement and Instrumentation, Management and Education, Reviews*, 135(7):457, 1988. 10.1049/ip-a-1.1988.0072.

[Alb15] Albanese, R., Carpentieri, B., Cavinato, M., et al. Effects of asymmetric vertical disruptions on ITER components. *Fusion Engineering and Design*, 94:7–21, 2015. 10.1016/j.fusengdes.2015.02.034.

[Amb05] Ambrosino, G. and Albanese, R. Magnetic control of plasma current, position, and shape in Tokamaks: A survey or modeling and control approaches. *IEEE Control Systems Magazine*, 25(5):76–92, 2005. 10.1109/MCS.2005.1512797.

[Art20] Artola, F. J., Lackner, K., Huijsmans, G. T. A., et al. Understanding the reduction of the edge safety factor during hot VDEs and fast edge cooling events. *Physics of Plasmas*, 27(3):032501, 2020. 10.1063/1.5140230.

[Art21a] Artola, F. J., Loarte, A., Matveeva, E., et al. Simulations of COMPASS vertical displacement events with a self-consistent model for halo currents including neutrals and sheath boundary conditions. *Plasma Physics and Controlled Fusion*, 63(6):064004, 2021. 10.1088/1361-6587/abf620.

[Art21b] Artola, F. J., Sovinec, C. R., Jardin, S. C., et al. 3D simulations of vertical displacement events in tokamaks: A benchmark of M3D-C1, NIMROD, and JOREK. *Physics of Plasmas*, 28(5):052511, 2021. 10.1063/5.0037115.

[Art22] Artola, F., Loarte, A., Hoelzl, M., et al. Non-axisymmetric MHD simulations of the current quench phase of ITER mitigated disruptions. *Nuclear Fusion*, 62(5):056023, 2022. 10.1088/1741-4326/ac55ba.

[Art23] Artola, F., Schwarz, N., Vannini, F., et al. Modelling of vertical displacement events in tokamaks: status and challenges ahead. *Plasma Physic and Controlled Fusion*, (submitted) 2023.

[AS18] Artola Such, F. J. *FREE-BOUNDARY SIMULATIONS OF MHD PLASMA INSTABILITIES IN TOKAMAKS*. Thesis, Université Aix Marseille, 2018.

[Ber14] Bernert, M., Eich, T., Burckhart, A., et al. Application of AXUV diode detectors at ASDEX Upgrade. *Review of Scientific Instruments*, 85(3):033503, 2014. 10.1063/1.4867662.

[Bis93] Biskamp, D. *Nonlinear Magnetohydrodynamics*. Cambridge Monographs on Plasma Physics. Cambridge University Press, 1993. 10.1017/CBO9780511599965.

[Bon86] Bondeson, A. Simulations of tokamak disruptions including self-consistent temperature evolution. *Nuclear Fusion*, 26(7):929–940, 1986. 10.1088/0029-5515/26/7/009.

[Bon01] Bondarenko, B. D. Role played by O A Lavrent'ev in the formulation of the problem and the initiation of research into controlled nuclear fusion in the USSR. *Physics-Uspekhi*, 44(8):844, 2001. 10.1070/PU2001v044n08ABEH000910.

[Boo11] Boozer, A. H. Two beneficial non-axisymmetric perturbations to tokamaks. *Plasma Physics and Controlled Fusion*, 53(8):084002, 2011. 10.1088/0741-3335/53/8/084002.

[Boo12] Boozer, A. H. Rotation of tokamak halo currents. *Physics of Plasmas*, 19(5):052508, 2012. 10.1063/1.4717721.

[Boo19a] Boozer, A. H. Fast magnetic reconnection and the ideal evolution of a magnetic field. *Physics of Plasmas*, 26(4):042104, 2019. 10.1063/1.5081828.

[Boo19b] Boozer, A. H. Halo currents and vertical displacements after ITER disruptions. *Physics of Plasmas*, 26(11):114501, 2019. 10.1063/1.5126339.

[Boo20] Boozer, A. H. Flattening of the tokamak current profile by a fast magnetic reconnection with implications for the solar corona. *Physics of Plasmas*, 27(10):102305, 2020. 10.1063/5.0014107.

[Bre08] Brenner, S. C. and Scott, L. R. *The Mathematical Theory of Finite Element Methods*, volume 15 of *Texts in Applied Mathematics*. Springer, 2008. ISBN 9780387759333. URL `http://dx.doi.org/10.1007/978-0-387-75934-0`.

[Bre19] Breizman, B. N., Aleynikov, P., Hollmann, E. M., and Lehnen, M. Physics of runaway electrons in tokamaks. *Nuclear Fusion*, 59(8):083001, 2019. 10.1088/1741-4326/ab1822.

[Bri20] Brida, D., Silvagni, D., Eich, T., et al. Role of electric currents for the sol and divertor target heat fluxes in asdex upgrade. *Plasma Physics and Controlled Fusion*, 62(10):105014, 2020.

[Bun19] Bunkers, K. J. *The Influence of Boundary Conditions on Vertical Displacement Event Calculations*. Ph.D. thesis, University of Wisconsin, Madison, 2019. URL `https://www.proquest.com/dissertations-theses/influence-boundary-conditions-on-vertical/docview/2272841264/se-2?accountid=106441`.

[Bun20] Bunkers, K. J. and Sovinec, C. R. The influence of boundary and edge-plasma modeling in computations of axisymmetric vertical displacement. *Physics of Plasmas*, 27(11):112505, 2020. 10.1063/5.0023604.

[Che16] Chen, F. F. *Introduction to Plasma Physics and Controlled Fusion*. Springer International Publishing, Cham, 2016. ISBN 978-3-319-22308-7.

[Cla19] Clauser, C., Jardin, S., and Ferraro, N. Vertical forces during vertical displacement events in an ITER plasma and the role of halo currents. *Nuclear Fusion*, 59(12):126037, 2019. 10.1088/1741-4326/ab440a.

[Cob21] Coburn, J., Lehnen, M., Pitts, R., et al. Reassessing energy deposition for the ITER 5 MA vertical displacement event with an improved DINA model. *Nuclear Materials and Energy*, 28:101016, 2021. 10.1016/j.nme.2021.101016.

[Com16] Commaux, N., Shiraki, D., Baylor, L., et al. First demonstration of rapid shutdown using neon shattered pellet injection for thermal quench mitigation on DIII-D. *Nuclear Fusion*, 56(4):046007, 2016. 10.1088/0029-5515/56/4/046007.

[Cza08] Czarny, O. and Huysmans, G. Bézier surfaces and finite elements for MHD simulations. *Journal of Computational Physics*, 227(16):7423–7445, 2008. 10.1016/j.jcp.2008.04.001.

[Dib23] Dibon, M., de Marne, P., Papp, G., et al. Design of the shattered pellet injection system for ASDEX Upgrade. *Review of Scientific Instruments*, 94(4):043504, 2023. 10.1063/5.0141799.

[Eid11] Eidietis, N. and Humphreys, D. A diffusive model for halo width growth during vertical displacement events. *Nuclear Fusion*, 51(7):073034, 2011. 10.1088/0029-5515/51/7/073034.

[Eid15] Eidietis, N., Gerhardt, S., Granetz, R., et al. The ITPA disruption database. *Nuclear Fusion*, 55(6):063030, 2015. 10.1088/0029-5515/55/6/063030.

[Fra15] Franck, Emmanuel, Hölzl, Matthias, Lessig, Alexander, and Sonnendrücker, Eric. Energy conservation and numerical stability for the reduced MHD models of the non-linear JOREK code. *ESAIM: M2AN*, 49(5):1331–1365, 2015. 10.1051/m2an/2015014.

[Fre14] Freidberg, J. P. *Ideal MHD*. Cambridge University Press, 2014. 10.1017/cbo9780511795046.

[Fre15] Freidberg, J. P., Cerfon, A., and Lee, J. P. Tokamak elongation – how much is too much? part 1. theory. *Journal of Plasma Physics*, 81(6):515810607, 2015. 10.1017/S0022377815001270.

[Fus07] Fusion product (figure), 2007. URL `http://large.stanford.edu/courses/2012/ph240/ramos2/docs/Focus_on.pdf`.

[Gar23] Garching, I. IPP Bilddatenbank, 1991-2023.

[Ger15] Gerasimov, S., Abreu, P., Baruzzo, M., et al. JET and COMPASS asymmetrical disruptions. *Nuclear Fusion*, 55(11):113006, 2015. 10.1088/0029-5515/55/11/113006.

[Ger20] Gerasimov, S., Abreu, P., Artaserse, G., et al. Overview of disruptions with JET-ILW. *Nuclear Fusion*, 60(6):066028, 2020.

[Ger21] Gerasimov, S., Abreu, P., Baranov, Y. F., et al. Mitigation of disruption electromagnetic load with SPI on JET-ILW. In *47th EPS Conference on Plasma Physics*. European Physical Society, 2021.

[Ger23] Gerasimov, S., Carvalho, P., Ficker, F., et al. VDE mitigation with SPI on JET-ILW. In *49th EPS Conference on Plasma Physics*. European Physical Society, 2023.

[Gia15] Giannone, L., Fischer, R., McCarthy, P., et al. Improvements for real-time magnetic equilibrium reconstruction on ASDEX Upgrade. *Fusion Engineering and Design*, 100:519–524, 2015. 10.1016/j.fusengdes.2015.07.029.

[Gla99] Glasser, A. H., Sovinec, C. R., Nebel, R. A., et al. The NIMROD code: a new approach to numerical plasma physics. *Plasma Physics and Controlled Fusion*, 41(3A):A747–A755, 1999. 10.1088/0741-3335/41/3a/067.

[Goe04] Goedbloed, J., Goedbloed, J., and Poedts, S. *Principles of Magnetohydrodynamics: With Applications to Laboratory and Astrophysical Plasmas*. Cambridge University Press, 2004. ISBN 978-0-521-62607-1.

[Gor07] Gormezano, C., Sips, A., Luce, T., et al. Chapter 6: Steady state operation. *Nuclear Fusion*, 47(6):S285, 2007. 10.1088/0029-5515/47/6/S06.

[Gra96] Granetz, R., Hutchinson, I., Sorci, J., et al. Disruptions and halo currents in Alcator C-Mod. *Nuclear Fusion*, 36(5):545–556, 1996. 10.1088/0029-5515/36/5/I02.

[Gru93] Gruber, O., Lackner, K., Pautasso, G., Seidel, U., and Streibl, B. Vertical displacement events and halo currents. *Plasma Physics and Controlled Fusion*, 35(SB):B191–B204, 1993. 10.1088/0741-3335/35/sb/015.

[Han89] Haney, S. W. and Freidberg, J. P. Variational methods for studying tokamak stability in the presence of a thin resistive wall. *Physics of Fluids B: Plasma Physics*, 1(8):1637–1645, 1989. 10.1063/1.858941.

[Han15] Hanson, J. D. The virtual-casing principle and Helmholtz's theorem. *Plasma Physics and Controlled Fusion*, 57(11):115006, 2015. 10.1088/0741-3335/57/11/115006.

[Hen07] Hender, T., Wesley, J., Bialek, J., et al. Chapter 3: MHD stability, operational limits and disruptions. *Nuclear Fusion*, 47(6):S128–S202, 2007. 10.1088/0029-5515/47/6/S03.

[Her10] Herrmann, A., Gruber, O., Seidel, U., et al. Plasma induced arcs in remote areas of ASDEX Upgrade. In *37th EPS Conference on Plasma Physics*. European Physical Society, 2010.

[Hoe21] Hoelzl, M., Huijsmans, G., Pamela, S., et al. The JOREK non-linear extended MHD code and applications to large-scale instabilities and their control in magnetically confined fusion plasmas. *Nuclear Fusion*, 61(6):065001, 2021. 10.1088/1741-4326/abf99f.

[Hoe23] Hoelzl, M. and et al. Non-linear MHD modelling of transients in Tokamaks: Recent advances with the JOREK code. In *IAEA FEC*. London, UK, 2023.

[Hol08] Hollmann, E., Jernigan, T., Parks, P., et al. Measurements of injected impurity assimilation during massive gas injection experiments in DIII-D. *Nuclear Fusion*, 48(11):115007, 2008. 10.1088/0029-5515/48/11/115007.

[Höl12] Hölzl, M., Merkel, P., Huysmans, G. T. A., et al. Coupling JOREK and STARWALL Codes for Non-linear Resistive-wall Simulations. *Journal of Physics: Conference Series*, 401:012010, 2012. 10.1088/1742-6596/401/1/012010.

[Hol15] Hollmann, E. M., Commaux, N., Eidietis, N. W., et al. Mitigation of upward and downward vertical displacement event heat loads with upper or lower massive gas injection in DIII-D. *Physics of Plasmas*, 22(10):102506, 2015. 10.1063/1.4932999.

[Hol21] Holod, I., Hoelzl, M., Verma, P. S., et al. Enhanced preconditioner for jorek mhd solver. *Plasma Physics and Controlled Fusion*, 63(11):114002, 2021. 10.1088/1361-6587/ac206b.

[Hu18] Hu, D., Nardon, E., Lehnen, M., et al. 3D non-linear MHD simulation of the MHD response and density increase as a result of shattered pellet injection. *Nuclear Fusion*, 58(12):126025, 2018. 10.1088/1741-4326/aae614.

[Hum99] Humphreys, D. A. and Kellman, A. G. Analytic modeling of axisymmetric disruption halo currents. *Physics of Plasmas*, 6(7):2742–2756, 1999. 10.1063/1.873231.

[Huy05] Huysmans, G. External kink (peeling) modes in x-point geometry. *Plasma physics and controlled fusion*, 47(12):2107, 2005. 10.1088/0741-3335/47/12/003.

[Hö10] Hölzl, M. *Diffusive Heat Transport across Magnetic Islands and Stochastic Layers in Tokamaks*. Ph.D. thesis, Technische Universität München, 2010.

[Igo15] Igochine, V. (editor). *Active Control of Magneto-Hydrodynamic Instabilities in Hot Plasmas*. Springer Series on Atomic, Optical, and Plasma Physics. Springer-Verlag, Berlin Heidelberg, 2015. ISBN 978-3-662-44221-0. 10.1007/978-3-662-44222-7.

[Ise22] Isernia, N. *The electromagnetic interatction of Magneto-Hydro-Dynamic plasmas with conducting structures*. Ph.D. thesis, Università Degli Studi Di Napoli Federico II, 2022.

[Ise23a] Isernia, N. ASDEX Upgrade conductive structures. Private Communication, 2023.

[Ise23b] Isernia, N., Schwarz, N., Artola, F. J., et al. Self-consistent coupling of JOREK and CARIDDI: On the electromagnetic interaction of 3d tokamak plasmas with 3d volumetric conductors. *Physics of Plasmas*, 30(11), 2023. 10.1063/5.0167271.

[ITE99] ITER Physics Expert Group on Disruptions, Plasma Control and MHD and Editors. Chapter 3: MHD stability, operational limits and disruptions. *Nuclear Fusion*, 39(12):2251–2389, 1999. 10.1088/0029-5515/39/12/303.

[Jac16] Jachmich, S., Drewelow, P., Gerasimov, S., et al. Disruption mitigation at JET using massive gas injection. In *43rd EPS Conference on Plasma Physics*. European Physical Society, 2016.

[Jac21] Jachmich, S., Kruezi, U., Lehnen, M., et al. Shattered pellet injection experiments at JET in support of the ITER disruption mitigation system design. *Nuclear Fusion*, 62(2):026012, 2021. 10.1088/1741-4326/ac3c86.

[Jar86] Jardin, S., Pomphrey, N., and Delucia, J. Dynamic modeling of transport and positional control of tokamaks. *Journal of Computational Physics*, 66(2):481–507, 1986. https://doi.org/10.1016/0021-9991(86)90077-X.

[Jar08] Jardin, S. C., Ferraro, N., Luo, X., et al. The M3D-C1 Approach to Simulating 3D 2-fluid Magnetohydrodynamics in Magnetic Fusion Experiments. Technical report, 2008. 10.2172/959333.

[Kal21] Kallenbach, A. 30 Jahre ASDEX Upgrade. *Physik in unserer Zeit*, 52(3):116–122, 2021. https://doi.org/10.1002/piuz.202101604.

[Kik12] Kikuchi, M., Lackner, K., Tran, M., and Agency, I. A. E. *Fusion Physics*. Publication. International Atomic Energy Agency, 2012. ISBN 978-92-0-130410-0.

[Kir16] Kiramov, D., Lehnen, M., Khayrutdinov, R., and Lukash, V. ITER disruption simulations with improved power balance in the halo region. In *Proc. 43rd EPS Conf. Plasma Physics (Leuven, Belgium, July 2016)*, page P4. 2016. URL `http://ocs.ciemat.es/EPS2016PAP/pdf/P4.071.pdf`.

[Kir17] Kiramov, D. I. and Breizman, B. N. Model of Vertical Plasma Motion during the Current Quench. *Physics of Plasmas*, 24(10):100702, 2017. 10.1063/1.4993071.

[Kre20] Krebs, I., Artola, F. J., Sovinec, C. R., et al. Axisymmetric simulations of vertical displacement events in tokamaks: A benchmark of M3D-C1, NIMROD, and JOREK. *Physics of Plasmas*, 27(2):022505, 2020. 10.1063/1.5127664.

[Leh13] Lehnen, M., Arnoux, G., Brezinsek, S., et al. Impact and mitigation of disruptions with the ITER-like wall in JET. *Nuclear Fusion*, 53(9):093007, 2013. 10.1088/0029-5515/53/9/093007.

[Leh15] Lehnen, M., Aleynikova, K., Aleynikov, P. B., et al. Disruptions in ITER and strategies for their control and mitigation. *Journal of Nuclear Materials*, 463:39–48, 2015. 10.1016/j.jnucmat.2014.10.075.

[Li21] Li, Y., Chen, Z., Yan, W., et al. Comparison of disruption mitigation from shattered pellet injection with massive gas injection on J-TEXT. *Nuclear Fusion*, 61(12):126025, 2021. 10.1088/1741-4326/ac2cf7.

[Li23] Li, J., Zhang, Y., and Tang, X.-Z. Staged cooling of a fusion-grade plasma in a tokamak thermal quench. *Nuclear Fusion*, 63(6):066030, 2023. 10.1088/1741-4326/acce4c.

[Loa04] Loarte, A., Andrew, P., Matthews, G. F., et al. Expected energy fluxes onto TER Plasma Facing Components during disruption thermal quenches from multi-machine data comparisons. In *20. IAEA fusion energy conference*. 2004. URL `https://www.osti.gov/etdeweb/servlets/purl/20641491`.

[Luk96] Lukash, V. E. and Khairutdinov, R. R. Numerical simulation of halo currents in tokamaks. *Plasma Physics Reports*, 22(2):91–96, 1996.

[Mat90] Matthews, G. F., Fielding, S. J., McCracken, G. M., et al. Investigation of the fluxes to a surface at grazing angles of incidence in the tokamak boundary. *Plasma Physics and Controlled Fusion*, 32(14):1301–1320, 1990. 10.1088/0741-3335/32/14/004.

[Mat22] Matveeva, E., Havlicek, J., Artola, F. J., et al. Current quench and vessel currents characterisation at the COMPASS tokamak. *Plasma Physics and Controlled Fusion*, 64(12):125010, 2022. 10.1088/1361-6587/ac9928.

[McC99] McCarthy, P. J., Martin, P., and Schneider, W. The CLISTE Interpretive Equilibrium Code. Technical Report IPP 5/85, Max-Planck-Institut für Plasmaphysik., Garching, 1999.

[Men11] Menard, J., Bromberg, L., Brown, T., et al. Prospects for pilot plants based on the tokamak, spherical tokamak and stellarator. *Nuclear Fusion*, 51(10):103014, 2011. 10.1088/0029-5515/51/10/103014.

[Mer15] Merkel, P. and Strumberger, E. Linear MHD stability studies with the STARWALL code. *arXiv:1508.04911 [physics]*, 2015.

[Miy11] Miyamoto, S. A linear response model of the vertical electromagnetic force on a vessel applicable to ITER and future tokamaks. *Plasma Physics and Controlled Fusion*, 53(8):082001, 2011. 10.1088/0741-3335/53/8/082001.

[Mye17] Myers, C., Eidietis, N., Gerasimov, S., et al. A multi-machine scaling of halo current rotation. *Nuclear Fusion*, 58(1):016050, 2017. 10.1088/1741-4326/aa958b.

[Nak96] Nakamura, Y., Yoshino, R., Pomphrey, N., and Jardin, S. C. Acceleration mechanism of vertical displacement event and its amelioration in tokamak disruptions. *Journal of Nuclear Science and Technology*, 33(8):609–619, 1996. 10.1080/18811248.1996.9731967.

[Nak02] Nakamura, Y., Pautasso, G., Gruber, O., and Jardin, S. C. Axisymmetric disruption dynamics including current profile changes in the ASDEX-Upgrade tokamak. *Plasma Physics and Controlled Fusion*, 44(8):1471–1481, 2002. 10.1088/0741-3335/44/8/304.

[Nar23] Nardon, E., Särkimäki, K., Artola, F., et al. On the origin of the plasma current spike during a tokamak disruption and its relation with magnetic stochasticity. *Nuclear Fusion*, 63(5):056011, 2023. 10.1088/1741-4326/acc417.

[Ned08] Nedospasov, A. Thermal quench in tokamaks. *Nuclear Fusion*, 48(3):032002, 2008. 10.1088/0029-5515/48/3/032002.

[Nol97] Noll, P., Andrew, P., Buzio, M., et al. Present understanding of electromagnetic behaviour during disruptions in jet. In C. VARANDAS and F. SERRA (editors), *Fusion Technology 1996*, pages 751–754. Elsevier, Oxford, 1997. ISBN 978-0-444-82762-3. https://doi.org/10.1016/B978-0-444-82762-3.50157-9. URL `https://www.sciencedirect.com/science/article/pii/B9780444827623501579`.

[Org18] Organization, I. Ter research plan within the staged approach (level iii – provisional version). Technical report, ITER Organization, 2018.

[Pam20] Pamela, S. J. P., Bhole, A., Huijsmans, G. T. A., et al. Extended full-MHD simulation of non-linear instabilities in tokamak plasmas. *Physics of Plasmas*, accepted, 2020. https://doi.org/10.1063/5.0018208.

[Pam22] Pamela, S., Huijsmans, G., and Hoelzl, M. A generalised formulation of g-continuous bezier elements applied to non-linear mhd simulations. *Journal of Computational Physics*, 464:111101, 2022. https://doi.org/10.1016/j.jcp.2022.111101.

[Pap22] Papp, G. Private communication, 2022.

[Par99] Park, W., Belova, E. V., Fu, G. Y., et al. Plasma simulation studies using multilevel physics models. *Physics of Plasmas*, 6(5):1796–1803, 1999. 10.1063/1.873437.

[Par21] Park, S., Lee, K., Lee, H., et al. Experimental results of multiple shattered pellet injection systems in KSTAR. *Fusion Engineering and Design*, 164:112200, 2021. https://doi.org/10.1016/j.fusengdes.2020.112200.

[Pau03] Pautasso, G., Herrmann, A., Eich, T., et al. Analysis of the power deposition in the ASDEX Upgrade divertor during disruptions. In *30th European Physical Society Conference on Plasma Physics and Controlled Fusion*. European Physical Society, 2003. URL `https://pure.mpg.de/rest/items/item_2137580_3/component/file_3310931/content`.

[Pau04] Pautasso, G., Eich, T., Herrmann, A., et al. Details of power deposition in the thermal quench of asdex upgrade disruptions. In *31st European Physical Society Conference on Plasma Physics*. European Physical Society, 2004. URL `https://pure.mpg.de/rest/items/item_2137027/component/file_2137026/content`.

[Pau07] Pautasso, G., Fuchs, C. J., Gruber, O., et al. Plasma shut-down with fast impurity puff on ASDEX Upgrade. *Nuclear Fusion*, 47(8):900–913, 2007. 10.1088/0029-5515/47/8/023.

[Pau11] Pautasso, G., Giannone, L., Gruber, O., et al. The halo current in ASDEX Upgrade. *Nuclear Fusion*, 51(4):043010, 2011. 10.1088/0029-5515/51/4/043010.

[Pau17] Pautasso, G., Bernert, M., Dibon, M., et al. Disruption mitigation by injection of small quantities of noble gas in ASDEX Upgrade. *Plasma Physics and Controlled Fusion*, 59(1):014046, 2017. 10.1088/0741-3335/59/1/014046.

[Peh22] Peherstorfer, T. Fragmentation analysis of cryogenic pellets for disruption mitigation, 2022. URL `https://repositum.tuwien.at/handle/20.500.12708/80329`.

[Pfe18] Pfefferlé, D., Ferraro, N., Jardin, S. C., Krebs, I., and Bhattacharjee, A. Modelling of NSTX hot vertical displacement events using M3D-C1. *Physics of Plasmas*, 25(5):056106, 2018. 10.1063/1.5016348.

[Pin94] Pinkau, K. Annual report 1994. Technical report, Max-Planck-Institut für Plasmaphysik, 1994. URL `https://hdl.handle.net/11858/00-001M-0000-002C-1C32-8`.

[Por08] Portone, A., Villone, F., Liu, Y., Albanese, R., and Rubinacci, G. Linearly perturbed MHD equilibria and 3D eddy current coupling via the control surface method. *Plasma Physics and Controlled Fusion*, 50(8):085004, 2008. 10.1088/0741-3335/50/8/085004.

[Pus15] Pustovitov, V. General approach to the problem of disruption forces in tokamaks. *Nuclear Fusion*, 55(11):113032, 2015. 10.1088/0029-5515/55/11/113032.

[Pus17] Pustovitov, V., Rubinacci, G., and Villone, F. On the computation of the disruption forces in tokamaks. *Nuclear Fusion*, 57(12):126038, 2017. 10.1088/1741-4326/aa8876.

[Pus22] Pustovitov, V. D. Models for calculation of the sideways force due to the kink modes in tokamaks. *Physics of Plasmas*, 29(6):062509, 2022. 10.1063/5.0085171.

[Reu21] Reux, C., Paz-Soldan, C., Aleynikov, P., et al. Demonstration of Safe Termination of Megaampere Relativistic Electron Beams in Tokamaks. *Phys. Rev. Lett.*, 126:175001, 2021. 10.1103/PhysRevLett.126.175001.

[Ric00a] Riccardo, V., Noll, P., and Walker, S. P. Forces between plasma, vessel and TF coils during AVDEs at JET. *Nuclear Fusion*, 40(10):1805–1810, 2000. 10.1088/0029-5515/40/10/311.

[Ric00b] Riccardo, V., Walker, S., and Noll, P. Modelling magnetic forces during asymmetric vertical displacement events in JET. *Fusion Engineering and Design*, 47(4):389–402, 2000. https://doi.org/10.1016/S0920-3796(99)00098-8.

[Ric04] Riccardo, V., Hender, T. C., Lomas, P. J., et al. Analysis of JET halo currents. *Plasma Physics and Controlled Fusion*, 46(6):925, 2004. 10.1088/0741-3335/46/6/001.

[Ric05] Riccardo, V., Loarte, A., and the JET EFDA Contributors. Timescale and magnitude of plasma thermal energy loss before and during disruptions in JET. *Nuclear Fusion*, 45(11):1427, 2005. 10.1088/0029-5515/45/11/025.

[Ric09] Riccardo, V., Arnoux, G., Beaumont, P., et al. Progress in understanding halo current at JET. *Nuclear Fusion*, 49(5):055012, 2009. 10.1088/0029-5515/49/5/055012.

[Roc16] Roccella, R., Roccella, M., Riccardo, V., and and, S. C. Asymmetric toroidal eddy currents (ATEC) to explain sideways forces at JET. *Nuclear Fusion*, 56(10):106010, 2016. 10.1088/0029-5515/56/10/106010.

[Ros97] Rosenbluth, M. and Putvinski, S. Theory for avalanche of runaway electrons in tokamaks. *Nuclear Fusion*, 37(10):1355, 1997. 10.1088/0029-5515/37/10/I03.

[Sap22] Saperstein, A., Levesque, J., Mauel, M., and Navratil, G. Halo current rotation scaling in post-disruption plasmas. *Nuclear Fusion*, 62(2):026044, 2022. 10.1088/1741-4326/ac4186.

[Sap23] Saperstein, A. R., Tinguely, R. A., Granetz, R. S., et al. Disruption halo current rotation scaling on Alcator C-Mod and HBT-EP. *Physics of Plasmas*, 30(4):042506, 04 2023. ISSN 1070-664X. 10.1063/5.0140867.

[Sch95] Schuller, F. C. Disruptions in tokamaks. *Plasma Physics and Controlled Fusion*, 37(11A):A135–A162, 1995. 10.1088/0741-3335/37/11A/009.

[Sch09] Schnack, D. D. *Lectures in Magnetohydrodynamics: With an Appendix on Extended MHD*. Lecture notes in physics. Springer, Berlin, Heidelberg, 2009. 10.1007/978-3-642-00688-3. URL `https://cds.cern.ch/record/1339298`.

[Sch20] Schwarz, N. *Vertical Displacement Events in ASDEX Upgrade*. Master thesis, Universität Heidelberg, Max Planck Institut für Plasmaphysik, Heidelberg, 2020.

[Sch23a] Schwarz, N., Artola, F. J., Hoelzl, M., et al. Experiments and non-linear MHD simulations of hot vertical displacement events in ASDEX-Upgrade. *Plasma Physics and Controlled Fusion*, 65(5):054003, 2023. 10.1088/1361-6587/acc358.

[Sch23b] Schwarz, N., Artola, F. J., Vannini, F., et al. The mechanism of the global vertical force reduction in disruptions mitigated by massive material injection. *Nuclear Fusion*, 2023.

[Seh16] Sehmer, T., Lackner, K., Strumberger, E., et al. Growth of axisymmetric instabilities in ASDEX Upgrade. *Fusion Science and Technology*, 70(1):73–82, 2016. 10.13182/FST15-175.

[Sha72] Shafranov, V. and Zakharov, L. Use of the virtual-casing principle in calculating the containing magnetic field in toroidal plasma systems. *Nuclear Fusion*, 12(5):599, 1972. 10.1088/0029-5515/12/5/009.

[Sha01] Shafranov, V. D., Bondarenko, B., Goncharov, G. A., et al. On the history of the research into controlled thermonuclear fusion. *Physics-Uspekhi*, 44(8):835–843, 2001.

[She20] Sheikh, U., David, P., Ficker, O., et al. Disruption mitigation efficiency and scaling with thermal energy fraction on ASDEX Upgrade. *Nuclear Fusion*, 60(12):126029, 2020. 10.1088/1741-4326/abb425.

[Smi13] Smith, H., Boozer, A., and Helander, P. Passive runaway electron suppression in tokamak disruptions. *Physics of Plasmas*, 20(7), 2013.

[Spi53] Spitzer, L. and Härm, R. Transport phenomena in a completely ionized gas. *Phys. Rev.*, 89:977–981, Mar 1953. 10.1103/PhysRev.89.977.

[Spi23] Spinicci, L. *3D Nonlinear MHD modelling studies: Plasma Flow and Realistic Magnetic Boundary Impacton Magnetic self-organisation in Fusion Plasmas*. Ph.D. thesis, Università degli Studi di Padova Centro Ricerche Fusione (CRF), 2023.

[Sta00] Stangeby, P. The Plasma Boundary of Magnetic Fusion Devices. The Plasma Boundary of Magnetic Fusion Devices. Series: Series in Plasma Physics, 2000. 10.1201/9781420033328.

[Str91] Strait, E., Lao, L., Luxon, J., and Reis, E. Observation of poloidal current flow to the vacuum vessel wall during vertical instabilities in the DIII-D tokamak. *Nuclear Fusion*, 31(3):527, 1991. 10.1088/0029-5515/31/3/011.

[Str14] Strauss, H., Sugiyama, L., Paccagnella, R., Breslau, J., and Jardin, S. Tokamak toroidal rotation caused by AVDEs and ELMs. *Nuclear Fusion*, 54(4):043017, 2014. 10.1088/0029-5515/54/4/043017.

[Str16] Strumberger, E. and Günter, S. CASTOR3D: Linear stability studies for 2D and 3D tokamak equilibria. *Nuclear Fusion*, 57(1):016032, 2016. 10.1088/0029-5515/57/1/016032.

[Str17] Strauss, H., Joffrin, E., Riccardo, V., Breslau, J., and and, R. P. Comparison of JET AVDE disruption data with M3D simulations and implications for ITER. *Physics of Plasmas*, 24(10), 2017. 10.1063/1.5004692.

[Tes22] Teschke, M. Bandwidth of shunts. Technical report, Max Planck Insitute for Plasma Physics, Garching, 2022.

[Tin18] Tinguely, R., Granetz, R., Berg, A., et al. High-resolution disruption halo current measurements using Langmuir probes in Alcator C-Mod. *Nuclear Fusion*, 2018. 10.1088/1741-4326/aa8fa6.

[Vil13] Villone, F., Barbato, L., Mastrostefano, S., and Ventre, S. Coupling of nonlinear axisymmetric plasma evolution with three-dimensional volumetric conductors. *Plasma Physics and Controlled Fusion*, 55(9):095008, 2013. 10.1088/0741-3335/55/9/095008.

[Vri11] de Vries, P., Johnson, M., Alper, B., et al. Survey of disruption causes at JET. *Nuclear Fusion*, 51(5):053018, 2011. 10.1088/0029-5515/51/5/053018.

[Wad79] Waddell, B. V., Carreras, B., Hicks, H. R., and Holmes, J. A. Nonlinear interaction of tearing modes in highly resistive tokamaks. *The Physics of Fluids*, 22(5):896–910, 1979. 10.1063/1.862685.

[Wag84] Wagner, F., Fussmann, G., Grave, T., et al. Development of an Edge Transport Barrier at the H-Mode Transition of ASDEX. *Phys. Rev. Lett.*, 53:1453–1456, 1984. 10.1103/PhysRevLett.53.1453.

[Wag07] Wagner, F. A quarter-century of h-mode studies. *Plasma Physics and Controlled Fusion*, 49(12B):B1, 2007. 10.1088/0741-3335/49/12B/S01.

[Wes78] Wesson, J. Hydromagnetic stability of tokamaks. *Nuclear Fusion*, 18(1):87–132, 1978. 10.1088/0029-5515/18/1/010.

[Wes89] Wesson, J., Gill, R., Hugon, M., et al. Disruptions in JET. *Nuclear Fusion*, 29(4):641, 1989. 10.1088/0029-5515/29/4/009.

[Wes11] Wesson, J. and Campbell, D. *Tokamaks.* International Series of Monogr. OUP Oxford, 2011. ISBN 978-0-19-959223-4.

[Why07] Whyte, D., Granetz, R., Bakhtiari, M., et al. Disruption mitigation on Alcator C-Mod using high-pressure gas injection: Experiments and modeling toward ITER. *Journal of Nuclear Materials*, 363-365:1160–1167, 2007. https://doi.org/10.1016/j.jnucmat.2007.01.149.

[Xia23] Xia, W., Zeng, L., Tang, T., et al. The timescale of thermal quench during disruptions in EAST. *Plasma Physics and Controlled Fusion*, 65(8):085011, 2023. 10.1088/1361-6587/acdf1c.

[Xu20] Xu, H. B., Zhu, G. L., Cao, Z., et al. Preliminary experimental results of shattered pellet injection on the HL-2A tokamak. *Fusion Science and Technology*, 76(7):857–860, 2020. 10.1080/15361055.2020.1817703.

[Yan22] Yanovskiy, V., Isernia, N., Pustovitov, V., and Villone, F. Sideways forces on asymmetric tokamak walls during plasma disruptions. *Nuclear Fusion*, 62(8):086001, 2022. 10.1088/1741-4326/ac5fea.

[Yu12] Yu, Y., Kim, Y.-O., Kim, H.-K., et al. First results on disruption mitigation by massive gas injection in Korea Superconducting Tokamak Advanced Research. *Review of Scientific Instruments*, 83(12):123509, 2012. 10.1063/1.4772573.

[Zam14] Zammuto, I. Resistività equivalente bellow. Technical report, IPP Garching, 2014.

[Zha23] Zhang, Y., Li, J., and Tang, X.-Z. Cooling flow regime of a plasma thermal quench. *Europhysics Letters*, 141(5):54002, 2023. 10.1209/0295-5075/acbb20.

[Zoh15] Zohm, H. *Magnetohydrodynamic stability of tokamaks*. John Wiley & Sons, 2015.

[Zyl22] Zylstra, A., Hurricane, O., Callahan, D., et al. Burning plasma achieved in inertial fusion. *Nature*, 601(7894):542–548, 2022. 10.1038/s41586-021-04281-w.